

Advances in Electrochemical Simulation and its Application to Electroanalysis

A thesis submitted for the degree of
Doctor of Philosophy
in Physical & Theoretical Chemistry

Edward O. Barnes
St John's College

Trinity Term 2014

Abstract

This thesis is concerned with the simulation of various electrochemical experiments and its application to electroanalysis.

Chapter 1 outlines the fundamental principles of electrochemistry which are of importance for the reading of this thesis. Chapter 2 then outlines the methods used in the numerical simulation of electrochemical experiments.

Chapters 3 and 4 are concerned with the electrochemistry of nanoparticles, and how this is affected by the presence of near wall hindered diffusion. In Chapter 3, a computational model to simulate anodic particle coulometry of nanoparticles in the presence of hindered diffusion is developed, and the effect of this hindered diffusion investigated. The model is then applied to simulate experimental data. Chapter 4 looks at the effect of hindered diffusion on the adsorption of nanoparticles on electrode surfaces, and investigates the effects of this adsorption on electrochemical experiments with nanoparticles generally.

Chapters 5, 6 and 7 are concerned with band electrodes in isolation, in a pair and in an array respectively. In Chapter 5, a model to simulate double potential step chronoamperometry at an individual band electrode is developed, and used to successfully simulate experimental data. Chapter 6 looks at dual band electrodes used in generator-collector mode, and how this can be used to simultaneously measure the concentration of two species in solution. Chapter 7 looks at interdigitated arrays of band and ring electrodes in generator-collector mode, and develops a model to simulate cyclic voltammetry in both cases, as well as investigating under what conditions interdigitated ring arrays may be modelled as interdigitated band arrays.

Chapter 8 develops a model to simulate chronoamperometry and cyclic voltammetry

at porous electrodes, and investigates the consequences for electroanalysis of having a porous layer.

Finally, Chapter 9 investigates the Marcus-Hush theory of electron transfer kinetics, and looks at the effect of the kinetically limited currents resulting from this theory to the equivalence relation between microdisc electrodes and sphere-on-a-surface electrodes.

Acknowledgements

Firstly, immeasurable thanks must go to Professor Richard Compton for his advice, encouragement and patience throughout the three years of my DPhil, my Part II year and two summer projects. Thank you also for being a wonderful tutor throughout my undergraduate degree.

For carrying out the experiments presented in this thesis, thanks must go to Dr. Yige Zhou and Ms. Linhongjia Xiong of the Compton Group, and Dr. Anna Fernández-la-Villa, Dr. Diego F. Pozo-Ayuso and Dr. Mario Castaño-Álvarez of Micrux Technologies®. Many thanks also to Prof. Frank Marken, Dr. Sara Dale and Ms. Grace Lewis from Bath University and Prof. Angela Molina and Dr. Joaquín Sánchez of the University of Murcia for their collaboration and input.

Thank you also to the rest of the Compton Group, past and present, for your friendship and for making my time in the group so enjoyable. From P.T. revelry in my first summer project to Friday night Plush at the end of my DPhil, not to mention weekly group drinks, it's been a blast from start to finish.

Everyone I've met at St John's and in Oxford generally over the past seven years, you've been great. I've made what I'm sure will be lifelong friends here, and some of my best memories are of times spent with you all.

This is also true of the old crowd in Backwell, some of whom I've known since I was five. You've given me memories that will last a lifetime, from surviving the insanity of certain teachers to hanging out at The Barn.

St John's College, Oxford must also be thanked for first of all offering me a place to study, and then for seven years of room and board, lots of excellent dinners, two

scholarships and several very generous grants. Special thanks also to my undergraduate tutors, Professor Richard Compton, Professor Fraser Armstrong, Dr. Angela Russell, Professor George Fleet and Dr. Devinder Sivia for ensuring I made it through my MChem. Thank you also to all the bar staff!

Many thanks to EPSRC for funding my DPhil research and my upcoming post-doctoral research.

Finally, most thanks of all to my Mum, for absolutely everything.

Glossary

Where appropriate, symbols are defined in terms of the generic species i or the reduction $\mathrm{A} + \mathrm{e}^- \rightleftharpoons \mathrm{B}$.

Roman Symbols

Symbol	Definition	Units
A	Electrode area	m^2
c_i	Concentration of species i	$\mathrm{mol\ m}^{-3}$
c_i^*	Bulk solution concentration of species i	$\mathrm{mol\ m}^{-3}$
c_i^0	Concentration of species i at the electrode surface	$\mathrm{mol\ m}^{-3}$
D_i	Diffusion coefficient of species i	$\mathrm{m}^2\ \mathrm{s}^{-1}$
E	Potential applied to the working electrode	V
$E_\mathrm{f}^\ominus$	Formal potential	V
F	Faraday constant ≈ 96485	$\mathrm{C\ mol}^{-1}$
G	Gibbs Energy	$\mathrm{J\ mol}^{-1}$
h	Distance between nanoparticle edge and wall	m
I	Current	A
I_p	Peak Current	A
j	Flux	$\mathrm{mol\ m}^{-2}\ \mathrm{s}^{-1}$
k	Nanoparticle adsorption rate constant	$\mathrm{m\ s}^{-1}$
k^0	Standard electrochemical rate constant	$\mathrm{m\ s}^{-1}$
k_B	Boltzmann constant $\approx 1.381 \times 10^{-23}$	$\mathrm{J\ K}^{-1}$

Continued on next page

$k_{\mathrm{red/ox}}$	Rate constant for reduction/oxidation	m s^{-1}
l	Electrode length	m
m	Number of pairs of electrodes in an inerdigitated array	Unitless
N	Collection efficiency	Unitless
N_{A}	Avogadro constant $\approx 6.022 \times 10^{23}$	mol^{-1}
N_{s}	Number of hollow spheres in a porous electrode	Unitless
R	Gas constant ≈ 8.314	J K^{-1} mol^{-1}
r	Radial coordinate in spherical/cylindrical space	m
r	Radius of disc in a porous electrode	m
r_{e}	Electrode radius	m
r_{NP}	Nanoparticle radius	m
r_{s}	Radius of hollow sphere in a porous electrode	m
T	Temperature	K
t	Time	s
w_{e}	Electrode width	m
w_g	Inter-electrode gap width	m
x	x coordinate in Cartesian space	m
y	y coordinate in Cartesian space	m
z	Vertical coordinate in cylindrical space	m

Greek Symbols

Symbol	Definition	Units
α	Butler-Volmer transfer coefficient	Unitless
Γ	Surface concentration of adsorbed nanoparticles	mol m^{-2}
Γ_m	Monolayer surface concentration of adsorbed nanoparticles	mol m^{-2}
η	Viscosity	Pa s
λ	Reorganisation energy	eV
ν	Scan rate	V s^{-1}
ψ	Hindrance factor	Unitless

Dimensionless Parameters

Where appropriate, r_e (radius of a disc, sphere or hemisphere electrode) may be replaced with w_e (width of a band or ring electrode).

Symbol	Definition
C_i	$\frac{c_i}{c_A^*}$
D_i'	$\frac{D_i}{D_A}$
d'	$\frac{w_g}{w_e}$
J	$\frac{r_e}{c_A^* D_A} j$
k'	$\frac{r_e}{D_A} k$
K^0	$\frac{r_e}{D_A} k^0$

Continued on next page

R	$\dfrac{r}{r_{\mathrm{e}}}$
R_{d}	$\frac{r_{\mathrm{d}}}{r_{\mathrm{s}}}$
R_{NP}	$\dfrac{r_{\mathrm{NP}}}{r_{\mathrm{e}}}$
X	$\dfrac{x}{w_{\mathrm{e}}}$
Y	$\dfrac{y}{w_{\mathrm{e}}}$
Z	$\dfrac{z}{r_{\mathrm{e}}}$
θ	$\dfrac{F}{RT}E$
Λ	$\dfrac{F}{RT}\lambda$
ξ	$\dfrac{c_{\mathrm{A}}^{*}r_{\mathrm{e}}}{\Gamma_{\mathrm{m}}}$
ρ	$\dfrac{\Gamma}{\Gamma_{\mathrm{m}}}$
σ	$\dfrac{Fr_{\mathrm{e}}^{2}}{RTD_{\mathrm{A}}}\nu$
τ	$\dfrac{D_{\mathrm{A}}}{r_{\mathrm{e}}^{2}}t$

Contents

Abstract i
Acknowledgements iii
Glossary v

1 Fundamentals of Electrochemistry **1**
1.1 Mass transport 1
1.2 Electrochemical equilibria 3
1.3 Electrochemical kinetics 4
1.4 Electrochemical experiments 5
1.4.1 Three electrode systems 6
1.4.2 The need for supporting electrolyte 6
1.5 Potential step chronoamperometry 8
1.6 Cyclic voltammetry 10
1.6.1 Effect of electrochemical kinetics 11
1.6.2 Effect of scan rate 12
1.7 Microelectrodes 13
1.7.1 Pseudo steady state currents 15
1.8 Surface bound and thin layer voltammetry 17
1.8.1 Effect of scan rate 19
1.9 Conclusions 20
References 20

2 Simulation Methods **22**
2.1 Constructing the model 22
2.2 The finite difference method 23
2.3 Explicit and implicit methods 26
2.4 The Newton-Rapshon method 28
2.5 The alternating direction implicit method 30
2.6 Dimensionless parameters 31
2.7 Spatial and temporal grids 31
References 32

3 The Effect of Hindered Diffusion on the Electrochemistry of Nanoparticles 34

3.1 Introduction . . . 34

3.2 Theory . . . 37

3.2.1 Dimensionless parameters . . . 40

3.2.2 Boundary conditions . . . 41

3.2.3 Numerical methods . . . 42

3.3 Simulated results and discussion . . . 44

3.3.1 Measuring the flux . . . 44

3.3.2 Effect of particle size . . . 46

3.4 Experimental . . . 50

3.4.1 Chemicals . . . 50

3.4.2 Instrumental . . . 50

3.5 Experimental results . . . 51

3.6 Conclusions . . . 55

References . . . 55

4 The Rate of Adsorption of Nanoparticles on Microelectrode Surfaces 57

4.1 Introduction . . . 58

4.2 Theory . . . 59

4.3 Simulated results and discussion . . . 61

4.4 Conclusions . . . 70

References . . . 71

5 Double Potential Step Chronoamperometry at a Microband Electrode: Theory and Experiment 73

5.1 Introduction . . . 73

5.2 Theory . . . 77

5.2.1 Boundary Conditions . . . 78

5.2.2 Numerical Methods . . . 81

5.3 Theoretical Results . . . 83

5.4 Experimental . . . 90

5.4.1 Chemicals . . . 90
5.4.2 Instrumental . . . 90
5.5 Experimental Results . . . 91
5.6 Conclusions . . . 93
References . . . 93

6 Dual Band Electrodes in Generator−Collector Mode: Simultaneous Measurement of Two Species 97
6.1 Introduction . . . 98
6.2 Theory . . . 102
6.2.1 Boundary conditions . . . 103
6.2.2 Numerical methods . . . 106
6.3 Theoretical Results . . . 108
6.3.1 Varying relative concentrations of species A and X . . . 108
6.3.2 Effect of Inter-Electrode Distance . . . 110
6.3.3 Effect of the Chosen Collection Efficiency . . . 111
6.3.4 Theoretical Application to Simultaneous Measurement of Ascorbic Acid and Dopamine . . . 113
6.4 Summary of Method . . . 113
6.5 Conclusions . . . 115
References . . . 116

7 Interdigitated Ring Arrays: Theory and Experiment 121
7.1 Introduction . . . 122
7.2 Theory . . . 125
7.2.1 Interdigitated band arrays . . . 126
7.2.2 Interdigitated ring arrays . . . 129
7.2.3 Numerical methods . . . 132
7.3 Theoretical Results . . . 133
7.4 Experimental . . . 137
7.5 Experimental Results . . . 138
7.5.1 Interdigitated band array . . . 138

7.5.2 Interdigitated ring array . . . 139
7.6 Conclusions . . . 141
References . . . 141

8 Voltammetry at porous electrodes 144
8.1 Introduction . . . 144
8.2 Theory . . . 146
8.2.1 Simulation of chronoamperometry within a single sphere . . . 149
8.2.2 Simulation of cyclic voltammetry within a single sphere . . . 151
8.2.3 Simulation of chronoamperometry and cyclic voltammetry at a disc electrode . . . 152
8.2.4 Total current at a porous electrode . . . 153
8.2.5 Numerical Methods . . . 154
8.3 Simulated results and discussion . . . 156
8.3.1 Chronoamperometry . . . 156
8.3.2 Cyclic voltammetry . . . 160
8.3.3 The possibility of two peaks arising from a single $A \pm e^- \rightleftharpoons B$ process 164
8.3.4 Extraction of K^0 . . . 165
8.4 Conclusions . . . 168
References . . . 168

9 Equivalence of Microdisc and Sphere-On-Surface Electrodes In the Marcus-Hush Formalism 171
9.1 Introduction . . . 172
9.2 Theory . . . 178
9.2.1 Boundary conditions . . . 179
9.2.2 Numerical Methods . . . 182
9.3 Theoretical results . . . 183
9.3.1 Kinetically limited currents at a microdisc electrode . . . 184
9.3.2 Comparison of Marcus-Hush theory at microdisc and impacting nanoparticles . . . 186
9.4 Conclusions . . . 189

References 189

10 Conclusions **193**

Chapter 1

Fundamentals of Electrochemistry

This introductory chapter outlines some fundamental concepts of importance for the reading of this thesis. Mass transport, electrochemical thermodynamics and electrochemical kinetics are detailed, and the interplay of these three concepts in electrochemical experiments described.

1.1 Mass transport

The motion of a species though solution (be it a molecule or a larger nanoparticle) is made up of three components: migration, convection and diffusion [1]. Migration is the result electrical interactions between species, meaning that charged species will move down (or up, depending on the charge) electric field gradients. While consideration of migration can allow the extraction of valuable information [2–5], it is often undesirable and is suppressed using an excess of supporting electrolyte (*vide infra*). It can be neglected for the remainder of this thesis.

Convective mass transport comes about from either the flow of solution due to temperature gradients or density differences (natural convection) or mechanical stirring or pumping of the solution (forced convection) [6]. Natural convection may occur if an ex-

periment has a particularly long timescale and the reaction has a large enthalpy change, but for the purposes of this thesis can be neglected. Forced convection can also be neglected for work here presented, but plays an important part in some closely related work and should be kept in mind (see Chapter 6 for details).

Overwhelmingly the most important mode of mass transport for work in this thesis is diffusion. Fick's laws are used to model diffusion, and are staple equations for the electrochemist. Fick's first law gives the flux of a species (defined as the net number of moles passing though a unit area in unit time in a particular direction) [7]:

$$j_{\mathrm{i}} = -D_{\mathrm{i}} \frac{\partial c_{\mathrm{i}}}{\partial x} \tag{1.1}$$

where j_{i} is the flux of species i (mol m^{-2} s^{-1}), c_{i} is the concentration of species i (mol m^{-3}), x is some spatial coordinate (m) and D_{i} is the diffusion coefficient of species i (m^2 s^{-1}), a constant of proportionality which is a function of the nature of the species concerned, the nature of the solvent and the temperature. All symbols are defined in the Glossary. The essence of Fick's first law is that a species will move down a concentration gradient from an area of high concentration to an area of low concentration.

Fick's second law, derived from the first, gives the concentration dependence of a species over time:

$$\frac{\partial c_{\mathrm{i}}}{\partial t} = D_{\mathrm{i}} \nabla^2 c_{\mathrm{i}} \tag{1.2}$$

where ∇^2 is the Laplacian operator. The form of this operator is dependent on the symmetry of the system, and will be given on a case by case basis in later chapters.

1.2 Electrochemical equilibria

Consider an equilibrium between two species A and B, where B is the reduced form of A:

$$\mathrm{A} + \mathrm{e}^- \rightleftharpoons \mathrm{B} \tag{1.3}$$

in a solution containing an electrode. If the electrode is subject to a sufficiently negative potential, E, (relative to the solution) it will become thermodynamically favourable for electrons to pass from the electrode to the solution, and convert species A at the electrode surface to species B. Conversely, a sufficiently positive potential on the electrode will favour the transfer of electrons from species B in solution to the electrode.

This flow of electrons will manifest itself as an electrical current which can be measured (assuming a circuit is completed using a second electrode). At some specific potential, the rate of electron transfer from the electrode to species A will be balanced against the rate of transfer from species B to the electrode, and no current will flow. The value of this potential will be a function of the relative amounts of A and B present in solution. This potential is quantified using the Nernst equation [6]:

$$E = E_{\mathrm{f}}^{\ominus} + \frac{RT}{F} \ln\left(\frac{c_{\mathrm{A}}}{c_{\mathrm{B}}}\right) \tag{1.4}$$

where $E_{\mathrm{f}}^{\ominus}$ is the formal potential of the A/B couple (V), the potential at which no current will flow if A and B are present in equal amounts.

It is, however, impossible to measure this value using only one electrode. As mentioned above, a second electrode is needed to complete an electrical circuit. The value E is measured relative to this second reference electrode, where a known reference electrochemical

reaction is maintained at equilibrium, drawing negligible amounts of current.

1.3 Electrochemical kinetics

Our discussion of the Nernst equation above assumes that the electron transfer reaction occurs as soon as the relevant potential is applied (or that infinite time is allowed for the transfer to take place). In reality, however, the rate at which this transfer takes place will be limited by the electrochemical kinetics of the system. The rate of the transfer, which can be considered as a flux of material through the electrode surface, can be expressed as:

$$j_0 = k_{\mathrm{red}} c_{\mathrm{A}}^0 - k_{\mathrm{ox}} c_{\mathrm{B}}^0 \tag{1.5}$$

where c_{A}^0 and c_{B}^0 are the concentrations of species A and B at the electrode surface (mol m^{-3}), and k_{red} and k_{ox} are rate constants for reduction and oxidation (m s^{-1}). These rate constants are dependent on the potential applied to the electrode. The most commonly used model to quantify these rate constants is Butler-Volmer theory [8, 9], where they are defined in the following way:

$$k_{\mathrm{red}} = k^0 \exp\left[-\alpha \frac{F\left(E - E_{\mathrm{f}}^{\ominus}\right)}{RT}\right] \tag{1.6}$$

$$k_{\mathrm{ox}} = k^0 \exp\left[(1-\alpha) \frac{F\left(E - E_{\mathrm{f}}^{\ominus}\right)}{RT}\right] \tag{1.7}$$

where $(E - E_{\mathrm{f}}^{\ominus})$ is the overpotential, and is the driving force for either reduction or oxidation to take place. A negative overpotential will favour reduction, a positive one will favour oxidation.

The value α is the transfer coefficient, an empirical quantity which can take a value

between zero and unity, although is often found to be ~ 0.5 [1]. A value less than 0.5 indicates an "early" transition state, where the transition state resembles the starting material, species A. If α is greater than 0.5, a "late" transition state, similar in structure to species B, is seen.

k^0 (m s^{-1}) is known as the standard electrochemical rate constant, and dictates whether the overall reaction is fast or slow. A small value of k^0 will require a larger overpotential to drive the reaction (in either direction). The value of k^0 can be predicted using Marcus theory [10–12]. While a fuller account of Marcus theory and the related Marcus-Hush theory of electron transfer (an alternative to Butler-Volmer theory) is given in Chapter 9, the crux of the argument is that if species A and B are structurally dissimilar, then k^0 will be small. If A and B closely resemble each other, then k^0 will be large and fast kinetics will be observed. Other factors, such as electronic structure and spin arguments, can also be important.

The current, I (A), drawn at the electrode is proportional to this flux of material through the surface, and is given by:

$$I = -FAj_0 \tag{1.8}$$

where A is the surface area of the electrode (m^2).

1.4 Electrochemical experiments

The experiments considered throughout this thesis are all amperometric in nature, *i.e.* the electrode potential is controlled and a current is measured (as opposed to a potentiometric

experiment, where the current is fixed, generally at zero, and a potential measured). Before an experiment can be carried out, two important conditions must be satisfied: a three electrode system is needed, as well as a large excess of inert supporting electrolyte.

1.4.1 Three electrode systems

In addition to the electrode where the electron transfer reaction of interest occurs (the working electrode), a second electrode is needed, a reference electrode (as discussed above). It is relative to this electrode that the potential at the working electrode is measured.

An important feature of a reference electrode is that it must maintain a known, and well characterised, electrochemical reaction at equilibrium. To achieve this, no (or at least negligible) current must be drawn at the reference electrode. This is a problem, since we do want to draw (and measure) current at the working electrode. A third electrode is therefore needed (the counter electrode). At this electrode, some electron transfer takes place to complete the electrical circuit and allow current to flow.

In some circumstances, a two electrode setup may be used. If the current drawn at the working electrode is very small (if it has a very small surface area, for example) then the reference electrode may be used as a counter electrode, since the current drawn will be small and will not disturb the equilibrium to any great extent.

1.4.2 The need for supporting electrolyte

During the course of an amperometric electrochemical experiment, electrons are necessarily transferred between the working electrode and solution. This creates a build up of excess charge in the solution in the region of the electrode. As this happens, an electric field is created which extends out into solution. This means the potential drop between

the electrode and solution (ϕ_e - ϕ_s, the driving force for the electron transfer) takes place over a greater distance. The electron transfer takes place *via* quantum mechanical tunnelling over a distance of *c.a.* 10-20 Å, within a zone of electron transfer, (ZET). It is important that the ZET is located at a distance outside the potential drop range. Adding an large excess of inert salt (or supporting electrolyte, creating a fully supported system) compresses the region of potential drop very close to the electrode surface, since the excess charge is dissipated more effectively. If only a small amount of supporting electrolyte is present, the charge generated near the electrode surface is not dissipated effectively and an electric field will extend beyond the ZET. This is shown in Figure 1.1.

This causes two undesirable effects. If the ZET is located inside the electric field, the full potential drop between electrode and solution is not felt, and there is a reduced driving force for the electron transfer. Secondly, an extended electric field will promote the electrical migration of charged species. The majority of electroanalysis techniques

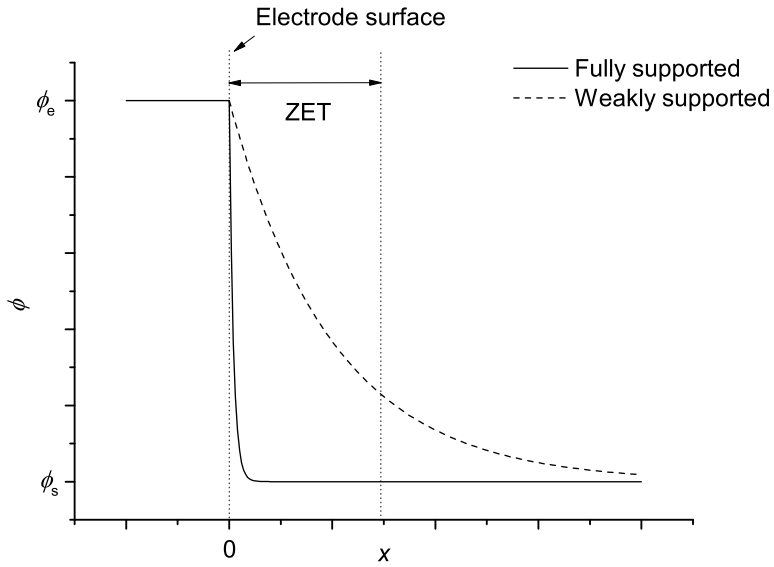


Figure 1.1: Potential profiles in a fully supported system (solid line) and a weakly supported system (dashed line).

require a diffusion only experiment, so migration must be suppressed. The addition of supporting electrolyte removes both of these problems.

1.5 Potential step chronoamperometry

The simpler of the two principal experiments discussed in this thesis is potential step chronoamperometry. This comes in two forms, single step and double step.

In both experiments, only species A is considered to be initially present in solution. In the single step variant, the potential is initially held at a value at which species A is not reduced and no current flows. The potential is then stepped to a large, negative overpotential for a set amount of time, which promotes reduction at a diffusion controlled rate (or it is stepped to a large positive potential to promote oxidation at a diffusion controlled rate). Any species A which comes into contact with the electrode will be immediately reduced (or oxidised, from here a reduction is assumed). Immediately after the step, there will be a very large current as all of species A initially at the surface is reduced. The current then drops off as species A is used up and must diffuse to the surface in order to react. The long time behaviour of the current will depend on the geometry of the electrode. It may eventually drop off to zero, or may reach a steady state current after a certain time (see section 1.7 for more information on when and why steady state currents are observed).

Double potential step chronoamperometry proceeds exactly as for single step, but after the large negative overpotential has been applied for a set amount of time, the potential is stepped again to a large positive overpotential. This re-oxidises the species B that was formed in the first step back to species A. The current profile is similar to the first step,

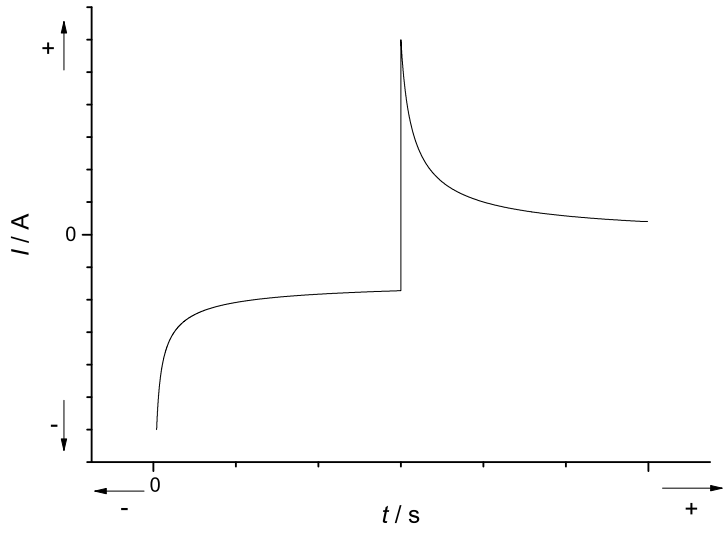


Figure 1.2: A typical double potential step chronoamperogram

but with opposite sign and will always drop off to zero current, since only a finite amount of species B was formed in the first step.

Figure 1.2 shows the result of a typical double potential step chronoamperometry experiment. In the single step variant, only the first half of the response, with negative current (assuming a reduction) is seen.

Chronoamperometry can be used to gain information on the concentration and diffusion coefficient of species A in the first step, and the diffusion coefficient of species B in the second step. An empirical equation, fitted to simulations, describing single step chronoamperometry at a disc electrode has been developed by Shoup and Szabo [13]:

$$|I| = 4nFD_{\mathrm{A}}c^{*}_{\mathrm{A}}r_{\mathrm{e}}f(\tau) \tag{1.9}$$

$$f(\tau) = 0.7854 + 0.4432\tau^{-\frac{1}{2}} + 0.2146\exp\left(-0.3912\tau^{-\frac{1}{2}}\right) \tag{1.10}$$

$$\tau = \frac{D_{\mathrm{A}}}{r_{\mathrm{e}}^{2}}t \tag{1.11}$$

where n is the number of moles of electrons transferred per mole of reactant, and r_e is the radius of the disc electrode (m). Fitting this equation to the first step of a chronoamperogram allows for the extraction of c_A and D_A. Numerical simulation can be used to fit the second step and extract D_B (see Chapter 5 for further details).

1.6 Cyclic voltammetry

In cyclic voltammetry (CV) experiments, the potential is not stepped from one value to another, but is swept linearly from a starting value to a vertex potential, and then back again [1]. This means that the driving force for the electron transfer will change throughout the experiment, unlike in chronoamperometry, where large overpotentials ensure diffusion control throughout.

Figure 1.3 shows a typical cyclic voltammogram for the reduction of some electroactive species in solution, and is illustrative of several key features. In region 1, at the start of

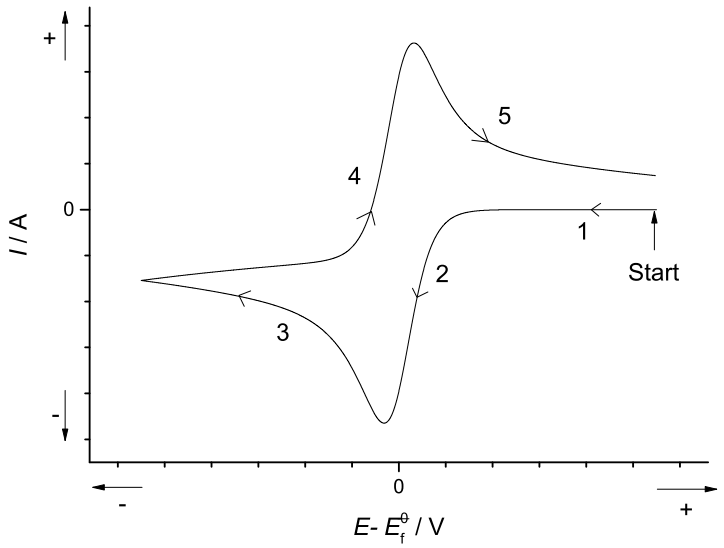


Figure 1.3: A typical cyclic voltammogram

the experiment, the potential is positive of the formal potential, so no reduction takes place and no current is drawn. As the formal potential is approached, reduction begins to be driven and the current grows exponentially in region 2. As species A is reduced, it is depleted around the electrode surface. This depletion means that the current passes through a peak and begins to drop off, as shown in region 3.

On the reverse sweep, similar effects are seen. In region 4, as the potential again approaches the formal potential, the re-oxidation of the species B that has been produced begins to be driven and the current again increases, although it is now positive. Again a peak is seen as species B is depleted, and in region 5 the rate at which species B arrives at the electrode becomes the limiting factor.

1.6.1 Effect of electrochemical kinetics

Two important features of a voltammogram are the separation between the two peaks, and the height of the peaks, the former of which is controlled by the electrochemical kinetics.

This is exemplified in Figure 1.4. In this figure, the solid line represents a system with fast, or reversible, electrochemical kinetics with $k^0 = 10^{-4}$ m s^{-1}. Any value of k^0 larger than this, all else being equal, will produce essentially the same voltammogram. The dashed line represents intermediate, or quasi-reversible, electrochemical kinetics. The peaks have become further apart and the forward peak height is a little lowered. The dotted line, representing fully irreversible electrochemical kinetics, has widely separated peaks. which will become further apart as k^0 is lowered. The forward peak height has reached the fully irreversible limit. The smaller the value of k^0, the larger the overpotential must be to drive the electron transfer, which is easily rationalised by inspection of

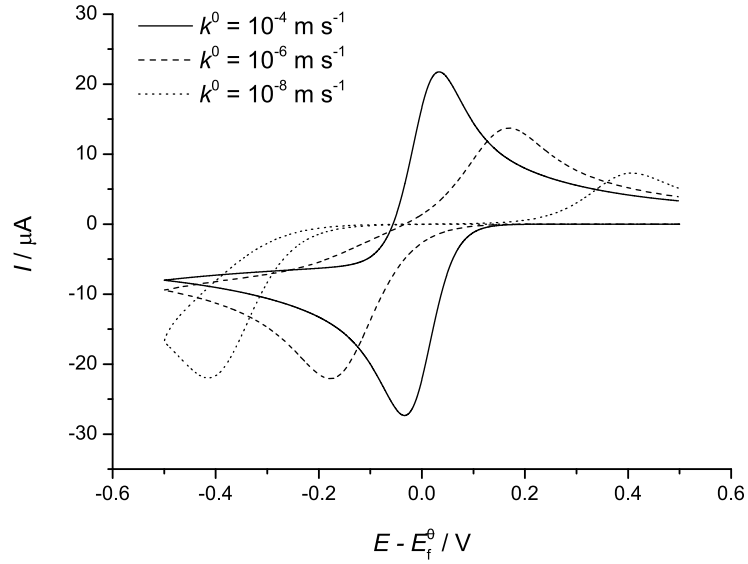


Figure 1.4: Cyclic voltammograms exhibiting different electrochemical kinetics. Solid line: $k^0 = 10^{-4}$ m s^{-1}, dashed line: $k^0 = 10^{-6}$ m s^{-1} and dotted line: $k^0 = 10^{-8}$ m s^{-1}. Other parameters are: $c_\mathrm{A} = 10$ mM, $D_\mathrm{A} = D_\mathrm{B} = 1 \times 10^{-9}$ m^2 s^{-1}, $r_\mathrm{e} = 1$ mm, $\alpha = 0.5$, $\nu = 0.01$ V s^{-1}.

Equations 1.7 and 1.6.

1.6.2 Effect of scan rate

The rate at which the potential applied to the working electrode is swept (the scan rate) can be controlled, and has an effect on the voltammetry. The height of the forward peak (I_p) is (for macroelectrodes, see later for microelectrodes) a function of the square root of the scan rate. The Randles-Ševčík equation quantifies this [1], and is given for a fully reversible system by:

$$|I_\mathrm{p}| = 0.446nFAc_\mathrm{A}^*\sqrt{\frac{FD_\mathrm{A}\nu}{RT}} \tag{1.12}$$

where ν is the scan rate in V s^{-1}. Other symbols have their usual meanings.

The cause of this increase is peak current with scan rate relates to the extent of the

depletion layer which forms around the electrode. The extent of the depletion layer is proportional to the square root of the time it has had to form. Einstein's theory of diffusion states that, in one dimension, the root mean squared displacement of a species undergoing random motion over a given time will be [14]:

$$\sqrt{\langle x^2 \rangle} = \sqrt{2Dt} \tag{1.13}$$

Therefore, the extent of the depletion layer (x_d) above the electrode (after a specific number of Volts have been swept out) will be proportional to the square root of the inverse scan rate:

$$x_\mathrm{d} \propto \sqrt{\frac{1}{\nu}}. \tag{1.14}$$

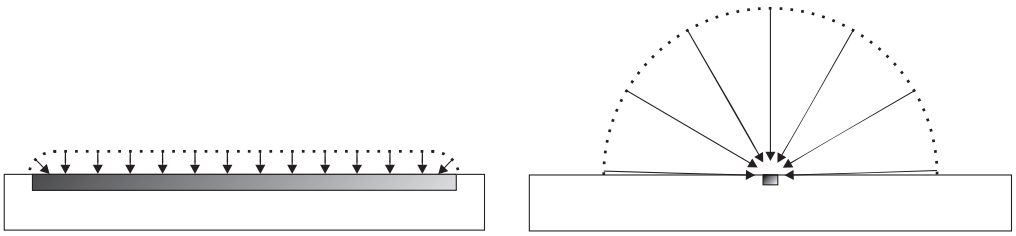
Since the flux of species to the electrode is proportional to the inverse of the extent of the depletion layer, and the current is directly proportional to the flux, it follows that the current is proportional to the square root of the scan rate.

For a fully irreversible system, the Randles-Ševčík equation describing the peak height becomes [1]:

$$|I_\mathrm{p}| = 0.469n\sqrt{\alpha}FAc^*_\mathrm{A}\sqrt{\frac{FD_\mathrm{A}\nu}{RT}} \tag{1.15}$$

1.7 Microelectrodes

A microelectrode is one which is on the micrometer scale in at least one dimension. The discussion of cyclic voltammetry given above is valid for macroelectrodes, as well as microelectrodes where the cyclic voltammetry is conducted at a high scan rate. In these situations, the electrode is large enough such that the depletion layer formed over



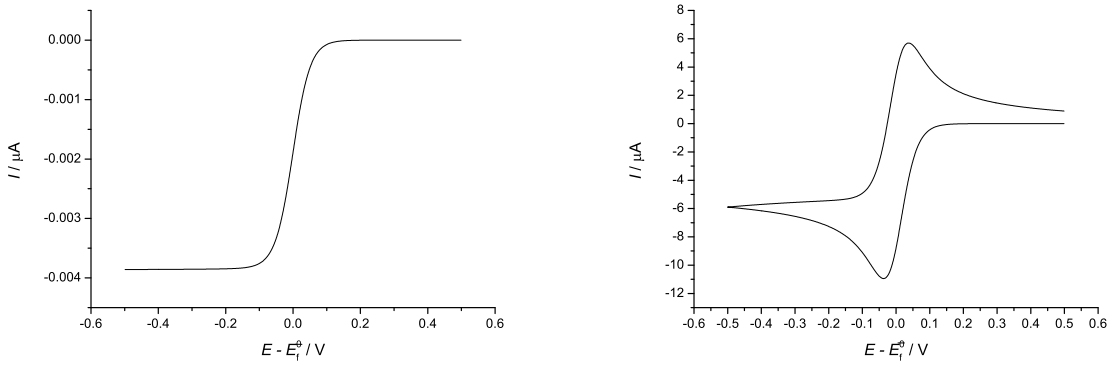
(a) Linear diffusion at a macrodisc (b) Convergent diffusion at a microdisc

Figure 1.5: Schematic cross sections representing diffusion at macro and microelectrodes. Dotted lines represent the edge of the depletion layer, arrows show the direction of diffusion.

the experiment is small compared to the size of the electrode. This being the case, the diffusion to the electrode is planar, as shown in Figure 1.5(a).

If, however, a microelectrode is used, the depletion layer may become very large compared to the electrode size, with the electrode approximating a point at the centre of a large depletion zone. This allows convergent diffusion to the electrode, which is much more efficient than planar diffusion. This is shown schematically in Figure 1.5(b).

This effect leads to the observation of steady state voltammetry in the slow scan rate limit if microdisc or microhemisphere working electrodes are used. This is shown in Figure 1.6. Part (a) of this Figure shows a steady state cyclic voltammogram at a microdisc electrode of radius 1 µm. A steady state current is seen due to the efficient, convergent mass transport. There is also no hysteresis in the response, the signal from the reverse sweep overlays that of the forward sweep. Figure 1.6(b) shows the response from the same system, but this time at a 1 mm radius disc electrode. Transient voltammetry is now seen with pronounced peaks caused by the inefficient, linear diffusion to the electrode surface.



(a) Microdisc (b) Macrodisc

Figure 1.6: Voltammetry at (a) a 1 µm radius disc electrode and (b) a 1 mm radius disc electrode. Other parameters are $c_A = 10$ mM, $D_A = D_B = 1 \times 10^{-9}$ m^2 s^{-1}, $k^0 = 1000$ m s^{-1}, $\alpha = 0.5$, $\nu = 0.001$ V s^{-1}.

1.7.1 Pseudo steady state currents

Microdisc and microhemisphere electrodes are necessarily micro in all their dimesnions (they can be described using a single parameter, their radius). A microband electrode, however, may only be micro in one dimension, its width, and be relatively infinite in length. This leads to efficient diffusion of material in any plane perpendicular to the electrodes length, but not along its length.

This leads to pseudo steady state behaviour, in between the two extremes of transient (macro) and steady state (micro). This is best exemplified by comparing chronoamperometric responses at a microdisc in open solution, a disc of the same area which forms the interior face of a cylinder full of solution, and a microband in open solution.

Chronoamperometry at a microelectrode in open solution is described by the Shoup-Szabo equation, as detailed in Section 1.5.

For the disc electrode at the end of the cylinder, the diffusion will be linear to the electrode surface throughout the whole experiment, since radial diffusion is no longer

possible. The Cottrell Equation is used to describe chornoamperometry for such systems, and for a disc may be written [15]:

$$I = \pi n F D_{\mathrm{A}} c_{\mathrm{A}}^{*} r_{\mathrm{e}} f(\tau) \tag{1.16}$$

$$f(\tau) = \frac{1}{\sqrt{\pi\tau}} \tag{1.17}$$

$$\tau = \frac{D_{\mathrm{A}}}{r_{\mathrm{e}}^{2}} t \tag{1.18}$$

Chronoamperometric responses at microband electrodes were studied extensively by Aoki *et. al.*, and an equation describing the response was developed [16]:

$$I = n F D_{\mathrm{A}} c_{\mathrm{A}}^{*} l_{\mathrm{e}} f(\tau) \tag{1.19}$$

$$f(\tau) = \frac{1}{\sqrt{\pi\tau}} + 0.97 - 1.1\exp\left[\frac{-9.90}{|\ln(12.37\tau)|}\right] \tag{1.20}$$

$$\tau = \frac{D_{\mathrm{A}}}{w_{\mathrm{e}}^{2}} t \tag{1.21}$$

where l_{e} is the length of the microband (m) and w_{e} is its width (m). The band is considered to be infinitely long compared to its width, so convergent diffusion effects at the ends of the band are neglected.

Figure 1.7 shows a log-log plot of $f(\tau)$ as a function of τ for all three situations. Each case shows a similar response at very small values of τ. The diffusion in this situation is planar, there has been very little time for the depletion layer to extend outwards from the electrodes and allow radial diffusion.

At longer times, the microdisc in open solution shows a steady state response, due to the efficient convergent diffusion resulting from the extended depletion layer. The microdisc at the end of the a cylinder shows a linear response over the entire range of τ.

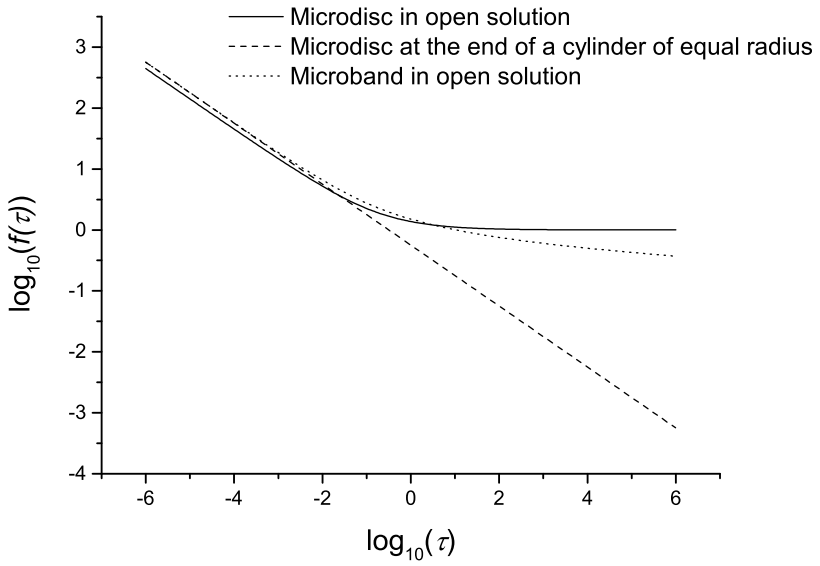


Figure 1.7: Calculated single step chronoamperometric responses for a microdisc in open solution (solid line), a microdisc at the end of a cylinder of equal radius (dashed line) and a microband in open solution (dotted line).

The presence of the cylinder means that convergent diffusion is impossible, the material must reach the electrode from directly above it at all times.

For a microband, however, the convergent diffusion seen at long times is less efficient than for a microdisc, since it only occurs in the plane perpendicular to the electrode length. As such, a true steady state current is not seen.

1.8 Surface bound and thin layer voltammetry

Thus far, the discussion of voltammetry has focused on diffusional systems, where the electrode is placed in a solution containing the electroactive species which is relatively infinite in extent. There is therefore always more electroactive species which can diffuse towards the electrode.

In some cases, however, the electroactive species adsorbs onto the electrode before the

experiment begins. This removes any diffusion effects from the experiment. A typical voltammogram of a surface bound redox couple, for reversible and irreversible electrochemical kinetics, is shown in Figure 1.8. For the reversible case (solid line), it is seen that the peaks are no longer separated, and are centred at the formal potential. Since the species no longer has to diffuse to the electrode, the only factors controlling the current are the applied potential (important for the first half of the wave, where the current increases since not much of species A has been depleted) and the amount of active species left on the surface (important for the second, decreasing half of the wave where most of species A has been used up). The rate at which any species arrives at the electrode is immaterial. If species B, once it has formed, remains adsorbed on the electrode surface, then the same happens on the back scan, but the current has opposite sign.

If the kinetics are slower, then the peaks become separated since a larger overpotential is needed to drive the electron transfer. Otherwise, the same principles apply. This is

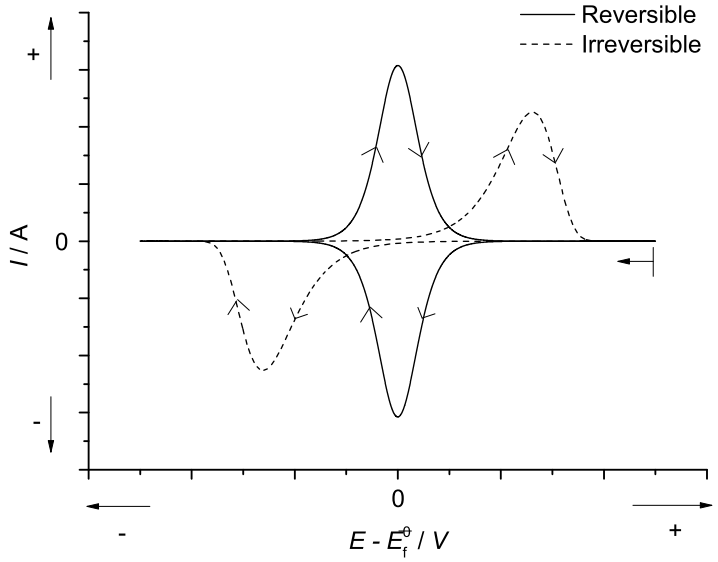


Figure 1.8: Examples of cyclic voltammetry of a surface bound system for reversible (solid line) and irreversible (dashed line) kinetics.

shown as the dashed line in Figure 1.8

In a thin layer system, the working electrode is placed in a cell with dimensions such that only a very thin layer of solution containing the electroactive species may be contained above the electrode. If the cell is small enough, and the scan rate slow enough to ensure the depletion layer fills the whole cell, the same voltammetry is seen as for surface bound species. There is no bulk solution from which the electroactive species may be replenished, and the system behaves as if the species were adsorbed on the electrode.

1.8.1 Effect of scan rate

As we saw earlier (Equation 1.12) the peak height in a diffusional system (for a macrodisc) is proportional to the square root of the scan rate. For a surface bound/thin layer system, the peak height becomes directly proportional to the scan rate. The area under a current-time plot (equal to the charge passed) is directly proportional to the amount of species consumed:

$$Q = nFm \tag{1.22}$$

where Q is the charge passed (C), n is the number of electrons transferred per molecule, and m is the number of moles of electroactive species which underwent electron transfer. Note that this is equally valid for diffusional systems. Running a CV for a surface bound system must produce the same peak area for any scan rate (all of the electroactive species is consumed, and the amount of this is independent of scan rate). Increasing the scan rate by some factor will compress the time axis of a current time plot by the same factor. To maintain the same area, the peak height must correspondingly increase by the same factor. Thus peak height in a surface bound/thin layer system is directly proportional to

scan rate.

1.9 Conclusions

This introductory chapter has provided an overview of mass transport, electrochemical equilibria and electrochemical kinetics. The role these three concepts play in electrochemical experiments has been explored. The following chapter provides an overview of the simulation methods used throughout this thesis.

References

[1] Compton, R. G.; Banks, C. E. *Understanding Voltammetry*, 2nd ed.; World Scientific: Singapore, 2010.

[2] Belding, S. R.; Limon-Petersen, J. G.; Dickinson, E. J. F.; Compton, R. G. *Angew. Chem. Int. Ed.* **2010**, *49*, 9242–9245.

[3] Barnes, E. O.; Wang, Y.; Limon-Petersen, J. G.; Belding, S. R.; Compton, R. G. *J. Electroanal. Chem.* **2011**, *659*, 25 – 35.

[4] Barnes, E. O.; Belding, S. R.; Compton, R. G. *J. Electroanal. Chem.* **2011**, *660*, 185 – 194.

[5] Barnes, E. O.; Wang, Y.; Belding, S. R.; Compton, R. G. *ChemPhysChem* **2012**, *13*, 92 – 95.

[6] Bard, A. J.; Faulkner, L. R. *Electrochemical Methods, Fundamentals and Applications*, 2nd ed.; John Wiley & Sons Inc.: Hoboken, NJ, 2001.

[7] Fick, A. *Annal. Phys. Chem.* **1855**, *94*, 59 – 86.

[8] Butler, J. A. V. *Trans. Faraday Soc.* **1924**, *19*, 729 – 733.

[9] Erdey-Grúz, T.; Volmer, M. *Z. Physik. Chem.* **1930**, *150*, 203–213.

[10] Marcus, R. A. *J. Chem. Phys.* **1956**, *24*, 966–978.

[11] Marcus, R. A. *J. Chem. Phys.* **1957**, *26*, 867 – 871.

[12] Marcus, R. A. *J. Chem. Phys.* **1957**, *26*, 872 – 877.

[13] Shoup, D.; Szabo, A. *J. Electroanal. Chem.* **1982**, *140*, 237 – 245.

[14] Einstein, A. *Ann. Phys.* **1905**, *17*, 549 – 560.

[15] Cottrell, F. G. *Z. Physik. Chem.* **1903**, *42*, 385 – 431.

[16] Aoki, K.; Tokuda, K.; Matsuda, H. *J. Electroanal. Chem.* **1987**, *230*, 61 – 67.

Chapter 2

Simulation Methods

This thesis is concerned with the simulation of electrochemical experiments. Simulation is often essential to extract important information from experimental data, such as k^0 and diffusion coefficients. Only for the simplest systems can this be done analytically, for example by using the Cottrell equation for chronoamperometry at a planar electrode [1] or a (hemi)spherical electrode [2], or steady state voltammetry [2, 3]. More complex "real" problems, such as transient cyclic voltammetry, require numerical simulation to produce a voltammogram. The following chapter outlines the numerical techniques used in this thesis to simulate electrochemical experiments.

2.1 Constructing the model

There are two generic ways in which to simulate an electrochemical experiment. A random walk model may be used, where the position and movement of individual molecules are tracked as they undergo random Brownian motion. As the molecules impact on the electrode they then may undergo electron transfer, resulting in a current. This method has been successfully applied to simulate both chronoamperometry [4–7] and cyclic voltammetry [8]. While a random walk model can provide insight into the electrochemistry of

systems with an extremely low concentration of electroactive species [8], the necessity of keeping track of extremely large numbers of molecules renders this method extremely slow computationally.

An alternative method is to solve Fick's second law (Equation 1.2) over a simulation space subject to appropriate boundary conditions, to obtain a concentration profile which evolves with time. The form of the simulation space will depend on the geometry of the system being simulated, and the boundary conditions are defined by both the geometry and the kind of experiment being simulated. The appropriate form of Fick's law, the simulation space and the boundary conditions will all be defined on a case by case basis as needed throughout this thesis.

2.2 The finite difference method

Fick's second law may only be solved analytically in the simplest of cases, for example single step chronoamperometry at an infinite planar electrode. For more complex situations, such as double potential step chronoamperometry or cyclic voltammetry, no analytical solution exists and a solution must be found using numerical methods.

A variety of numerical methods exist to solve partial differential equations such as Fick's second law. Within electrochemistry, the two most popular are the finite element method and the finite difference method. The finite element method involves dividing space up into individual tessellating cells, for example triangles in 2D space or tetrahedra in 3D space. Concentration profiles can then be fitted across each cell, and summed up to give an overall concentration profile across all of the space. The main advantage of this method is that it can be used to model complex and intricate geometries. It is, however,

quite difficult to implement [9, 10].

Throughout this thesis, the finite difference method is employed to solve Equation 1.2 numerically. This method approximates continuous derivatives of some function $f(x)$ as linear gradients between discrete points in space. There are three ways to approximate the first derivative of $f(x)$ at some point x_j, (denoted as $f'(x_j)$): the upwards ($f'(x_j)^+$), central ($f'(x_j)^0$) and downwards ($f'(x_j)^-$) methods. These are given respectively by:

$$f'(x_j)^+ \approx \frac{f(x_{j+1}) - f(x_j)}{x_{j+1} - x_j} \tag{2.1}$$

$$f'(x_j)^0 \approx \frac{f(x_{j+1}) - f(x_{j-1})}{x_{j+1} - x_{j-1}} \tag{2.2}$$

$$f'(x_j)^- \approx \frac{f(x_j) - f(x_{j-1})}{x_j - x_{j-1}} \tag{2.3}$$

These approximations become more accurate as steps between successive values of x_j become smaller [11].

Where possible, the centrally differenced method is used throughout this thesis, as it is more accurate than the upwards or downwards methods. Assuming (for simplicity) that:

$$x_j - x_{j-1} \approx x_{j+1} - x_{j1} = \Delta \tag{2.4}$$

then two Taylor expansions can be written:

$$f(x_{j+1}) = f(x_j) + \frac{f'(x_j)}{1!}\Delta + \frac{f''(x_j)}{2!}\Delta^2 + \frac{f'''(x_j)}{3!}\Delta^3 ... \tag{2.5}$$

$$f(x_{j-1}) = f(x_j) - \frac{f'(x_j)}{1!}\Delta + \frac{f''(x_j)}{2!}\Delta^2 - \frac{f'''(x_j)}{3!}\Delta^3 ... \tag{2.6}$$

Equation 2.5 can be rearranged to:

$$f'(x_j) = \frac{f(x_{j+1}) - f(x_j)}{\Delta} - \frac{f''(x_j)}{2}\Delta - ... \quad (2.7)$$

$$f'(x_j) = f'(x_j)^+ - \frac{f''(x_j)}{2}\Delta - ... \quad (2.8)$$

Therefore the true differential is equal to that calculated using the upwards differenced method minus extra terms of order Δ. Applying the same logic to the downwards differenced method produces the same result. Hence, these two methods have error $\mathcal{O}(\Delta)$

To evaluate the error in the centrally differenced method, Equation 2.6 is subtracted from Equation 2.5 to yield:

$$f(x_{j+1}) - f(x_{j-1}) = 2f'(x_j)\Delta + \frac{2f'''(x_j)}{3!}\Delta^3 + ... \quad (2.9)$$

which rearranges to:

$$f'(x_j) = \frac{f(x_{j+1}) - f(x_{j-1})}{2\Delta} - \frac{2f'''(x_j)}{3!}\Delta^2 - ... \quad (2.10)$$

$$f'(x_j) = f'(x_j)^0 - \frac{2f'''(x_j)}{3!}\Delta^2 - ... \quad (2.11)$$

Thus, the centrally differenced method has error $\mathcal{O}(\Delta^2)$. Since the upwards and downwards methods have error $\mathcal{O}(\Delta)$, the centrally differenced method will be more accurate if $\Delta < 1$.

Second derivatives can be approximated as the derivative of the first derivative, *i.e.*:

$$f''(x_j) \approx \frac{\frac{f(x_{j+1})-f(x_j)}{x_{j+1}-x_j} - \frac{f(x_j)-f(x_{j-1})}{x_j-x_{j-1}}}{0.5(x_{j+1} - x_{j-1})} \quad (2.12)$$

2.3 Explicit and implicit methods

In linear space, Fick's second law for a particular species is given by:

$$\frac{\partial c}{\partial t} = D\frac{\partial^2 c}{\partial x^2} \tag{2.13}$$

We must use one of the upwards, central or downwards finite difference methods to discretise the left hand side of this equation. Since concentrations at the current time step (denoted k) are known, we and are aiming to calculate the concentration at the next time step $(k+1)$, the upwards method must be used:

$$\frac{\partial c}{\partial t} \approx \frac{c_j^{k+1} - c_j^k}{t^{k+1} - t^k} \tag{2.14}$$

The right hand side of Equation 2.13 is spatially discretised using Equation 2.12. There is, however, a choice of which timestep to use, either k or $k+1$. Using the former is referred to as the *explicit* method, the latter is the *implicit* method. Using these two methods, Equation 2.13 can be rewritten as:

$$\text{Explicit:} \quad \frac{c_j^{k+1} - c_j^k}{t^{k+1} - t^k} = D\left(\frac{\frac{c_{j+1}^k - c_j^k}{x_{j+1} - x_j} - \frac{c_j^k - c_{j-1}^k}{x_j - x_{j-1}}}{0.5\left(x_{j+1} - x_{j-1}\right)}\right) \tag{2.15}$$

$$\text{Implicit:} \quad \frac{c_j^{k+1} - c_j^k}{t^{k+1} - t^k} = D\left(\frac{\frac{c_{j+1}^{k+1} - c_j^{k+1}}{x_{j+1} - x_j} - \frac{c_j^{k+1} - c_{j-1}^{k+1}}{x_j - x_{j-1}}}{0.5\left(x_{j+1} - x_{j-1}\right)}\right). \tag{2.16}$$

At first glance, the explicit method seems the easier. Knowing all the values of c_{j-1}^k, c_j^k and c_{j+1}^k, it is a simple matter to calculate the one unknown c_j^{k+1}. However, this method has stringent stability requirements [12]. If the value of $t^{k+1} - t^k$ is too small compared to $x_j - x_{j-1}$ and $x_{j+1} - x_j$, the result given by the equation will diverge away from the true

result. This requirement often involves prohibitively small values of $t^{k+1} - t^k$, resulting in unacceptably long simulation times.

The implicit scheme is, however, unconditionally stable [12]. The disadvantage is that there are now three unknowns in the equation, c_{j+1}^{k+1}, c_j^{k+1} and c_{j-1}^{k+1}. The equation must then be solved simultaneously over all n spatial points (subject to boundary conditions). This gives n equations with n unknowns.

Equation 2.16 can be rewritten as:

$$\alpha_j c_{j-1}^{k+1} + \beta_j c_j^{k+1} + \gamma_j c_{j+1}^{k+1} = \delta c_j^k \tag{2.17}$$

where:

$$\alpha_j = \frac{-D}{0.5\,(x_j - x_{j-1})\,(x_{j+1} - x_{j-1})} \tag{2.18}$$

$$\gamma_j = \frac{-D}{0.5\,(x_{j+1} - x_j)\,(x_{j+1} - x_{j-1})} \tag{2.19}$$

$$\delta = \frac{1}{t^{k+1} - t^k} \tag{2.20}$$

and:

$$\beta_j = \delta - \alpha_j - \gamma_j \tag{2.21}$$

The n simultaneous equations can then be written in matrix form:

$$\begin{pmatrix} \ddots & \vdots & \vdots & \vdots & \vdots & \vdots & \iddots \\ \cdots & \alpha_{j-1} & \beta_{j-1} & \gamma_{j-1} & 0 & 0 & \cdots \\ \cdots & 0 & \alpha_j & \beta_j & \gamma_j & 0 & \cdots \\ \cdots & 0 & 0 & \alpha_{j+1} & \beta_{j+1} & \gamma_{j+1} & \cdots \\ \iddots & \vdots & \vdots & \vdots & \vdots & \vdots & \ddots \end{pmatrix} \begin{pmatrix} \vdots \\ c_{j+1}^{k+1} \\ c_j^{k+1} \\ c_{j-1}^{k+1} \\ \vdots \end{pmatrix} = \delta \begin{pmatrix} \vdots \\ c_{j+1}^{k} \\ c_j^{k} \\ c_{j-1}^{k} \\ \vdots \end{pmatrix} \tag{2.22}$$

more simply written:

$$\mathbf{XU} = \mathbf{V} \tag{2.23}$$

The elements of the vector $\mathbf{U}$ are the only unknowns in these simultaneous equations. $\mathbf{U}$ can be calculated using the Thomas Algorithm [12–14], an efficient method for solving simultaneous equations in tridiagonal matrix form. The method can also be easily generalised for n-diagonal matrices, as required when more than one species in solution needs to be considered.

In this manner, knowing the values of the concentration at the first time step over all space, c_j^0, equation 2.23 may be solved, subject to boundary conditions, to find c_j^1, and these new concentrations fed back into $\mathbf{V}$ for the next time step.

2.4 The Newton-Rapshon method

The above method is able to provide an exact solution to a set of discretised linear simultaneous equations, where the equations may be cats as a linear combination of unknown variables to be calculated. If, however, the set of equations to be solved is non-linear, the iterative Newton-Raphson method may be used to arrive at an approximate

solution [14].

If some function is expressed as $f(x) = 0$, and an initial guess at the value of x is made x_0, we would like to know how much to change this guess by to get a better estimate. Consider the Taylor expansion:

$$f(x_0 + u) = f(x_0) + u\frac{\partial f(x_0)}{\partial x} + ... \tag{2.24}$$

$$= 0 \tag{2.25}$$

This can be extended to a function of n variables x_0, x_1, ... x_{n-1} written as a vector:

$$f(\mathbf{x_0} + \mathbf{u}) = f(\mathbf{x_0}) + \sum_n u_n \frac{\partial f(\mathbf{x_0})}{\partial x_n} + ... \tag{2.26}$$

Since we want $f(\mathbf{x_0} + \mathbf{u})$ to be equal to zero:

$$\sum_n u_n \frac{\partial f(\mathbf{x_0})}{\partial x_n} = -f(\mathbf{x_0}) \tag{2.27}$$

ignoring higher order terms.

This can be extended if there are n simultaneous equations for each of these n variables. For each of the n functions (labelled m):

$$\sum_n u_n \frac{\partial f_m(\mathbf{x_0})}{\partial x_n} = -f_m(\mathbf{x_0}) \tag{2.28}$$

which may be expressed in matrix form:

$$\mathbf{J}\mathbf{u} = -\mathbf{f}\left(\mathbf{x_0}\right) \tag{2.29}$$

J is a square $n \times n$ matrix where the element of the m^{th} row and n^{th} column is:

$$J_{mn} = \frac{\partial f_m}{\partial x_n} \tag{2.30}$$

These simultaneous equations may then be solved using the Thomas Algorithm (since **J** will be diagonal for finite difference problems). The initial guess of the unknowns are then augmented by the elements of **u** and the process repeated. This continues until the elements of **u** are small enough to make no significant change to the unknowns (in this thesis values less than 10^{-4} are used). These final values of **x** are then used as the initial guess for the next time step up.

2.5 The alternating direction implicit method

The discussion thus far has been limited to one dimensional systems, and is applicable to macrodisc electrodes and hemispherical electrodes. However, to model electrochemistry at, for example, a microdisc, a two dimensional model is needed.

Fick's second law in two dimensional Cartesian space is given by:

$$\frac{\partial c}{\partial t} = D\left(\frac{\partial^2 c}{\partial x^2} + \frac{\partial^2 c}{\partial y^2}\right) \tag{2.31}$$

An efficient way to solve a two dimensional problem such as this is to split each time step in half, and solve the equations first implicitly in the x dimension and explicitly in the y, then the other way around in the second half of the time step. This is called the alternating direction implicit (ADI) method.

2.6 Dimensionless parameters

Once a model has been developed from the appropriate mass transport equation and boundary conditions, it is convenient to normalise that model by introducing a set of dimensionless parameters. This reduces the number of independent variables by expressing all concentrations and diffusion coefficients relative to the values for the first species of a given mechanism. Similarly, all distances are given relative to the electrode radius/width. A full list of dimensionless parameters used throughout this thesis, and their definitions, is given in the Glossary.

2.7 Spatial and temporal grids

In order to solve the discretised mass transport equation numerically, spatial and temporal grids must be defined to solve the equation over (subject to boundary conditions).

In electrochemical experiments, concentration gradients are steepest near the interface where the electron transfer takes place. In order to maintain accuracy, a dense spatial grid consisting of closely separated points is therefore needed in the region close to the electrode surface. Having a dense grid across the whole simulation space is, however, computationally inefficient. Since there will only be very small concentration gradients far from the electrode, fewer spatial points are needed. Spatial grids in this thesis therefore consist of closely spaced points near the electrode surface, which expand to more sparse grids away from the electrode. Exact mathematical forms of these grids are given on a case by case basis throughout this thesis.

The type of temporal grid employed depends on the nature of the experiment being carried out. In a chronoamperometry experiment, the most dramatic changes in con-

centration occur soon after the start of the experiment, necessitating a dense temporal grid shortly after $t = 0$. At longer times, however, the concentration changes become smaller and smaller, and steady state may eventually be reached where the concentration no longer changes at all. Only a sparse grid is therefore required at longer times. For chronoamperometry, therefore, a similar grid to the spatial one is employed, which is initially dense but expands to a sparse one at longer times.

For cyclic voltammetry, concentration changes occur the varying degrees across the whole voltammogram. It is therefore most efficient to used a regular array of temporal grid points which does not expand. Again, details of the grids used will be given on a case by case basis.

References

[1] Cottrell, F. G. *Z. Physik. Chem.* **1903**, *42*, 385 – 431.

[2] Compton, R. G.; Banks, C. E. *Understanding Voltammetry*, 2nd ed.; Imperial College Press: London, 2011.

[3] Molina, A.; Gonzalez, J.; Barnes, E. O.; Compton, R. G. *J. Phys. Chem. C.* **2014**, *118*, 346 – 356.

[4] Nagy, G.; Sugimoto, Y.; Denuault, G. *J. Electroanal. Chem.* **1997**, *433*, 167 – 173.

[5] Baur, J. E.; Motsegood, P. N. *J. Electroanal. Chem.* **2004**, *572*, 29 – 40.

[6] Cutress, I. J.; Dickinson, E. J. F.; Compton, R. G. *J. Electroanal. Chem.* **2011**, *655*, 1 – 8.

[7] Kätelhön, E.; Barnes, E. O.; Krause, K. J.; Wolfrum, B.; Compton, R. G. *Chem. Phys. Lett.* **2014**, *595*, 31 – 34.

[8] Cutress, I. J.; Compton, R. G. *Chem. Phys. Let.* **2011**, *508*, 306–313.

[9] Cutress, I. J.; Dickinson, E. J. F.; Compton, R. G. *J. Electroanal. Chem.* **2010**, *638*, 76 – 83.

[10] Dickinson, E. J. F.; Ekström, H.; Fontes, E. *Electrochem. Commun.* **2014**, *40*, 71 – 74.

[11] Britz, D. *Digital Simulation in Electrochemistry*; Springer-Verlag: Heidelberg, 2005.

[12] Compton, R. G.; Laborda, E.; Ward, K. R. *Understanding Voltammetry: Simulation of Electrode Processes*; Imperial College Press: London, 2014.

[13] Compton, R. G.; Pilkington, M. B. G.; Stearn, G. M. *J. Chem. Soc., Faraday Trans. 1* **1988**, *84*, 2155–2171.

[14] Press, W. H.; Teukolsky, S. A.; Vetterling, W. T.; Flannery, B. P. *Numerical Recipes: The Art of Scientific Computing*, 3rd ed.; Cambridge University Press: Cambridge, 2007.

Chapter 3

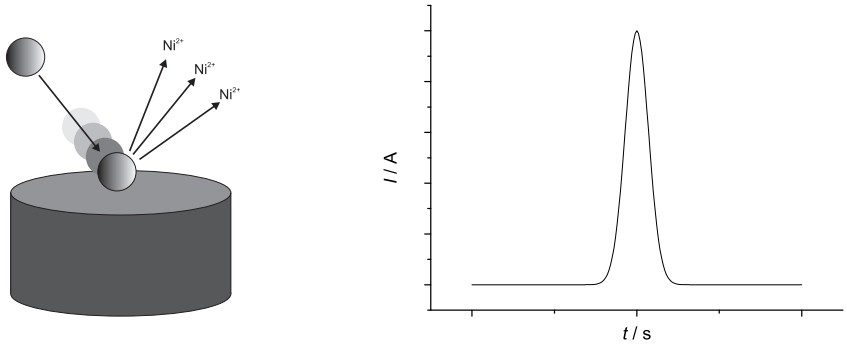
The Effect of Hindered Diffusion on the Electrochemistry of Nanoparticles

This chapter investigates the influence of near wall hindered diffusion on the destructive oxidation of spherical nanoparticles, and a computational model is developed to include near wall hindered diffusion effects. It is shown that this more complete picture is able to successfully simulate the experimental anodic particle coulometry of nickel nanoparticles. This work has been published in *The Journal of Electroanalytical Chemistry* [1]. Experiments were carried out by Dr. Yige Zhou.

3.1 Introduction

The detection and characterisation of metal nanoparticles is of great importance due to their potentially toxic effects on human health [2, 3] and the environment [4, 5]. In order to detect nanoparticles electrochemically, an understanding of their mass transport properties and mechanisms of oxidation is important.

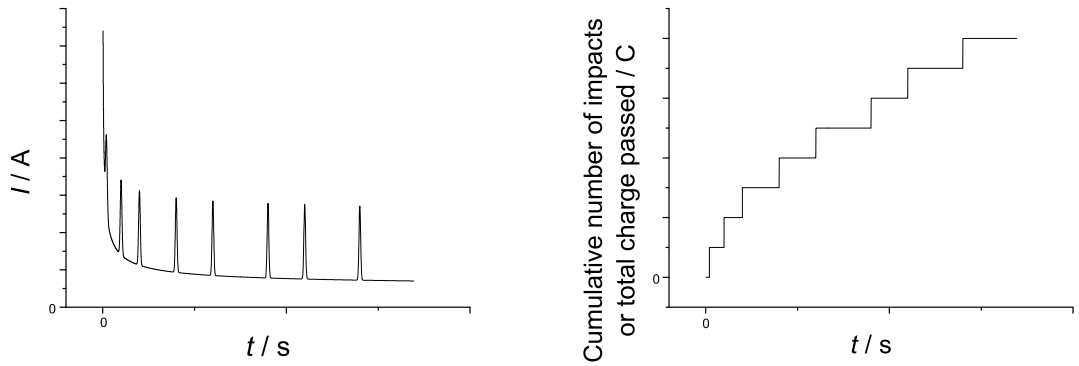
Nanoparticle impact experiments were pioneered by Heyrovský and Jirovský in 1995 [6–9], and have been developed in recent years to directly extract information about nanoparticles in solution. Anodic particle coulometry' (APC) has been used to charac-



(a) An impact event (b) Current time plot

Figure 3.1: Schematic diagrams of (a) an oxidative impact of a nickel nanoparticle and (b) the resulting current time plot.

terise gold [10], silver [11, 12], nickel [12] and copper [13] nanoparticles. In these experiments, a potential step is applied to an electrode in a solution containing nanoparticles from a potential where no current is measured to one where oxidation and dissolution of the nanoparticles occurs at a mass transport controlled rate, and the current passed measured as a function of time. When a nanoparticle approaches the electrode and is oxidised, a spike in the measured current is seen. This is shown schematically for a nickel nanoparticle in Figure 3.1. The frequency of and charge under the spikes yields information about the nanoparticles under study. Measuring the charge passed gives information on the number of atoms in a nanoparticle, and hence its size and the degree of aggregation between nanoparticles. In the case of silver [11] and gold [10] this analysis showed significant aggregation occurring between nanoparticles, but not in the case of nickel [12]. Figure 3.2 (a) shows a schematic of typical nanoparticle APC experimental results. The area under the spikes corresponds to the charge transferred during the impact event. Figure 3.2 (b) shows a schematic of the cumulative number of spikes observed and total charge passed over time in an APC experiment (the charge passed is the integral of the



(a) (b)

Figure 3.2: (a) Schematic of a nanoparticle APC experiment. Each spike corresponds to a nanoparticle impact. (b) Schematic of the cumulative number of spikes or the total charge passed as a function of time.

current time plot minus the background current, or the cumulative number of spikes observed times the charge passed per nanoparticle oxidation). It has been shown that an analysis of the cumulative number of spikes observed over time can be used to estimate an unknown concentration of nanoparticles [12].

These previous electrochemical studies have assumed that the diffusion coefficient of nanoparticles of a given size is constant, whether the nanoparticle is near the electrode surface or in bulk solution. However, it has been shown theoretically [14–16] and experimentally [17–19] that this is not the case, and that the diffusion of spherical particles in solution is hindered near a solid wall, due to hydrodynamic drag [18]. The diffusion coefficients must be multiplied by a hindrance factor:

$$D(r) = \psi D(\infty) \tag{3.1}$$

where $D(r)$ is the diffusion coefficient at distance r from the wall, $D(\infty)$ is the diffusion coefficient infinitely far from the wall (given by the Stokes-Einstein equation), and ψ is

the hindrance factor. For motion perpendicular to a wall, the hindrance factor is given by:

$$\psi = \frac{6h^2 + 2r_{\mathrm{NP}}h}{6h^2 + 9r_{\mathrm{NP}}h + 2r_{\mathrm{NP}}^2} \tag{3.2}$$

where r_{NP} is the radius of the nanoparticle, and h is the distance between the edge of the nanoparticle and the wall. Note that, when r_{NP} is zero, ψ is equal to 1 for all values of h. It is reasonable to expect that this must affect the analysis of the electrochemistry of nanoparticles, and this chapter investigates whether or not this is the case.

In this chapter, we study the APC of nickel nanoparticles (NiNPs), and develop a more complete computational model to simulate these experiments, including near-wall hindered diffusion in the model for destructive oxidation of the nanoparticles. The model is used to successfully simulate APC experiments by measuring the flux of nanoparticles approaching the electrode.

3.2 Theory

We develop a model to simulate the destructive oxidation of nanoparticles, via anodic particle coulometry (APC), including the effects of hindered diffusion at a hemispherical electrode. In an APC experiment, the potential applied to the electrode is stepped from one where no oxidation occurs, to one where oxidation is mass transport controlled.

Approximating the nanoparticle mass transport to behave in a statistical manner [20, 21] we can apply Fick's second law (in spherical coordinates) and avoid time consuming stochastic calculations:

$$\frac{\partial c}{\partial t} = \nabla \left(D \nabla c \right) \tag{3.3}$$

which in spherical space, and assuming D is a function of r, is given by:

$$\frac{\partial c}{\partial t} = D\left(\frac{\partial^2 c}{\partial r^2} + \frac{2}{r}\frac{\partial c}{\partial r}\right) + \frac{\partial D}{\partial r}\frac{\partial c}{\partial r} \tag{3.4}$$

where c is concentration, t is time, r is the radial distance from the centre of the electrode, and D is the diffusion coefficient. All symbols are defined in the Glossary.

Since we are using a Fickian model of diffusion rather than a stochastic one, the simulations will generate a smooth, continuous current rather than discrete impact spikes. We can convert the current produced into the cumulative number of impact spikes expected in a simple way. The current, I, can be converted into a number of particles per second, P:

$$P = \frac{N_A I}{F} \tag{3.5}$$

where N_A is the Avogadro constant. This direct proportionality means that the currents produced by the simulations can readily be thought of as directly reflecting impact spike frequency. The cumulative number of impact spikes expected in the APC experiment at time t, $N(t)$, can then be calculated by integrating P with respect to t:

$$N(t) = \int_0^t P \mathrm{d}t \tag{3.6}$$

The total charge passed in an experiment is then given by the cumulative number of impact events multiplied by the charge passed during a single impact event.

D is considered to vary with radial distance from the electrode [14–16]:

$$\frac{D(r)}{D^{\mathrm{bulk}}} = \frac{6h^2 + 2r_{\mathrm{NP}}h}{6h^2 + 9r_{\mathrm{NP}}h + 2r_{\mathrm{NP}}^2} \tag{3.7}$$

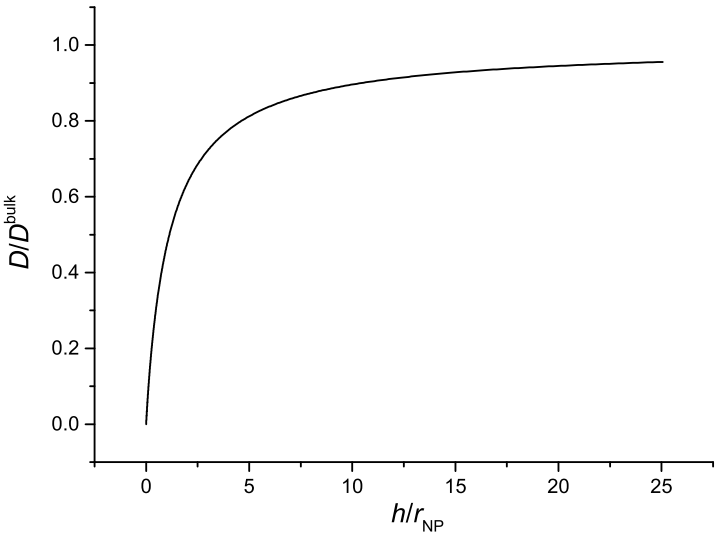


Figure 3.3: Variation of D relative to its bulk value as a function of h/r_{NP}.

where D^{bulk} is the diffusion coefficient in bulk solution far from the electrode, r_{NP} is the radius of the nanoparticle, and h is the distance between the edge of the nanoparticle and the electrode surface (*i.e.* if the nanoparticle is centred at r, then $h = r - r_{\mathrm{NP}} - r_e$). Figure 3.3 shows the variation of D/D^{bulk} with h/r_{NP}. This equation has been shown to be a good approximation using a variety of experimental methods [17–19].

We need to consider the flux of species at the electrode surface, required for calculating the current. In most electrochemical simulations the flux would be given by the expression

$$j = D\left(\frac{\partial c}{\partial r}\right)_{r=r_e} \tag{3.8}$$

However, using Equation 3.7 to calculate the variable diffusion coefficient, we find that D at the electrode surface is zero, and hence the flux at the electrode surface will always be zero on the basis of Equation 3.8.

There are two possible ways to solve this problem. One is to include quantum me-

chanical tunnelling in the model. The tunnelling process is not confined to the electrode surface, and has a distance dependent rate equation [22]:

$$\text{rate} = \nu \mathrm{e}^{-\beta' r} \tag{3.9}$$

where ν is a pre exponential constant and β' is the tunnelling constant, dependent on the medium in which tunnelling is taking place. This will reduce the size of the particles at a rate dependent on their distance from the electrode, until they disappear completely. However, this produces a complex problem to be solved where there are two variables, concentration of nanoparticles and their size, to find. Each size of nanoparticle will also have a different diffusion coefficient (due to the Stokes-Einstein equation, see below). A simpler model would be desirable.

While we cannot measure the flux directly at the electrode surface, we can measure the flux at very small distances close to it. However, the value of $r^2 D \frac{\partial c}{\partial r}$ is constant beyond a certain tiny distance from the electrode. The limiting value of the flux as it approaches the surface is therefore used as a measure of the flux in this model.

3.2.1 Dimensionless parameters

Dimensionless parameters are introduced into the model to remove scaling factors such as concentration and electrode radius, as discussed in Chapter 2. A full list with definitions is given in the Glossary. Introducing these parameters into the mass transport equation:

$$\frac{\partial C}{\partial \tau} = D' \left(\frac{\partial^2 C}{\partial R^2} + \frac{2}{R} \frac{\partial C}{\partial R} \right) + \frac{\partial D'}{\partial R} \frac{\partial C}{\partial R} \tag{3.10}$$

3.2.2 Boundary conditions

Initial conditions are defined as:

$$\tau < 0; \quad \text{all } R; \quad C = 1 \tag{3.11}$$

since the nanoparticles are present at bulk concentration throughout the solution before any potential step is applied.

At $\tau > 0$, since the particles are oxidised at a mass transport controlled rate, we can say $C = 0$ at the electrode surface:

$$C_{R=1} = 0 \tag{3.12}$$

The outer edge of the simulation space, $R_{\max}$ is defined as:

$$R_{\max} = 6\sqrt{\tau_{\max}} \tag{3.13}$$

which is well outside the depletion layer of an experiment lasting time $\tau_{\max}$ [23–25]. Note that the usual maximum dimensionless diffusion coefficient is not present in this equation. Since we are only considering one species, and its maximum dimensionless diffusion coefficient (in bulk solution) is 1, this parameter is redundant in this instance. At this limit, we set the concentration at its bulk value:

$$C_{R=R_{\max}} = 1 \tag{3.14}$$

These boundary conditions are summarised in Table 3.1.

To calculate the current, we calculate the dimensionless flux using the method dis-

Boundary		Condition
$\tau < 0$	all R	$C = 1$
$\tau \geq 0$	$R = 1$	$C = 0$
	$R = R_{\max}$	$C = 1$

Table 3.1: Dimensionless boundary conditions for an APC experiment at a hemispherical electrode

cussed above, taking the value at a short distance from the electrode surface R':

$$J = R^2 D' \left(\frac{\partial C}{\partial R}\right)_{R=R'} \tag{3.15}$$

A suitable value for R' is discussed below. The (dimensional) current is then calculated using:

$$I = 2\pi n F D c^* r_e J \tag{3.16}$$

This current may then be converted to a cumulative number of spikes by calculating the number of particles per second and integrating with respect to time, as discussed above.

3.2.3 Numerical methods

The mass transport equation and boundary condition are discretised using the methods outlined in Chapter 2 and solved simultaneously over all space.

As discussed in Chapter 2, it is necessary to discretise the spatial and temporal domains over which the equations are solved. For the spatial grid, an initial value of R at the electrode surface (R_0) is defined as 1. The next grid point, R_1, is set at an extremely

small distance δR from the electrode. There is then a regular grid from R_2 up to some switching value, R_s, after which the grid expands. The grid can be defined mathematically as:

$$R_0 = 1 \tag{3.17}$$

$$R_1 = \delta R \tag{3.18}$$

$$R_\mathrm{j} = R_{\mathrm{j}-1} + \Delta R \qquad \delta R < R < R_\mathrm{s} \tag{3.19}$$

$$R_\mathrm{j} = \gamma_R R_{\mathrm{j}-1} \qquad R_\mathrm{s} \leq R \tag{3.20}$$

The temporal grid is also defined as initially linear, then expanding past some switching value, τ_s:

$$\tau_0 = 0 \tag{3.21}$$

$$\tau_\mathrm{k} = \tau_{\mathrm{k}-1} + \Delta\tau \qquad 0 < \tau < \tau_\mathrm{s} \tag{3.22}$$

$$\tau_\mathrm{k} = \gamma_\tau \tau_{\mathrm{k}-1} \qquad \tau_\mathrm{s} \leq \tau \tag{3.23}$$

Convergence studies found grid parameters of $\delta R = 1\times10^{-11}$, $\Delta R = 1\times10^{-7}$, $R_\mathrm{s} = 1.0001$, $\gamma_R = 1.01$, $\Delta\tau = 1\times10^{-9}$, $\tau_\mathrm{s} = 1\times10^{-4}$, $\gamma_\tau = 1.001$ gave simulations converged to within 0.2% of fully converged results in the range $1\times10^{-8} < \tau < 1\times10^{5}$.

Equations were solved using the Thomas Algorithm for a diagonal matrix [26]. The program was coded in C++ and run on a desktop computer (Intel Core 2 Quad 2.4 Ghz, 2 GB RAM) with a typical running time of a five minutes per simulation.

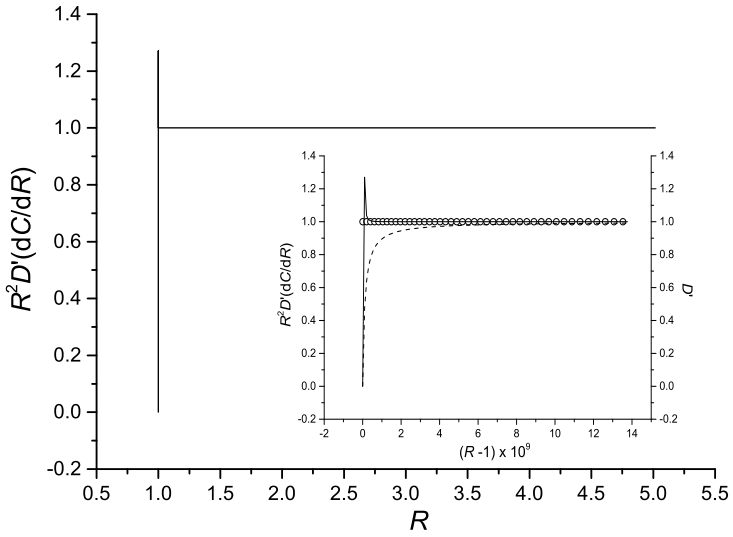


Figure 3.4: Variation of dimensionless flux with distance for nanoparticles of size $R_{\mathrm{NP}} = 1 \times 10^{-10}$ at dimensionless time $\tau = 10^6$. Inset shows the region very close to the electrode, where the flux for nanoparticles of zero size (no hindered diffusion) is shown by circles for comparison. Also shown is the hindered dimensionless diffusion coefficient for the nanoparticles (dashed line).

3.3 Simulated results and discussion

3.3.1 Measuring the flux

Using the model described above, we are able to simulate the oxidative dissolution of nanoparticles after a potential step, *i.e.* an APC experiment, and calculate the flux of nanoparticles as a function of time after the potential step. However, as discussed above, the flux cannot be evaluated at the electrode surface, as is usually the case in electrochemical simulations, since the diffusion coefficient here is zero. Instead, we must measure the limiting value of the flux approaching the electrode.

Figure 3.4 shows the value of $R^2 D'(\frac{\partial C}{\partial R})$ as a function of radial coordinate R at $\tau = 10^6$ after the potential step (steady state) for dimensionless particle radius $R_{\mathrm{NP}} = 10^{-10}$. Inset

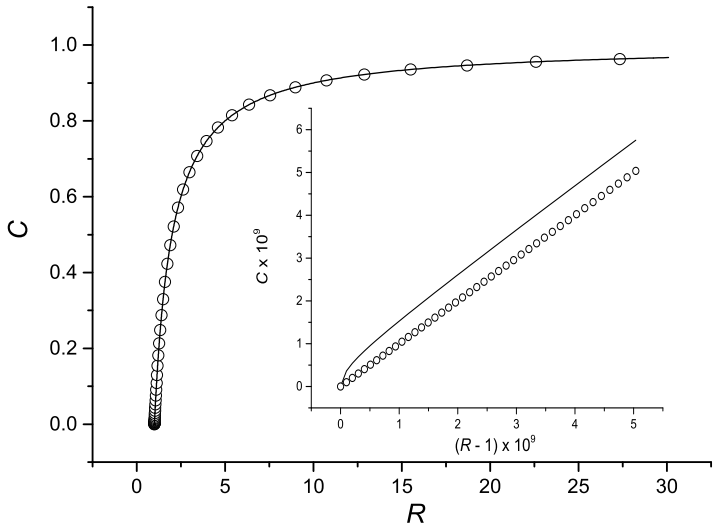


Figure 3.5: Variation of concentration with distance for nanoparticles of size $R_{\mathrm{NP}} = 1 \times 10^{-10}$ (solid line) and $R_{\mathrm{NP}} = 0$ (circles) at dimensionless time $\tau = 10^6$. Inset shows the region very close to the electrode

is the region very close to the electrode surface, with a comparison to the case where there is no hindered diffusion ($R_{\mathrm{NP}} = 0$, mimicking molecular behaviour where the diffusion coefficient is the same over the entire solution). Also shown in the inset is the variation with R of the diffusion coefficient close to the electrode surface (dashed line). The no hindered diffusion case shows a constant flux of unity from the electrode surface out into solution, as is expected. If the nanoparticles have a size, however, we see zero flux at the electrode surface, which then very quickly attains a constant value of unity. A short sharp peak in the apparent flux very close to the electrode surface is a result of the limitations of the spatial grid used in the simulations. Beyond this peak however, the dimensionless flux has a constant value of unity. Therefore, the limiting value of the flux as the radial

coordinate approaches one is used as a measure of the nanoparticle flux:

$$J = \lim_{R \to 1} \left(R^2 D' \frac{\partial C}{\partial R} \right) \tag{3.24}$$

Figure 3.5 shows the concentration profile for the same situation described above ($\tau = 10^6$ after the potential step in an APC experiment, $R_{\mathrm{NP}} = 10^{-10}$). Again, for comparison the case where $R_{\mathrm{NP}} = 0$ (mimicking molecular behavior with no hindered diffusion effects) is shown by circles. It is seen that over large distances, there is no difference between the two concentration profiles, showing that these very small nanoparticles behave as molecules do. Very close the the electrode however (inset in Figure 3.5) we see the hindered diffusion case has a slightly higher concentration than the non hindered case. The zero diffusion coefficient at the electrode surface causes a build up of material adjacent to the surface, causing a slightly higher concentration than when diffusion is unhindered.

Figure 3.6 shows the percentage error in simulated dimensionless steady state flux for various values of δR, the point at which the flux is recorded, for $R_{\mathrm{NP}} = 0.1$. It is seen that as δR approaches zero, the error increases drastically, up to values in excess of 20% (not shown for clarity). $R = 1 + 2 \times 10^{-9}$ was found to be an appropriate radial coordinate to measure the limiting flux of particles for particles of radius $R_{\mathrm{NP}} < 0.1$ for times $\tau > 1 \times 10^{-7}$.

3.3.2 Effect of particle size

Larger nanoparticles will have a hindered diffusion region that extends further out into solution than smaller ones, thus having a greater effect on the concentration profiles and measured flux.

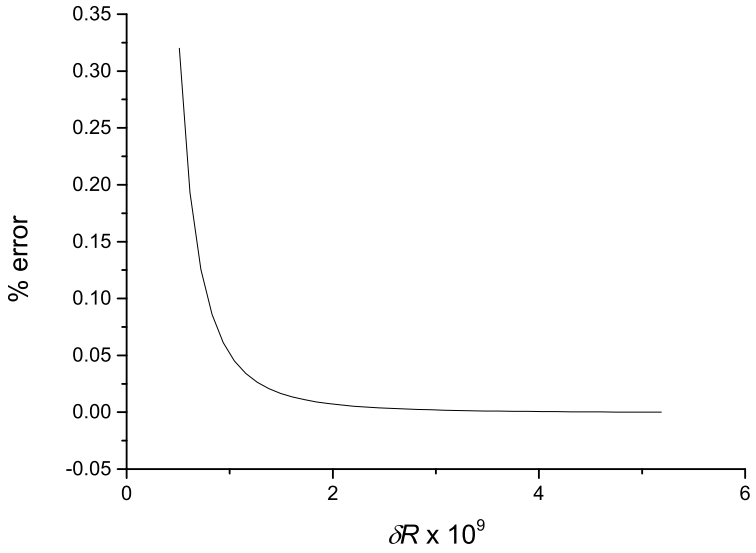


Figure 3.6: Percentage error in simulated steady state dimensionless flux as a function of δR, the point close to the electrode at which flux is measured. Percentages taken relative to largest δR value shown on this graph.

Simulated steady state ($\tau = 10^6$) concentration profiles of APC experiments are shown in Figure 3.7 for various nanoparticle sizes. It is seen that for large nanoparticles, the depletion layer becomes much smaller, since the particles near the electrode diffuse much more slowly to replenish those lost via destructive oxidation. As the particles get smaller, the concentration profiles converge on one another as the hindered diffusion becomes less and less significant, until the limit of zero size is reached.

Figure 3.8 shows $\lim_{R\to 1}\left(R^2 D' \frac{\partial C}{\partial R}\right)$ taken at $R = 1+2\times 10^{-9}$ at steady state ($\tau = 10^6$), *i.e.* the steady state (dimensionless) flux at the electrode, J, for various nanoparticle sizes. It is seen that the dimensionless flux approaches the familiar limit of unity for small nanoparticles, but decreases and approaches zero as the nanoparticles get larger, due to the hindered diffusion becoming more significant and limiting the rate at which the particles can approach the electrode.

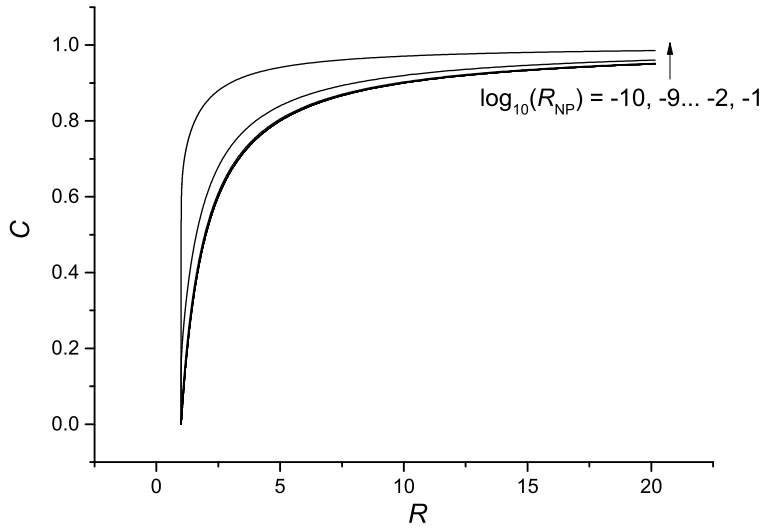


Figure 3.7: Steady state concentration profiles for nanoparticles of various sizes.

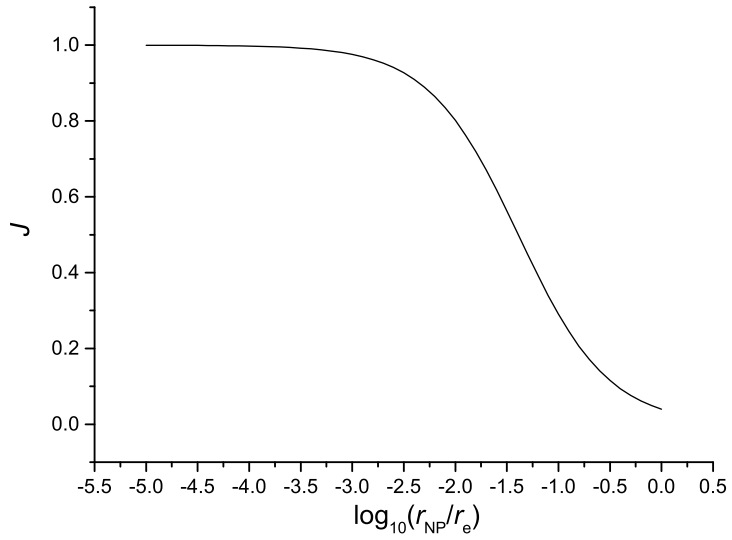


Figure 3.8: Steady state flux for nanoparticles of various sizes

Figure 3.9 shows simulated dimensionless fluxes ($J = \lim_{R\to 1}\left(R^2 D' \frac{\partial C}{\partial R}\right)$) generated as a function of dimensionless time after the potential step is applied in a APC experiments

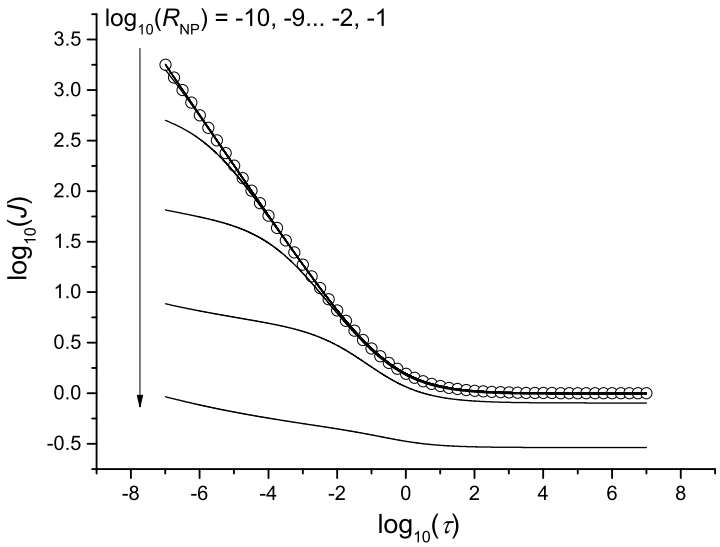


Figure 3.9: Transients produced for nanoparticles of various sizes (solid lines). Circles represent the transient derived from the analytical expression for flux at hemisphere as a function of dimensionless time τ after the potential step.

for nanoparticles of various sizes, as well as the analytical result from the equation:

$$J = 1 + \frac{1}{\sqrt{\tau\pi}} \tag{3.25}$$

It can be seen that small nanoparticles adhere exactly to the analytical expression, since the hindered diffusion occurs over a very small distance. As the particles get larger, deviations become apparent at short times. If the particles are not too large, these deviations vanish at longer times and the analytical result is obtained at steady state. For very large particles however, the steady state flux is reduced from that of the analytical expression, due to the greatly hindered diffusion of the particles.

3.4 Experimental

The experimental results presented in this chapter were obtained by Dr. Yige Zhou.

3.4.1 Chemicals

Nickel nanoparticles of radii range 15-30 nm and modal radius 26 nm were purchased from Nanostructured & Amorphous Materials, Inc. (Houston, Texas, USA). Nanoparticle sizes were confirmed *via* SEM imaging and impact analysis [12]. Sodium perchlorate ($\geq 98\%$, $NaClO_4$, Sigma Aldrich) and perchloric acid (70%, $HClO_4$, Fisher Chemicals) were used as received. All solutions were made using ultrapure water of resistivity not less than 18.2 $M\Omega\ cm^{-1}$ at 298 K (Millipore).

3.4.2 Instrumental

Electrochemical experiments were conducted within a faraday cage using a μAutolab III (Metrohm-Autolab BV, Utrecht, Netherlands) and a three electrode arrangement. The working electrode was a 6.9 μm radius carbon fibre micro electrode. A saturated calomel electrode and a graphite rod were used as the reference and counter electrodes respectively. Experiments were carried out in an aqueous solution of 10 mM $HClO_4$ and 100 mM $NaClO_4$. Nickel nanoparticles were handled under argon to prevent atmospheric oxidation. All experiments were also conducted under an argon atmosphere. Solutions were deoxygenated by bubbling nitrogen for at least 15 minutes.

3.5 Experimental results

Experimental results presented in this section were obtained by Dr. Yige Zhou, as noted above.

Since the theory we have developed is in hemispherical space, and the experiments are carried out on a planar microdisc electrode, we approximate one of these cases to the other. These two cases produces the same steady state current when:

$$r_{\text{disc}} = \frac{\pi r_{\text{hemi}}}{2} \tag{3.26}$$

where r_{disc} is the radius of the disc under study, and r_{hemi} is the radius of a hemisphere that will mimic the disc's steady state behaviour.

While this approximation is valid at long times, it breaks down at short times, where electrodes of equal area will produce equivalent currents (due to the linear diffusion domain). To assess the extent of this error and the influence it will have on our results, we can use the approximate Shoup-Szabo equation for a microdisc [27] (accurate to within 0.6%):

$$I = 4nFDC^{*}r_{\text{e}}f(\tau) \tag{3.27}$$

$$f(\tau) = 0.7854 + 0.4432\tau^{-0.5} + 0.2146\exp\left(-0.3912\tau^{-0.5}\right) \tag{3.28}$$

$$\tau = \frac{D}{r_{\text{e}}^{2}}t \tag{3.29}$$

and the analytical expression for the current at a hemisphere [28]:

$$I = 2\pi nr_{\text{e}}FDC^{*}\left(\frac{r_{\text{e}}}{\sqrt{\pi Dt}} + 1\right) \tag{3.30}$$

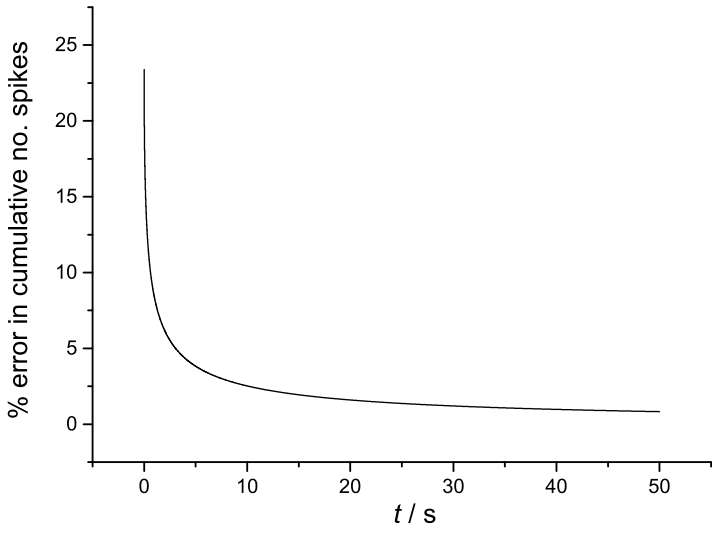


Figure 3.10: Error in the cumulative number of spikes observed as a function of time using the microdisc/microhemisphere approximation.

Both of these equations are valid in the absence of hindered diffusion, and the assumption is made that the disc/hemisphere relationship can be approximately extended to a hindered diffusion model.

The currents given by these equations can be converted to cumulative numbers of spikes by calculating the number of particles oxidised each second at time t (particles per second $= N_A I/F$) and numerically integrating with respect to time, as described above.

Carrying out this procedure using the parameters appropriate for this investigation, a plot of the percentage error in the cumulative number of spikes (when the steady state equivalence relation is used) as a function of time can be generated. This is shown in Figure 3.10. The parameters used were selected to correspond to the experiments discussed below: $r_{\mathrm{NP}} = 26$ nm, $D = 9.43 \times 10^{-12}$ m^2 s^{-1} (calculated using the Stokes-Einstein equation for the nanoparticles used in the experiments below), $c = 54$ pM, $r_{\mathrm{disc}} = 6.9$ μm and corresponding $r_{\mathrm{hemi}} = 4.39$ μm. It is seen that as the time tends to

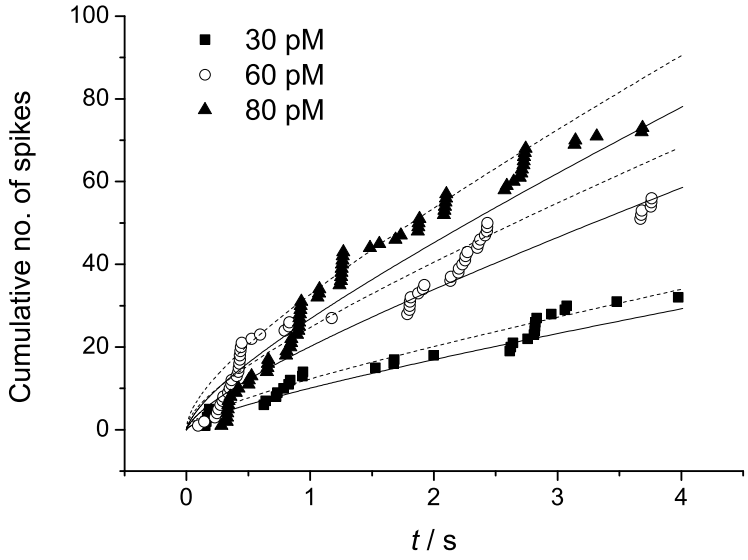


Figure 3.11: Experimental and theoretical cumulative number of spikes observed in APC experiments of NiNPs. Solid lines represent simulations including hindered diffusion, dashed lines simulations neglecting hindered diffusion.

large values, the error tends to zero as the disc/hemisphere equivalence approximation becomes exact. The experiments last for four seconds, which corresponds to an error of approximately 4.3%, which is much less than the uncertainty in the known concentrations of nanoparticles used in the experiments, as discussed below.

We next compare the theory developed to experimental results. Figure 3.11 shows the cumulative number of oxidative spikes observed for three separate anodic particle coulometry (APC) experiments with known concentrations of nickel nanoparticles (NiNPs) (28±4, 54±8 and 77±11 pM) of average radius 26 nm [12]. Also shown are theoretical results obtained using the model outlined above (solid lines), and theoretical results using the model neglecting hindered diffusion (dashed lines). The microdisc electrode used in the experiment ($r = 6.9$ μm) was approximated to a hemisphere ($r = 4.4$ μm). The diffusion

coefficient of the nanoparticles was calculated using the Stokes-Einstein equation [29]:

$$D = \frac{k_{\mathrm{B}}T}{6\pi\eta r_{\mathrm{NP}}} \tag{3.31}$$

where k_{B} is the Boltzmann constant and η is the viscosity of the solution (the viscosity of water at 298 K is 8.90×10^{-4} Pa s [30]).

It is seen that the model incorporating hindered diffusion shows a reduced number of cumulative impacts, as expected. The stochastic nature of the impacts make it difficult to fit a single theoretical line through the data, and both models are seen to qualitatively fit. In addition to this, there are significant sources of error in both models. Both assume a single radius of nanoparticle in solution of 26 nm, whereas in fact there is a distribution of nanoparticle radii, from less than 10 nm to greater than 60 nm (obtained via analysis of the areas of impact spikes and from scanning electron microscopy data [12]). There is also uncertainty in the known concentrations of the nanoparticles [12], as noted above. Further, the possible presence of a surface oxide layer on the nanoparticles may complicate the electron transfer process. These factors mean that the physical reality of the processes occurring is much more complex than is here modelled, either with hindered diffusion or without.

However, the qualitative fitting of the hindered diffusion model with the data suggests this model may represent a more complete understanding of complex nanoparticle impact processes.

3.6 Conclusions

In this chapter, we have used a model including the effects of near wall hindered diffusion to successfully simulate the anodic particle coulometry of nickel nanoparticles over a range of concentrations. We have investigated theoretically the effect of particle size on the electrochemistry of nanoparticles, and have found that where nanoparticles are very small (relative to the electrode size) a limit of molecular behaviour is reached. For large nanoparticles however, deviations become apparent, necessitating the use of this more complete model.

The following chapter applies the concept of hindered diffusion to model nanoparticle adsorption processes on microelectrodes, and investigates the effects of adsorption more generally.

References

[1] Barnes, E.; Zhou, Y.-G.; Rees, R. V.; Compton, R. G. *J. Electroanal. Chem.* **2012**, *691*, 28 – 34.

[2] Guo, D. D.; Wu, C. H.; Li, X. M.; Jiang, H.; Wang, X. H.; Chen, B. A. *J. Nanosci. and Nanotechnol.* **2008**, *8*, 2301 – 2307.

[3] Ahamed, M. *Toxicol. in vitro* **2011**, *25*, 930–936.

[4] Pasricha, A.; Jangra, S. L.; Singh, N.; Dilbaghi, N.; Sood, K.; Arora, K.; Pasricha, R. *J. Environ. Sci.* **2012**, *24*, 852 – 859.

[5] Gajewicz, A.; Rasulev, B.; Dinadayalane, T. C.; Urbaszek, P.; Puzyn, T.; Leszczynska, D.; Leszczynski, J. *Adv. Drug Deliv. Rev.* **2012**, *64*, 1663–1693.

[6] Heyrovský, M.; Jirovský, J. *Langmuir* **1995**, *11*, 4288 – 4292.

[7] Heyrovský, M.; Jirovský, J. *Langmuir* **1995**, *11*, 4293 – 4299.

[8] Heyrovský, M.; Jirovský, J. *Langmuir* **1995**, *11*, 4300 – 4308.

[9] Heyrovský, M.; Jirovský, J. *Langmuir* **1995**, *11*, 4309 – 4312.

[10] Zhou, Y.-G.; Rees, N. V.; Pillay, J.; Tshikhudo, R.; Vilakazi, S.; Compton, R. G. *Chem. Commun.* **2012**, *48*, 224 – 226.

[11] Zhou, Y.-G.; Rees, N. V.; Compton, R. G. *Angew. Chem. Int. Ed.* **2011**, *50*, 4219 – 4221.

[12] Stuart, E. J. E.; Zhou, Y.-G.; Rees, N. V.; Compton, R. G. *RSC Adv.* **2012**, *2*, 6879 – 6884.

[13] Haddou, B.; Rees, N. V.; Compton, R. G. *Phys. C* **2012**, *14*, 13612 – 13617.

[14] Bevan, M. A.; Prieve, D. C. *J. Chem. Phys.* **2000**, *113*, 1228 – 1236.

[15] Goldman, A.; Cox, R.; Brenner, H. *Chem. Eng. Sci.* **1967**, *22*, 637 – 651.

[16] Brenner, H. *Chem. Eng. Sci.* **1961**, *16*, 242 – 251.

[17] Banerjee, A.; Kihm, K. D. *Phys. Rev. E.* **2005**, *72*, 042101.

[18] Kazoe, Y.; Yoda, M. *Appl. Phys. Lett.* **2011**, *99*, 124104.

[19] Sharma, P.; Ghosh, S.; Bhattacharya, S. *Appl. Phys. Lett.* **2010**, *97*, 104101.

[20] Cutress, I. J.; Dickinson, E. J. F.; Compton, R. G. *J. Electroanal. Chem.* **2011**, *655*, 1 – 8.

[21] Einstein, A. *Ann. Phys.* **1905**, *17*, 549 – 560.

[22] Edwards, P. P.; Gray, H. B.; Lodge, M. T. J.; Williams, R. J. P. *Angew. Chem. Int. Ed.* **2008**, *47*, 6758–6765.

[23] Gavaghan, D. J. *J. Electroanal. Chem.* **1998**, *456*, 1 – 12.

[24] Gavaghan, D. J. *J. Electroanal. Chem.* **1998**, *456*, 13 – 23.

[25] Gavaghan, D. J. *J. Electroanal. Chem.* **1998**, *456*, 25 – 35.

[26] Press, W. H., Teukolsky, S. A., Vetterling, W. T., Flannery, B. P., Eds. *Numerical Recipes: The Art of Scientific Computing*; Cambridge University Press, 2007.

[27] Shoup, D.; Szabo, A. *J. Electroanal. Chem.* **1982**, *140*, 237 – 245.

[28] Bard, A. J.; Faulkner, L. R. *Electrochemical Methods, Fundamentals and Applications*, 2nd ed.; John Wiley & Sons Inc.: Hoboken, NJ, 2001.

[29] Dill, K. A.; Bromberg, S. *Molecular Driving Forces*; Garland Science, 2001.

[30] West, R. C., Ed. *Handbook of Chemistry and Physics*, 55th ed.; CRC Press, Inc.: Cleveland, Ohio, United States, 1974.

Chapter 4

The Rate of Adsorption of Nanoparticles on Microelectrode Surfaces

The previous chapter investigated the effect of near wall hindered diffusion on the destructive oxidation of nanoparticles at an electrode surface. This chapter develops theory for the rate of irreversible adsorption of nanoparticles from solution onto an electrode surface, including the effects of hindered diffusion of large nanoparticles. The effect of nanoparticle size on adsorption processes is studied, and found to be significant for large particles, where the nanoparticle radius to electrode radius ratio is larger than 1×10^{-3}. The extent of adsorption in a typical electrochemical nanoparticle experiment at a 5 μm radius hemispherical electrode is studied for different adsorption rate constants, along with the effect this has on concentration of nanoparticles in the vicinity of the electrode and the frequency of impacts of nanoparticles on the electrode. For fast adsorption rate constants, it is found that significant and long lasting (in extreme cases greater than 4 hours) concentration gradients can form, necessitating careful experimental practice. This work has been published in *The Journal of Electroanalytical Chemistry* [1].

4.1 Introduction

The previous chapter discussed the use of anodic particle coulometry to characterise nanoparticle solutions. The impacts observed during an experiment of this type are destructive in nature, and the nanoparticles are completely oxidised upon impact with the electrode. This gives information about the size [2], concentration [3], aggregation properties [4, 5] and electrochemical kinetics [6] of nanoparticles.

Often, however, nanoparticles will adsorb on an electrode surface [7], leading to a change in the character of the electrode surface assuming the chemical composition of the nanoparticles is different from that of the electrode. In this situation the character of the electrode changes from that of one material to another. It is of interest to explore the timescales over which this occurs.

In this chapter, we develop a model for the irreversible adsorption of nanoparticles onto a hemispherical electrode. Such a situation has previously been studied for the adsorption of molecules [8]. We extend the model to incorporate the hindered diffusion of spherical nanoparticles as they approach a wall in solution. As discussed in Chapter 3, hindered diffusion has both theoretically [9–11] and experimentally [12–14] shown to occur, and was successfully used in the previous chapter to model the quantitative oxidation of nickel nanoparticles [15]. By using typical experimental parameters for the size of nanoparticles and electrode radius, we can estimate the time taken for significant levels of adsorption to occur at various adsorption rate constants. If the rate constant for adsorption in unknown, this model can be used to obtain a timescale for a significant concentration of adsorbed particles to build up in the fast kinetic limit, providing a lower bound for this time. The extent of depletion of nanoparticles in the vicinity of the electrode surface is

also examined, along with its implications.

4.2 Theory

To simulate the adsorption of nanoparticles of arbitrary size onto the surface of a hemispherical electrode, a model largely identical to that used in Chapter 3 is used, the only change being the boundary condition at the electrode surface.

At this boundary ($r = r_\mathrm{e}$), both the surface coverage and the flux of material to the electrode must be considered. If the adsorption is irreversible, the concentration of particles adsorbed on the electrode surface, Γ (in mol m^{-2}), will vary with time in a manner dependent on the amount of material already adsorbed, the concentration of free species adjacent to the electrode surface, and a rate constant for adsorption, k (m s^{-1}):

$$\frac{\partial \Gamma}{\partial t} = k \left(1 - \frac{\Gamma}{\Gamma_\mathrm{m}}\right) c_{r=r_\mathrm{e}} \tag{4.1}$$

where Γ_m is the coverage (mol m^{-2}) of a complete monolayer.

The flux of material at the electrode surface per unit area (caused by the adsorption of nanoparticles and their subsequent removal from solution) will be equal to the rate at which they are adsorbed per unit area. Therefore:

$$D(r) \left(\frac{\partial c}{\partial r}\right)_{r=r_\mathrm{e}} = k \left(1 - \frac{\Gamma}{\Gamma_\mathrm{m}}\right) c_{r=r_\mathrm{e}} \tag{4.2}$$

However, from Equation 3.3 we know that the diffusion coefficient at the electrode surface is zero, meaning zero flux at the electrode surface, and therefore no adsorption (as seen in the previous chapter). However, the flux approaches a limiting value near the electrode

surface before very quickly dropping to zero at the electrode surface. It is this limiting value that we measure:

$$j = \lim_{r \to r_e} \left(r^2 D(r) \frac{\partial c}{\partial r} \right) \tag{4.3}$$

So rather than this boundary condition defining the flux actually at the surface, we use it to define the flux at some very small distance δr from the surface, and assume the flux at the surface is the same as this value, as outlined in Chapter 3. The value of the surface concentration can then be extrapolated assuming a linear concentration profile near the surface.

Introducing dimensionless parameters (defined in the Glossary), Equations 4.1 and 4.2 become:

$$\frac{\partial \rho}{\partial \tau} = k' \xi (1 - \rho) C_{R=1} \tag{4.4}$$

and:

$$D'(R) \left(\frac{\partial C}{\partial R} \right)_{R=1+\delta r} = k'(1 - \rho) C_{R=1} \tag{4.5}$$

The parameter ξ is a "saturation parameter," and is a measure of the bulk solution concentration relative to the adsorbed surface concentration of a complete monolayer:

$$\xi = \frac{c^* r_e}{\Gamma_m} \tag{4.6}$$

The surface boundary condition is now non-linear, and the set of simultaneous equations must be solved using the iterative Newton-Raphson method as outlined in Chapter 2.

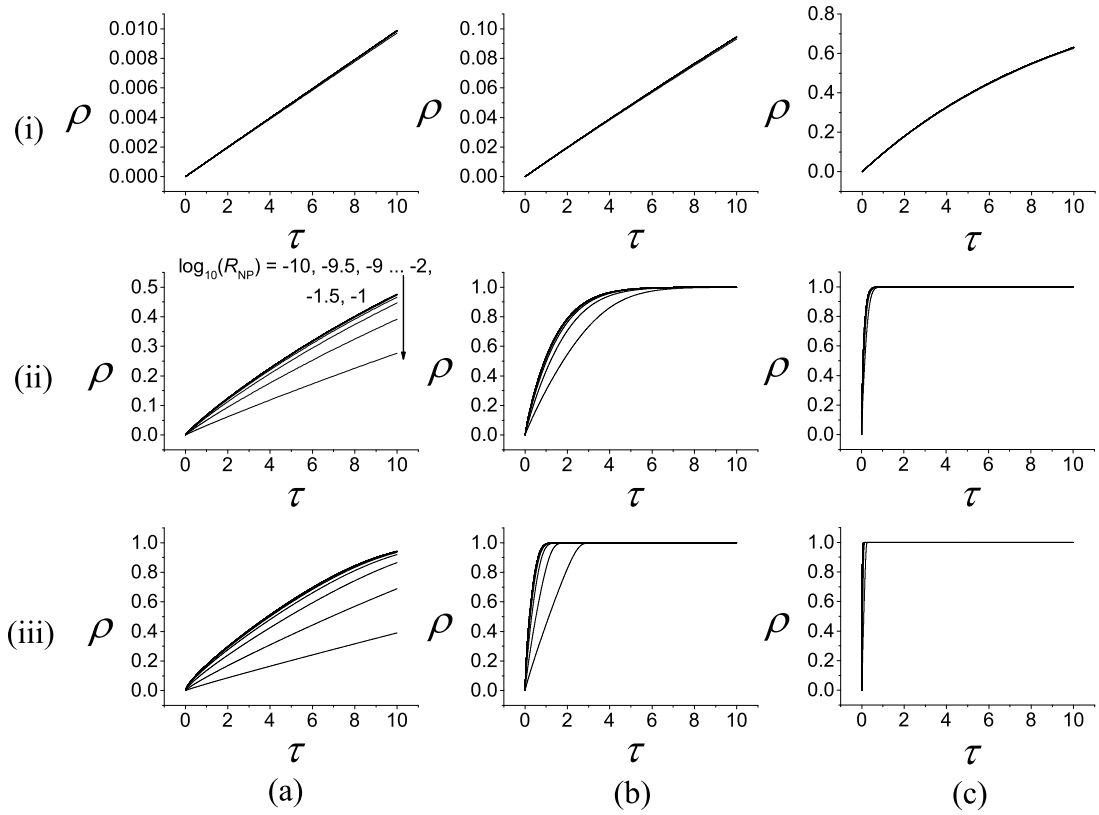


Figure 4.1: Variation of surface coverage, ρ with dimensionless time, τ for saturation parameter, ξ, values of (a) 0.1 (b) 1 and (c) 10, and dimensionless adsorption rate constant, k', of (i) 0.01 (ii) 1 and (iii) 10. Different lines within each graph represent different dimensionless nanoparticle radii from 10^{-10} to 10^{-1}, as illustrated in (a)(ii).

4.3 Simulated results and discussion

Simulations were carried out to determine the extent of adsorption, as a function of dimensionless time, for various dimensionless values of adsorption rate constant, k', saturation parameter, ξ, and nanoparticle radius, R_{NP}. The fractional surface coverage, ρ, is simulated as a function of time for various values of these three parameters, assuming that no adsorption occurs before $\tau = 0$. Typical results are shown in Figure 4.1. For small nanoparticles, where the diffusion is unhindered except in a region extremely close to the electrode surface, results from a previous study of adsorption onto spherical particles [8] (paralleling the adsorption onto a hemispherical electrode in this study) are reproduced.

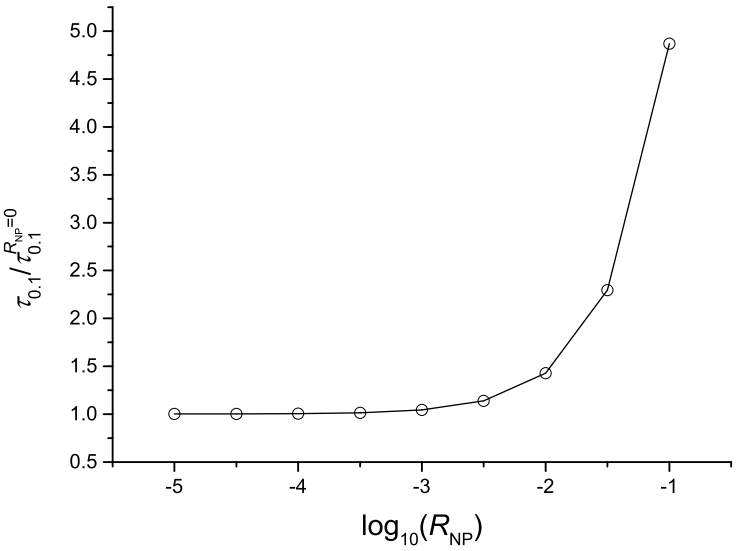


Figure 4.2: Ratio of time taken to form 10% of a monolayer for nanoparticles of various size to the time taken as the nanoparticle size approaches zero.

Trivially, adsorption is seen to occur more quickly at higher adsorption rate constants (Figure 4.1 row (i) shows small rate constants, (iii) shows high rate constants), for a given saturation parameter ξ. A larger saturation parameter (physically representing a smaller monolayer surface concentration compared with bulk solution concentration, Figure 4.1 (c)) also results in a full monolayer forming more quickly. Conversely, a smaller value of ξ (Figure 4.1 (a)) results in a longer time for a monolayer to form, due to smaller bulk solution concentration relative to the full monolayer surface concentration.

The effect of increasing the nanoparticle size is to increase the time taken for full monolayer formation, for any given value of k' and ξ, as shown in Figure 4.1 (a)(ii). Larger nanoparticles will experience more hindered diffusion at a greater distance from the electrode, hence reducing the flux of nanoparticles towards the electrode surface, limiting the rate at which adsorption can occur. This effect was found to be significant for particles of dimensionless radius greater than 10^{-3}.

Figure 4.2 shows the time taken to form 10% of a full monolayer for various nanoparticle sizes, $\tau_{0.1}$, relative to the time taken to form 10% of a monolayer when the size of the nanoparticle approaches zero and the effect of hindered diffusion is lost, $\tau_{0.1}^{R_{\mathrm{NP}}=0}$, for $k = 10$ and $\xi = 1$. For $R_{\mathrm{NP}} = 10^{-3}$, $\tau_{0.1}$ is 4.6% larger than $\tau_{0.1}^{R_{\mathrm{NP}}=0}$. It should be noted that since nanoparticles of differing sizes will have different bulk diffusion coefficients, these dimensionless times will map onto real times in different ways. This is not however related to hindered diffusion, but a consequence of the Stokes-Einstein equation (see below).

Hindered diffusion is also only shown to be significant for fast nanoparticle adsorption (Figure 4.1 (ii) and (iii)). If adsorption is slow (Figure 4.1 (i)) then the mass transport of nanoparticles to the surface is fast compared with the rate of their loss at the surface. This means that slowing down the mass transport has little effect, since the process is essentially completely activation controlled. At larger rate constants however, the process gains a degree of mass transport control and hindered diffusion of larger nanoparticles begins to have much more of an effect.

In order to determine the minimum time for significant adsorption to occur, typical experimental parameters [3] (nanoparticle size, $r_{\mathrm{NP}} = 13$ nm, electrode radius $r_{\mathrm{e}} = 5$ μm and bulk concentration, $c^* = 50$ pM) were used to simulate the surface coverage as a function of time for a variety of adsorption rate constants, from the fast adsorption limit down to slower rate constants. To calculate the saturation parameter, ξ, a knowledge of the surface concentration of a full monolayer, Γ_{m}, is required. This value will depend on the geometry of adsorption, which in turn depends on the nature of the surface being adsorbed on. For the purposes of this study, we assume that a monolayer consists of hexagonally close packed nanoparticles covering the entirety of the surface. A schematic of the unit cell is shown in Figure 4.3. The area of the unit cell, which contains a total of

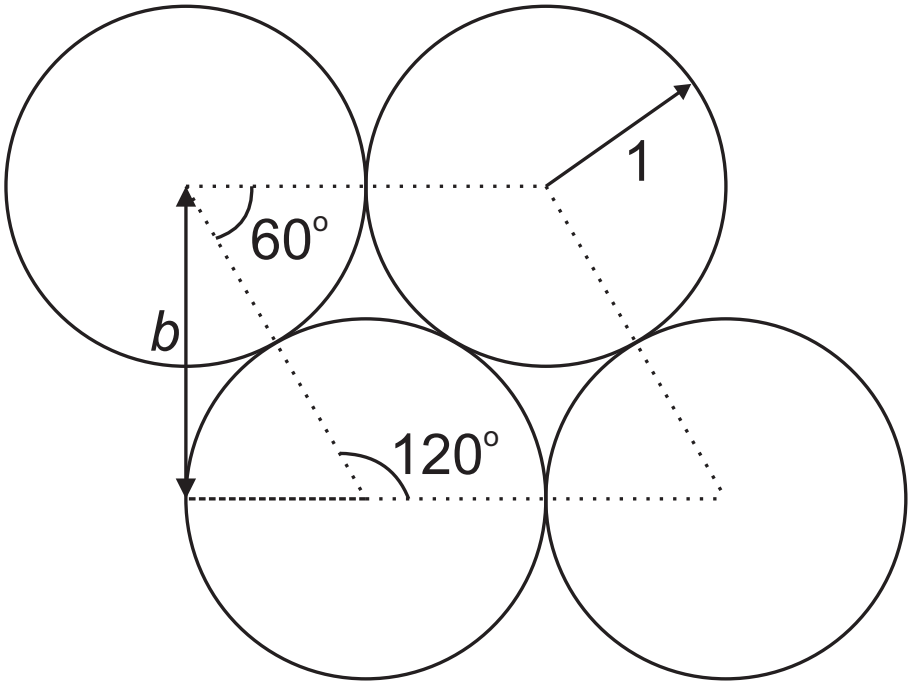


Figure 4.3: Schematic diagram of close packed adsorbed nanoparticles. Dotted lines represent the unit cell.

one adsorbed nanoparticle, is equal to $2b$. From trigonometry:

$$b = 2\cos(30^\circ) \tag{4.7}$$

$$= \sqrt{3} \tag{4.8}$$

The unit cell area is therefore equal to $2\sqrt{3}$. The area of the single nanoparticle contained within the unit cell is π. The packing efficiency, ζ, is therefore:

$$\zeta = \frac{\pi}{2\sqrt{3}} \times 100\% \tag{4.9}$$

$$\approx 90.69\% \tag{4.10}$$

Simple calculations of the cross sectional area of a nanoparticle leads to the number and therefore number of moles of nanoparticles per square metre, leading to $\Gamma_{\mathrm{m}} = 2.84 \times$

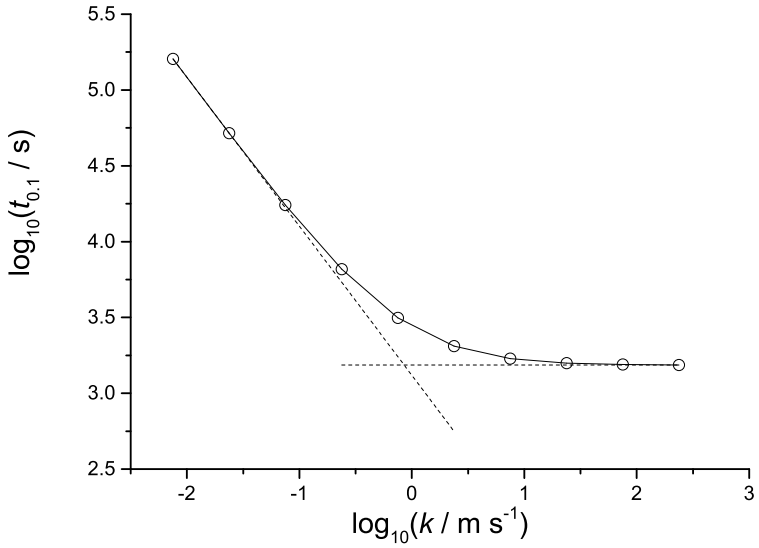


Figure 4.4: Decadic log of time take for 10% of a monolayer to build up, $t_{0.1}$ as a function of the decadic log of the adsorption rate constant, k. Limiting behavior for slow and fast adsorption shown by dotted lines.

10^{-9} mol m^{-2}, and therefore $\xi = 8.82 \times 10^{-5}$. The bulk diffusion coefficient of the nanoparticles is estimated using the Stokes-Einstein equation, given by [16]:

$$D^{\text{bulk}} = \frac{kT}{6\pi\eta r_{\text{NP}}} \tag{4.11}$$

where k is the Boltzmann constant, T is temperature and η is the viscosity of the solvent (in this case water, at 298 K $\eta = 8.90 \times 10^{-4}$ Pa s [17]) giving a bulk diffusion coefficient of $D^{\text{bulk}} = 1.89 \times 10^{-11}$ m^2 s^{-1}.

Simulations were carried out using these parameters and various dimensionless adsorption rate constants from $k' = 10^{-2}$ to $k' = 10^{2.5}$ to determine the time taken for the surface coverage, ρ, to reach 0.1, $t_{0.1}$. The results are shown (in dimensional parameters) in Figure 4.4. The data recorded show a typical transition from activation control at slow rate constants to diffusion control at high rate constants, where increasing the rate

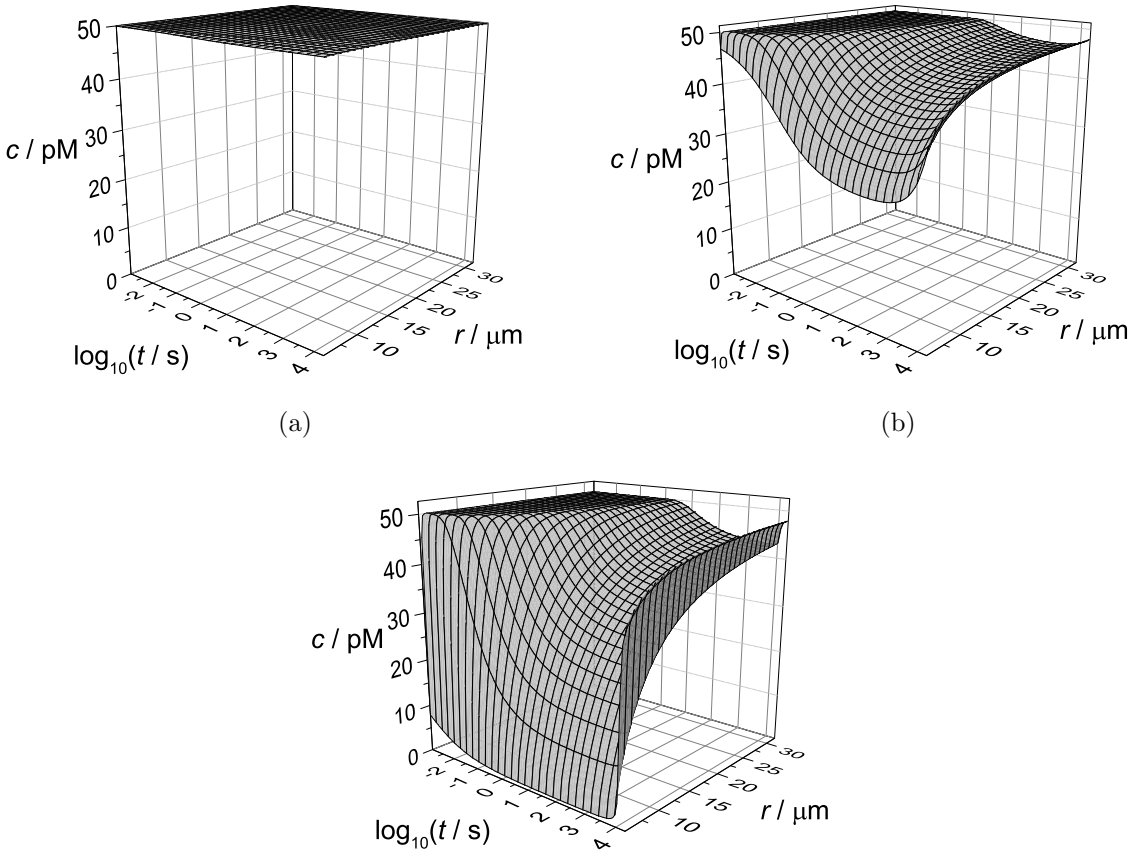


Figure 4.5: Concentration of nanoparticles in solution as a function of radial coordinate and decadic log of time, for parameters described in the text and various adsorption rate constants. Dimensionless rate constants are: (a) 0.01; (b) 1; (c) 100. These correspond to dimensional values of 3.8×10^{-6}, 3.8×10^{-4} and 3.8×10^{-2} m s^{-1} respectively.

constant no longer has an effect on the rate of adsorption. In this fast adsorption limit, the time taken for 10% of a monolayer to build up is found to be approximately 20 - 30 minutes. This gives us a lower bound on the time taken for surface adsorption to reach significant levels (where a significant level is taken to be 10% coverage) for the parameters discussed above.

We next question what the concentration profiles will look like if adsorption is allowed to take place. Figure 4.5 shows concentration profiles of nanoparticles as a function of distance and time, for the same experimental parameters as Figure 4.4. It is seen that, for

low rate constants (Figure 4.5(a)), the concentration profile remains essentially unchanged over these timescales. The particles are adsorbed so slowly that any lost from the surface are efficiently replenished from bulk solution. At higher rate constants, however, it is seen that significant concentration gradients become present in solution well before the time at which 10% of a monolayer is formed, in hundredths of a second for dimensionless rate constant $k^{'} = 100$, as can be seen in Figure 4.5(c). The fast adsorption rate constant means material adjacent to the electrode is consumed very quickly, resulting in a marked concentration gradient formed fast. It then takes in excess of 4 hours to recover even half of the original surface concentration.

These concentration gradients could have a dramatic impact on nanoparticle experiments, for example anodic particle coulometry (APC), as desribed in the previous chapter. If adsorption has been allowed to occur before the potential step, the depletion of nanoparticles around the electrode will have an impact on the frequency of nanoparticle-electrode impacts. It is therefore desirable to have a knowledge of how the frequency of impacts varies with time due to adsorption.

The frequency (s^{-1}) of successful impacts, those that result in a nanoparticle sticking, is given by the flux of nanoparticles at the electrode surface. This is equal to 4.2 multiplied by the electrode area and the Avogadro constant N_A:

$$\nu_{\text{successful}} = k(1-\rho)c^0 A N_A \tag{4.12}$$

where c^0 is the concentration of nanoparticles adjacent to the electrode surface and A is the electrode area (m^2). This is expected to approach zero at larger times and the surface becomes filled up. Similarly, the frequency (s^{-1}) of collisions that are unsuccessful

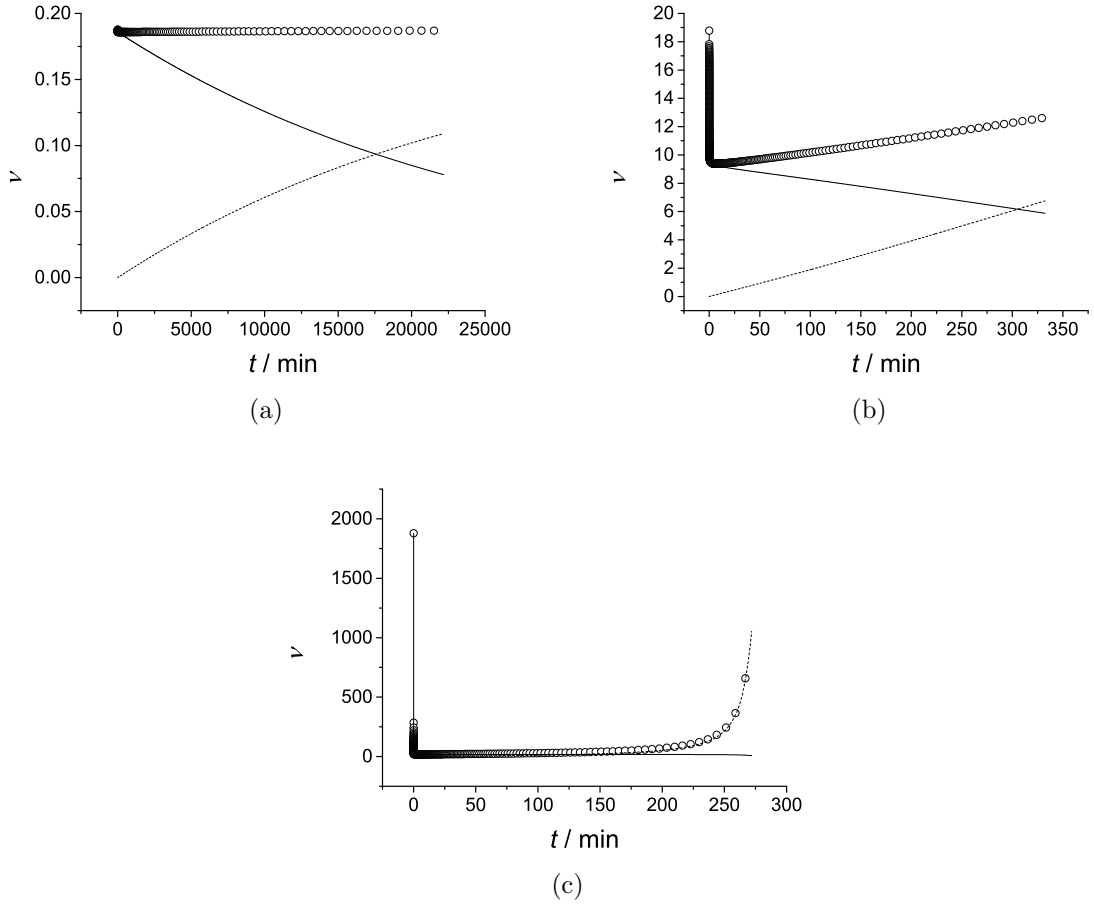


Figure 4.6: Frequency (s^{-1}) of nanoparticle impacts for dimensionless rate constants of (a) 0.01, (b) 1 and (c) 100, corresponding to dimensional values of 3.8×10^{-6}, 3.8×10^{-4} and 3.8×10^{-2} m s^{-1} respectively. Other parameters as described in text. Solid lines correspond to successful impacts that stick, dashed lines to unsuccessful ones that do not stick through collision with an occupied site, and open circles to total number of impacts.

through colliding with a blocked part of the electrode is given by:

$$\nu_{\text{unsuccessful}} = k\rho c^0 A N_A \tag{4.13}$$

The total number of collisions (with potential to stick, whether successful or not), ν_{total}, is the sum of these two frequencies (and hence equal to kc^0AN_A). This impact frequency of particles with sufficient energy to stick will be, for a given adsorption rate constant and temperature, equal to some constant fraction of the total number of impacts of any

energy. These impact frequencies, as a function of time, are shown in Figure 4.6 for three different rate constants (dimensionless values of 0.01, 1 and 100, corresponding to dimensional values of 3.8×10^{-6}, 3.8×10^{-4} and 3.8×10^{-2} m s^{-1} respectively). It is seen that for the slow adsorption rate constant (Figure 4.6 (a)) the total impact frequency of particles with sufficient energy to stick is close to constant over the whole, very wide, time range. For the faster rate constants, the total frequency of impacts initially drops off, before slowly building up again as the electrode surface becomes filled up and material in the solution near the electrode is replenished. It should also be noted that the total frequency is higher for larger rate constants, since a greater proportion of nanoparticles will have sufficient energy to stick.

Figure 4.7 shows the fraction of impacts which are successful, as a function of time, for the same three adsorption rate constants. As expected, it is seen that for slow rate

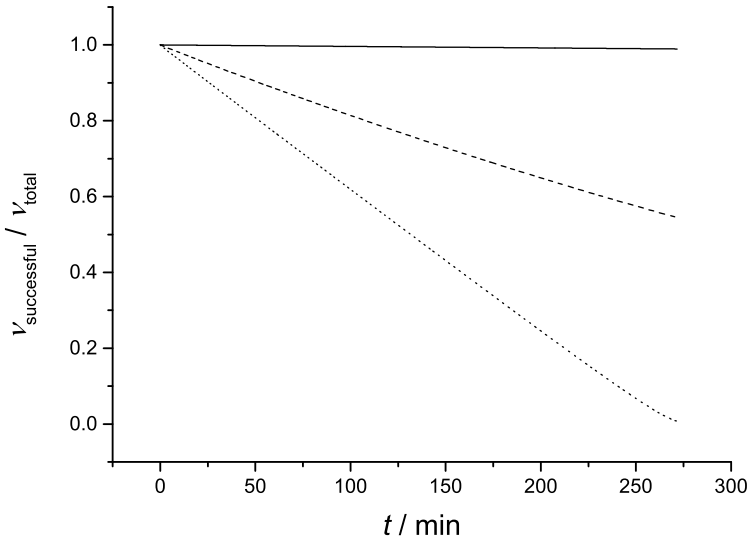


Figure 4.7: Fraction of impacts which adsorb as a function of time for three adsorption rate constants. Dimensionless rate constants are: Solid line - $k' = 0.01$, dashed line - $k' = 1$, dotted line - $k' = 100$. These correspond to real values of 3.8×10^{-6}, 3.8×10^{-4} and 3.8×10^{-2} m s^{-1} respectively.

constants (solid line) this fraction decreases very slowly with time (since the number of available sites decreases slowly). For intermediate (dashed line) and fast (dotted line) rate constants, the surface fills up more quickly so the fraction of impacts which are successful decreases more quickly.

This alone means that, if adsorption of nanoparticles occurs quickly, significant concentration gradients may form in solution before an experiment of interest can start, which have a large effect on the frequency of particle-electrode impacts. It is seen in Figure 4.6 (c) that even after four hours the total impact frequency is only about half of the initial value. Depending on the experiment to be performed, this may however not be a problem. If an APC experiment (or indeed any experiment with nanoparticles) is to be carried out on nanoparticles which adsorb strongly to the surface, the time taken for a full monolayer to form and for concentration gradients to dissipate may be greatly reduced by stirring the nanoparticle solution, increasing the rate of mass transport. After a full monolayer has formed and the solution again has a uniform concentration, applying the potential step will immediately oxidise and destroy the adsorbed monolayer, and the experiment can proceed as normal with a clean surface and uniform concentration profile the instant after the potential step. Also of significance here is the time taken for the surface to change from being mostly "electrode" to mostly "nanoparticle" in character as a result of adsorption.

4.4 Conclusions

It has been shown by simulation that the size of nanoparticles has an effect on the time taken to adsorb on a surface, such as an electrode, and form a monolayer, due to the

more hindered diffusion of larger particles in solution. Using typical parameters for an electrochemical nanoparticle experiment ($c^* = 50$ pM, $r_e = 5$ μm, $a = 13$ nm), it was shown that even in the limit of very fast adsorption, it takes *ca.* half an hour for 10% of a monolayer to build up on the electrode surface. This does, however, cause significant depletion of material around the electrode which can take several hours to replenish under diffusion only conditions, and has a large effect on the number of nanoparticle-electrode impacts. This suggests that if adsorption of nanoparticles does occur, careful steps may have to be taken to ensure uniformity of concentration throughout solution, even if not much of a monolayer has formed on the electrode surface. Moreover the formation of even 10% of a monolayer can significantly modify electrode behaviour from that characteristic of the bare electrode to that of the nanoparticle material [18, 19].

The following chapters focus on electroanalysis at microband electrodes, with three distinct cases discussed. They are first considered in isolation, before moving on to dual bands working in generator-collector mode, and finally large arrays of bands, also in generator-collector mode.

References

[1] Barnes, E. O.; Compton, R. G. *J. Electroanal. Chem.* **2013**, *693*, 73 – 78.

[2] Stuart, E. J.; Rees, N. V.; Compton, R. G. *Chem. Phys. Lett.* **2012**, *531*, 94 – 97.

[3] Stuart, E. J. E.; Zhou, Y.-G.; Rees, N. V.; Compton, R. G. *RSC Adv.* **2012**, *2*, 6879–6884.

[4] Zhou, Y.-G.; Rees, N. V.; Pillay, J.; Tshikhudo, R.; Vilakazi, S.; Compton, R. G. *Chem. Commun.* **2012**, *48*, 224–226.

[5] Zhou, Y.-G.; Rees, N. V.; Compton, R. G. *Angew. Chem. Int. Ed.* **2011**, *50*, 4219–4221.

[6] Haddou, B.; Rees, N. V.; Compton, R. G. *Phys. C* **2012**, *14*, 13612–13617.

[7] Zhou, Y.-G.; Rees, N. V.; Compton, R. G. *Chem. Phys. Lett.* **2011**, *514*, 291 – 293.

[8] Chevallier, F. G.; Šljukić, B.; Wildgoose, G. G.; Jiang, L.; Jones, T. G. J.; Compton, R. G. *ChemPhysChem* **2006**, *7*, 697–703.

[9] Brenner, H. *Chem. Eng. Sci.* **1961**, *16*, 242 – 251.

[10] Bevan, M. A.; Prieve, D. C. *J. Chem. Phys.* **2000**, *113*, 1228–1236.

[11] Goldman, A.; Cox, R.; Brenner, H. *Chem. Eng. Sci.* **1967**, *22*, 637 – 651.

[12] Kazoe, Y.; Yoda, M. *Appl. Phys. Lett.* **2011**, *99*, 124104.

[13] Banerjee, A.; Kihm, K. D. *Phys. Rev. E.* **2005**, *72*, 042101.

[14] Sharma, P.; Ghosh, S.; Bhattacharya, S. *Appl. Phys. Lett.* **2010**, *97*, 104101.

[15] Barnes, E.; Zhou, Y.-G.; Rees, R. V.; Compton, R. G. *J. Electroanal. Chem.* **2013**, *691*, 28 – 34.

[16] Dill, K. A.; Bromberg, S. *Molecular Driving Forces*; Garland Science, 2001.

[17] West, R. C., Ed. *Handbook of Chemistry and Physics*, 55th ed.; CRC Press, Inc.: Cleveland, Ohio, United States, 1974.

[18] Simm, A. O.; Banks, C. E.; Ward-Jones, S.; Davies, T. J.; Lawrence, N. S.; Jones, T. G.; Jiang, L.; Compton, R. G. *Analyst* **2005**, *130*, 1303–1311.

[19] Davies, T. J.; Moore, R. R.; Banks, C. E.; Compton, R. G. *J. Electroanal. Chem.* **2004**, *574*, 123 – 152.

Chapter 5

Double Potential Step Chronoamperometry at a Microband Electrode: Theory and Experiment

In this chapter, numerical simulation is used to characterise double potential step chronoamperometry at a microband electrode for a simple redox process, A + e^- $\rightleftharpoons$ B. The method is shown to be highly sensitive for the measurement of the diffusion coefficients of both A and B, and is applied to the one electron oxidation of decamethylferrocene (DMFc), DMFc − e^- $\rightleftharpoons$ $DMFc^+$, in the room temperature ionic liquid 1-propyl-3-methylimidazolium bistrifluoromethylsulfonylimide [Pmim][$N(Tf)_2$]. Theory and experiment are seen to be in excellent agreement and the following values of the diffusion coefficients were measured at 298 K: $D_{\mathrm{DMFc}} = 2.50 \times 10^{-7}$ cm^2 s^{-1} and $D_{\mathrm{DMFc^+}} = 9.50 \times 10^{-8}$ cm^2 s^{-1}. This work has been published in *The Journal of Electroanalytical Chemistry* [1]. Experiments were carried out by Ms. Linhongjia Xiong.

5.1 Introduction

The field of electrochemistry has been transformed by the introduction of microelectrodes [2], which have the properties of enhanced mass transport allowing steady states to be achieved [3], operate with reduced Ohmic drop [4] and often allow a two electrode setup

to be employed with a combined reference/counter electrode [5]. The most widely used microelectrode is the microdisc, which is easily fabricated and has well characterised properties [6, 7].

The application of microdisc electrodes are many and varied, including using single potential step chronoamperometry to determine the diffusion coefficient of a species of interest, D_{A}, and simultaneously either its concentration, c_{A}, or the number of electrons transfered, n, provided one of these two parameters is known [8]. In a single step chronoamperometry experiment, the potential applied to the working electrode is stepped from a value where no reaction occurs, to one where reduction (or oxidation) occurs at a mass transport controlled rate, as outlined in Chapter 1. The well established Shoup-Szabo equation then describes the current measured within 0.6 % error [9]:

$$i = 4nFc_{\mathrm{A}}D_{\mathrm{A}}r_e f(\tau) \tag{5.1}$$

where

$$f(\tau) = 0.7854 + 0.4432\tau^{-0.5} + 0.2146\exp\left(-0.3912\tau^{-0.5}\right) \tag{5.2}$$

and

$$\tau = \frac{D_{\mathrm{A}}t}{r_e^2} \tag{5.3}$$

where i is the measured current (A), F is the Faraday constant and r_e is the radius of the microelectrode (m). The change in the current's dependency on D_{A} (from $\sqrt{D_{\mathrm{A}}}$ at short times to linearly dependent at long times), and the direct proportionality of the current to nc_{A} at all times, allows both D_{A} and the product nc_{A} to be determined by fitting of the Shoup-Szabo equation to experimental data. A knowledge of either n or c_{A} then allows

calculation of the final unknown.

Using double potential step chronoamperometry, in conjunction with numerical simulation, this method can be extended to find not only D_{A}, but also D_{B}, the diffusion coefficient of the other member of the redox couple [10]. In these experiments, the potential is first stepped in the same manner as for single potential step experiments, and held at this reducing potential for a set time, t_s, before being stepped a second time to a value where the reverse reaction occurs at a mass transport controlled rate, and species B is converted back to species A. Numerical simulations of double potential step experiments can then be used, with D_{A}, c_{A} and D_{B} as input parameters, and these parameters optimised to obtain a best fit.

In addition to these simple yet powerful techniques, microelectrodes of various geometries have found uses in a wide variety of applications, including weakly supported voltammetry [11] (where their very low Ohmic drop is of great advantage in the study of the effects of migration), generator/collector systems [12], electrochemical sensors [13–15], and studies of ionic liquid properties [16, 17].

Despite these extensive uses of microelectrodes, investigations of double potential step chronoamperometry have largely confined themselves to microdiscs, except for one case each at spherical [18] and hemispherical [19] electrodes. This chapter extends the theory of double potential step chronoamperometry to microband electrodes. Note these electrodes are being manufactured by Nanoflux PTE LTD®[20] and MicruX®[21], have been noted for their ease of construction, cheapness and durability [22], and are finding increasing use in electrochemical sensors.

In addition to these advantages, microband electrodes have emerged as being experimentally useful, and have found steadily increasing use in hydrodynamic voltammetry in

a flow cell [23–30], in dual electrode generator-collector mode [31–36], and in impedance spectroscopy [37, 38]. One of the key differences in electrochemistry carried out at microbands, as opposed to microdiscs, is the absence of a true steady state in chornoamperometry at microbands [39]. This has the effect that, at all times, the measured current is dependent on both D and $\sqrt{D}$. This lack of a true steady state will make behavior observed in double potential step chronoamperometry at microbands different to that at microdiscs, and perhaps more useful.

The study of ionic liquids has received a huge amount of attention in recent years (see [40] and [41] for reviews). Being composed entirely of mobile ions, their intrinsic conductivity removes the need to add any supporting electrolyte to carry out electrochemical experiments. They also have a near zero volatility, and often have a very wide electrochemical window. This has led to their application in electrochemical gas sensors [42], as well as sensors for temperature [42] and humidity [43]. A further property of ionic liquids is that they can show drastic differences between the diffusion coefficients of members of a redox pair, *e.g.* the factor of 30 difference between the diffusion coefficients of O_2 and $O_2^{\bullet -}$ in the ionic liquid hexyltriethylammonium bis-((trifluoromethyl)sulfonyl)imide ($[N_{6222}][N(Tf)_2]$) [44]. This is due to the extremely strong ionic interactions hindering the movement of charged species. This large difference between diffusion coefficients in ionic liquids necessitates accurately measuring both of them if their electrochemistry is to be fully understood, and so performing double potential step chronoamperomtry in the solvents is a necessity.

In this chapter, a model is developed to numerically simulate double potential step chronoamperometry at a microband electrode, and used to asses the extent to which this technique can be used to determine both D_A and D_B at a microband electrode.

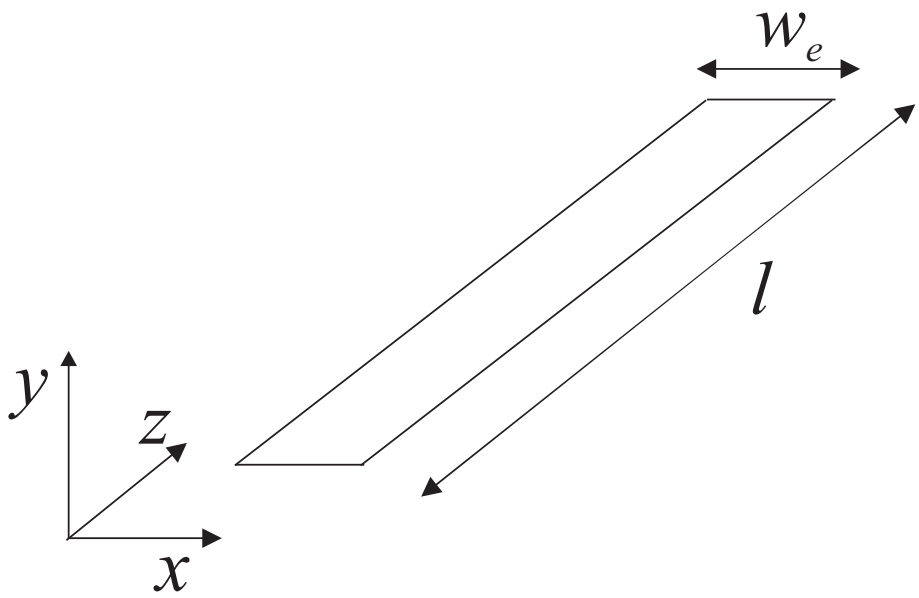


Figure 5.1: Schematic diagram of a microband electrode.

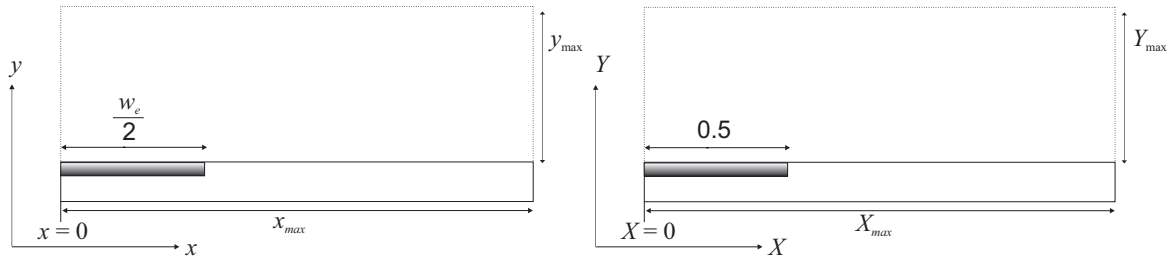
We validate this model by simulating the double potential step chronoamperometry of decamethylferrocene in the ionic liquid [Pmim][NTf_2] and fitting experimental data.

5.2 Theory

In this chapter, we develop a model to simulate double potential step chronoamperometry, as discussed in the above, at a planar microband electrode. A schematic of the electrode being used is shown in Figure 5.1, indicating the parameters w_e (the electrode width), l (the electrode length) and the orientation of the Cartesian coordinates. A simple one electron redox couple is considered:

$$\mathrm{A} \pm \mathrm{e}^- \rightleftharpoons \mathrm{B} \tag{5.4}$$

If the microband is considered to be infinitely long in the z direction (relative to its width in the x direction, see Figure 5.1), the edge effects at the ends of the electrode can



(a) Dimensional simulation space (b) Dimensionless simulation space

Figure 5.2: Schematic diagram of the simulation space used in this study in (a) real apsace and (b) dimensionless space.

be neglected, along with diffusion along the length of the electrode, reducing the mass transport equation to be solved to two dimensions. In dimensionless parameters (see Chapter 2 and the Glossary), the mass transport equation is given by:

$$\frac{\partial C_{\mathrm{i}}}{\partial \tau} = D_{\mathrm{i}}^{'} \left(\frac{\partial^2 C_{\mathrm{i}}}{\partial X^2} + \frac{\partial^2 C_{\mathrm{i}}}{\partial Y^2} \right) \tag{5.5}$$

Subject to appropriate boundary conditions described below, this equation is used to simulate the time evolution of the concentration of species in solution.

5.2.1 Boundary Conditions

The simulation space used is shown schematically in Figure 5.2. Due to symmetry around $X = 0$, we only need simulate half of the electrode and surrounding solution, with a zero flux condition imposed by symmetry at $X = 0$:

$$\left(\frac{\partial C_{\mathrm{i}}}{\partial X} \right)_{X=0} = 0 \tag{5.6}$$

A zero flux condition is imposed on the insulating surface around the electrode:

$$\left(\frac{\partial C_{\mathrm{i}}}{\partial Y}\right)_{X>0.5} = 0 \tag{5.7}$$

Before the experiment begins at $\tau = 0$, the potential is set such that no reaction occurs and no current is drawn:

$$\tau < 0;\ \text{all } X;\ \text{all } Y \begin{cases} C_{\mathrm{A}} = 1 \\ \\ C_{\mathrm{B}} = 0 \end{cases} \tag{5.8}$$

At times after $\tau = 0$, at the electrode surface ($X < 0.5$, $Y = 0$) the boundary conditions for each species depend on the applied potential. Before some switching time, τ_{s}, the potential applied to the electrode is such that species A is reduced at a mass transport controlled rate to form species B. Hence, when $\tau < \tau_{\mathrm{s}}$:

$$\tau < \tau_{\mathrm{s}};\ X < 0.5;\ Y = 0 \begin{cases} C_{\mathrm{A}} = 0 \\ \\ D'_{\mathrm{B}} \left(\frac{\partial C_{\mathrm{B}}}{\partial Y}\right) = -\left(\frac{\partial C_{\mathrm{A}}}{\partial Y}\right) \end{cases} \tag{5.9}$$

After τ_{s}, the potential is stepped to a more positive value such that now species B is oxidised at a mass transport controlled rate back to species A:

$$\tau \geq \tau_{\mathrm{s}};\ X < 0.5;\ Y = 0 \begin{cases} C_{\mathrm{B}} = 0 \\ \\ \left(\frac{\partial C_{\mathrm{A}}}{\partial Y}\right) = -D'_{\mathrm{B}} \left(\frac{\partial C_{\mathrm{B}}}{\partial Y}\right) \end{cases} \tag{5.10}$$

The bulk solution boundaries were set at $6\sqrt{D'_{\max}\tau_{\max}}$ from the electrode in both

<table>
<tr><th colspan="3">Boundary</th><th>Condition</th></tr>
<tr><td>$\tau < 0$</td><td>All X</td><td>All Y</td><td>$C_{\mathrm{A}} = 1$, $C_{\mathrm{B}} = 0$</td></tr>
<tr><td>$0 \leq \tau < \tau_s$</td><td>$0 \leq X \leq 0.5$</td><td rowspan="4">$Y = 0$</td><td>$C_{\mathrm{A}} = 0$, $D'_{\mathrm{B}} \left(\frac{\partial C_{\mathrm{B}}}{\partial Y}\right) = -\left(\frac{\partial C_{\mathrm{A}}}{\partial Y}\right)$</td></tr>
<tr><td>$\tau \geq \tau_s$</td><td>$0 \leq X \leq 0.5$</td><td>$\left(\frac{\partial C_{\mathrm{A}}}{\partial Y}\right) = -D'_{\mathrm{B}} \left(\frac{\partial C_{\mathrm{B}}}{\partial Y}\right)$, $C_{\mathrm{B}} = 0$</td></tr>
<tr><td rowspan="4">All τ</td><td>$X > 0.5$</td><td>$\frac{\partial C_{\mathrm{i}}}{\partial Y} = 0$</td></tr>
<tr><td>$X = 0$</td><td rowspan="2">All Y</td><td>$\frac{\partial C_{\mathrm{i}}}{\partial X} = 0$</td></tr>
<tr><td>$X = X_{\max}$</td><td rowspan="2">$C_{\mathrm{A}} = 1$, $C_{\mathrm{B}} = 0$</td></tr>
<tr><td>All X</td><td>$Y = Y_{\max}$</td></tr>
</table>

Table 5.1: Dimensionless boundary conditions for double potential step chronoamperometry simulations at a microband electrode.

the X and Y direction, where $D'_{\max}$ and $\tau_{\max}$ are the maximum dimensionless diffusion coefficient in the system and the total dimensionless time of the experiment respectively [45–47]. At these boundaries, bulk concentrations are assumed:

$$X = 0.5 + 6\sqrt{D'_{\max}\tau_{\max}};\; Y = 6\sqrt{D'_{\max}\tau_{\max}} \begin{cases} C_{\mathrm{A}} = 1 \\ \\ C_{\mathrm{B}} = 0 \end{cases} \tag{5.11}$$

These boundary conditions are summarised in Table 5.1.

To calculate the current, the flux must be evaluated at each point on the electrode, and summed up over the entire electrode surface. The total dimensionless flux, J, is given

by:

$$J = 2\int_{X=0.5}^{X=0}\left(\frac{\partial C_{\mathrm{A}}}{\partial Y}\right)_{Y=0}\mathrm{d}X \tag{5.12}$$

and the dimensional current given by:

$$I = -FAj \tag{5.13}$$

where F is the Faraday constant, A is the electrode area in m^2, and j is the dimensional flux, given by:

$$j = \frac{c_{\mathrm{A}}^{*} D_{\mathrm{A}}}{w_e} J \tag{5.14}$$

giving:

$$I = -c_{\mathrm{A}}^{*} D_{\mathrm{A}} l F J \tag{5.15}$$

assuming an initial reduction. If instead, species A is oxidised, the current is trivially multiplied by minus one.

5.2.2 Numerical Methods

The methods outlined in Chapter 2 are used to discretise the mass transport equations and boundary conditions, and solved over discrete spatial and temporal grids using the alternating direction implicit (ADI) method in conjunction with the Thomas algorithm for an n-diagonal matrix [48] (see Chapter 2). The form of the temporal grid employed is one which has been successfully used in previous models [49–51]. After a potential step,

the temporal grid is initially uniform, but after some defined change time τ_c it expands:

$$\tau \leq \tau_c \qquad \tau_{k+1} = \tau_k + \Delta_\tau \tau \tag{5.16}$$

$$\tau_c < \tau < \tau_s \qquad \tau_{k+1} = \tau_k + \gamma_\tau \left(\tau_k - \tau_{k-1}\right) \tag{5.17}$$

After the potential switch, the temporal grid repeats its form but offset by an amount τ_s. It should be noted that since microband electrodes exhibit pseudo steady state behaviour [39], a denser temporal grid is required than for microdisc simulations where a steady state concentration profile allows for large time steps at high τ.

The spatial grid used is shown schematically in Figure 5.3 (some lines removed for clarity). After an initial step of Δ_s, the grid expands from $X = 0$ and from the electrode edge ($X = 0.5$) in both direction in a way directly analogous to the temporal grid, with an expansion coefficient of γ_s. Convergence studies found grid parameter values of: $\Delta_\tau = 1 \times 10^{-7}$, $\tau_c = 1 \times 10^{-4}$, $\gamma_\tau = 1.0001$, $\Delta_s = 1 \times 10^{-5}$ and $\gamma_s = 1.1$ were sufficient to give results such that making either grid ten times denser changed the simulation result by less than 0.5%. The simulations were coded in C++ with multithreaded parallel

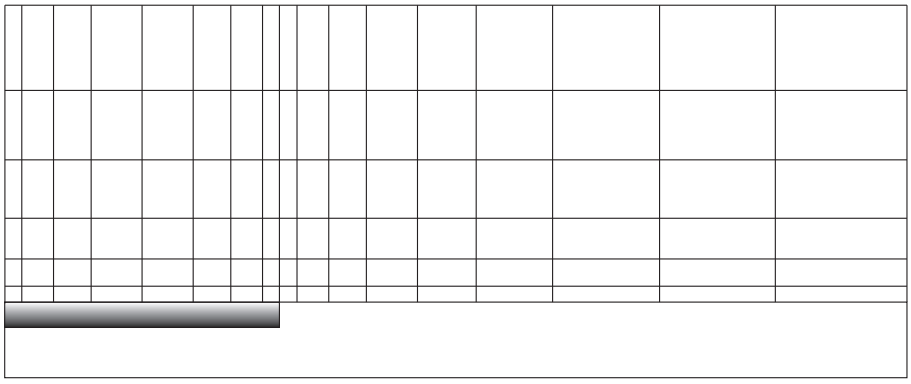


Figure 5.3: Schematic diagram of the spatial grid employed (some lines removed for clarity).

programming employed to increase efficiency, and run on an Intel(R) Xeon(R) 2.26 GHz PC with 2.25 GB RAM.

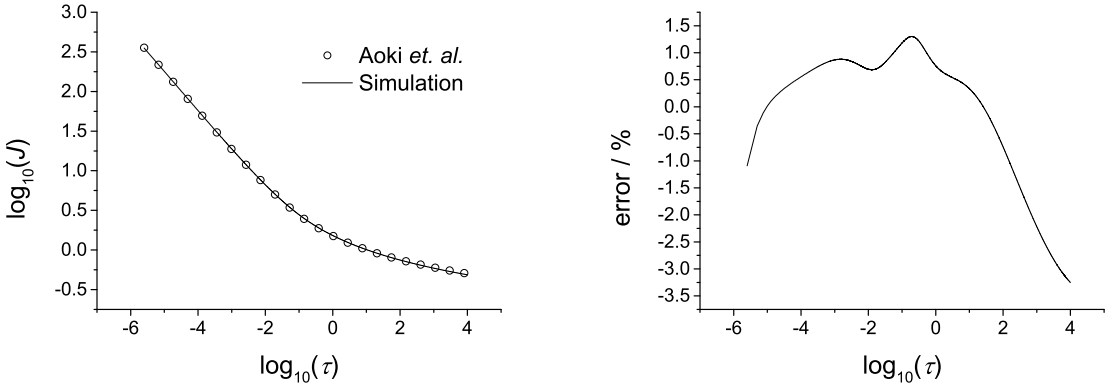
5.3 Theoretical Results

In order to validate the program used in this study, the simulated dimensionless flux for the first step of a double potential step chronoamperometry experiment can be compared to the equation developed by Aoki *et. al.* [39]:

$$J = \frac{1}{\sqrt{\pi\tau}} + 0.97 - 1.10\exp\left(\frac{-9.90}{|\ln(12.37\tau)|}\right) \tag{5.18}$$

The comparison between simulations from this model and from the analytical equation proposed by Aoki *et. al.* is shown in Figure 5.4. Excellent agreement is seen between the two.

As discussed in the introduction, double potential step chronoamperometry can be



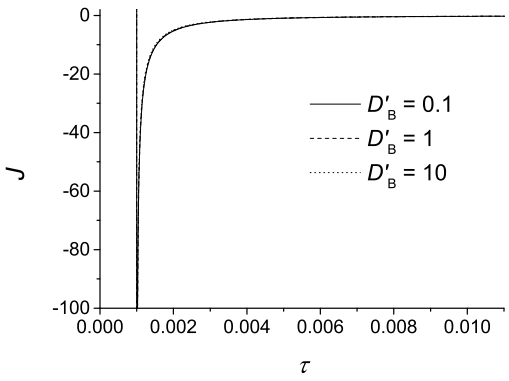
(a) (b)

Figure 5.4: (a) Dimensionless flux during the first step of a double potential step chronoamperometry experiment at a band electrode calculated via simulation (line) and Aoki's equation (circles). (b) Percentage error between the simulation used in this study and Aoki's equation.

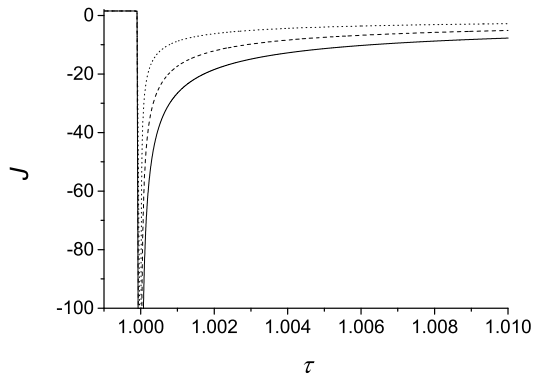
used to obtain values for the diffusion coefficients of both the oxidised and reduced form of the species under investigation. The model described above can be used to probe the extent to which microband electrodes are useful in this respect, and under what conditions values can be most easily obtained.

Simulations of double potential step chronoamperometry were carried out with various values of τ_s, the time at which the potential is switched, and $D_{\mathrm{B}}^{'}$. The results, zoomed in on the parts of the chronoamperograms of interest, are shown in Figure 5.5. τ_s values of 0.001, 1 and 1000 were used, as well as $D_{\mathrm{B}}^{'}$ values of 0.1, 1 and 10. By comparing the results from different diffusion coefficients at various switching times, it can be seen whether switching the potential after a short time or a long time will give the greatest discrepancies between different diffusion coefficients, and hence allow the most accurate determinations of D_{B}. In Figure 5.5, it is immediately apparent that a large value of τ_s is desirable for discriminating between different values of $D_{\mathrm{B}}^{'}$. For small values of τ_s, species B does not have time to diffuse away from the electrode to any significant extent, and the currents drawn after τ_s are essentially identical for all three values of $D_{\mathrm{B}}^{'}$. For larger values of τ_s, however, species B does diffuse away from the electrode to different extents for different $D_{\mathrm{B}}^{'}$, therefore giving very different responses after the second potential step.

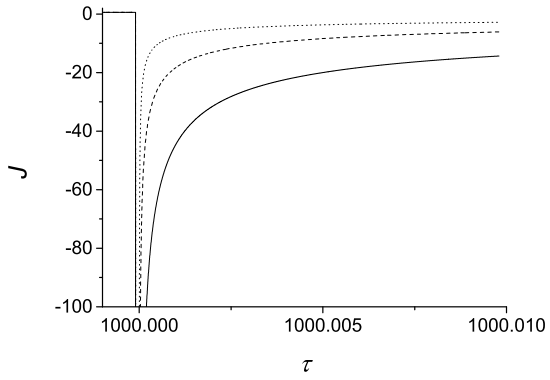
Tables 5.2 to 5.5 tabulate reference values for the dimensionless flux, J, measured after the second potential step, for τ_s values of 1, 10, 100 and 1000, each with a wide range of $D_{\mathrm{B}}^{'}$ values. The (dimensional) value of D_{A} can be extracted by fitting experimental data to the first transient, then D_{B} estimated by comparing the second step transient with these reference tables. The pseudo-steady state nature of the diffusion to a microband allows higher resolution between different $D_{\mathrm{B}}^{'}$ values to be achieved with higher τ_s values, approaching a limit as τ_s approaches ∞.



(a) $\tau_s = 0.001$



(b) $\tau_s = 1$



(c) $\tau_s = 1000$

Figure 5.5: Dimensionless flux at short times after the second potential step for D'_B values of 0.1, 1 and 10, and τ_s values of (a) 0.001, (b) 1 and (c) 1000

D'_{B}	$\tau - \tau_s$							
	0.01	0.1	0.5	1	2	5	10	25
0.01	-9.0187	-2.1405	-0.5610	-0.2727	-0.1209	-0.0368	-0.0143	-0.0040
0.05	-8.2419	-1.9694	-0.5205	-0.2538	-0.1128	-0.0347	-0.0137	-0.0040
0.1	-7.7371	-1.8567	-0.4925	-0.2407	-0.1078	-0.0339	-0.0137	-0.0041
0.2	-7.0770	-1.7090	-0.4580	-0.2265	-0.1034	-0.0336	-0.0139	-0.0043
0.3	-6.6213	-1.6083	-0.4369	-0.2186	-0.1012	-0.0335	-0.0140	-0.0044
0.4	-6.2752	-1.5329	-0.4221	-0.2133	-0.0998	-0.0334	-0.0141	-0.0045
0.5	-5.9985	-1.4736	-0.4110	-0.2094	-0.0987	-0.0334	-0.0142	-0.0045
0.6	-5.7694	-1.4251	-0.4022	-0.2062	-0.0978	-0.0333	-0.0143	-0.0046
0.7	-5.5750	-1.3846	-0.3949	-0.2036	-0.0971	-0.0333	-0.0143	-0.0046
0.8	-5.4068	-1.3499	-0.3888	-0.2013	-0.0964	-0.0332	-0.0143	-0.0046
0.9	-5.2592	-1.3198	-0.3834	-0.1994	-0.0959	-0.0332	-0.0143	-0.0046
1.0	-5.1281	-1.2933	-0.3787	-0.1977	-0.0953	-0.0331	-0.0143	-0.0047
2.0	-4.3037	-1.1327	-0.3497	-0.1865	-0.0918	-0.0326	-0.0143	-0.0047
3.0	-3.8656	-1.0510	-0.3341	-0.1801	-0.0895	-0.0322	-0.0143	-0.0048
4.0	-3.5791	-0.9983	-0.3235	-0.1757	-0.0879	-0.0319	-0.0142	-0.0048
5.0	-3.3718	-0.9603	-0.3155	-0.1723	-0.0866	-0.0316	-0.0141	-0.0048
6.0	-3.2121	-0.9310	-0.3092	-0.1696	-0.0856	-0.0314	-0.0141	-0.0048
7.0	-3.0841	-0.9073	-0.3040	-0.1673	-0.0847	-0.0312	-0.0140	-0.0048
8.0	-2.9784	-0.8876	-0.2996	-0.1653	-0.0839	-0.0310	-0.0140	-0.0048
9.0	-2.8889	-0.8708	-0.2958	-0.1636	-0.0833	-0.0308	-0.0139	-0.0048
10	-2.8120	-0.8562	-0.2924	-0.1621	-0.0827	-0.0307	-0.0139	-0.0048
20	-2.3729	-0.7696	-0.2715	-0.1524	-0.0787	-0.0297	-0.0136	-0.0047
50	-1.9420	-0.6757	-0.2471	-0.1408	-0.0737	-0.0283	-0.0131	-0.0046

Table 5.2: Simulated dimensionless fluxes at various times after the second potential step and various values of D'_{B} for $\tau_s = 1$

D'_{B}	$\tau - \tau_s$							
	0.01	0.1	0.5	1	2	5	10	25
0.01	-16.399	-4.7499	-1.7984	-1.1183	-0.6581	-0.2908	-0.1407	-0.0476
0.05	-12.792	-3.7306	-1.4298	-0.8972	-0.5353	-0.2443	-0.1230	-0.0445
0.1	-10.924	-3.2064	-1.2453	-0.7905	-0.4800	-0.2258	-0.1164	-0.0434
0.2	-9.1066	-2.7028	-1.0742	-0.6945	-0.4312	-0.2090	-0.1101	-0.0421
0.3	-8.1174	-2.4327	-0.9858	-0.6453	-0.4059	-0.1999	-0.1065	-0.0412
0.4	-7.4594	-2.2553	-0.9288	-0.6136	-0.3893	-0.1938	-0.1040	-0.0406
0.5	-6.9764	-2.1265	-0.8880	-0.5906	-0.3771	-0.1892	-0.1020	-0.0401
0.6	-6.6002	-2.0272	-0.8566	-0.5729	-0.3676	-0.1855	-0.1004	-0.0397
0.7	-6.2954	-1.9474	-0.8315	-0.5586	-0.3599	-0.1824	-0.0991	-0.0393
0.8	-6.0411	-1.8814	-0.8107	-0.5467	-0.3534	-0.1799	-0.0980	-0.0390
0.9	-5.8244	-1.8256	-0.7930	-0.5365	-0.3478	-0.1776	-0.0970	-0.0387
1.0	-5.6366	-1.7775	-0.7778	-0.5276	-0.3429	-0.1756	-0.0961	-0.0385
2.0	-4.5386	-1.5024	-0.6887	-0.4750	-0.3132	-0.1633	-0.0906	-0.0369
3.0	-4.0020	-1.3712	-0.6443	-0.4481	-0.2977	-0.1567	-0.0875	-0.0359
4.0	-3.6649	-1.2894	-0.6157	-0.4305	-0.2875	-0.1522	-0.0854	-0.0352
5.0	-3.4269	-1.2314	-0.5950	-0.4177	-0.2799	-0.1489	-0.0838	-0.0347
6.0	-3.2469	-1.1874	-0.5789	-0.4077	-0.2740	-0.1463	-0.0825	-0.0343
7.0	-3.1043	-1.1522	-0.5659	-0.3995	-0.2691	-0.1441	-0.0814	-0.0340
8.0	-2.9876	-1.1232	-0.5551	-0.3927	-0.2650	-0.1422	-0.0805	-0.0337
9.0	-2.8897	-1.0987	-0.5458	-0.3868	-0.2615	-0.1406	-0.0798	-0.0334
10	-2.8060	-1.0776	-0.5378	-0.3817	-0.2584	-0.1392	-0.0791	-0.0332
20	-2.3372	-0.9545	-0.4895	-0.3508	-0.2396	-0.1306	-0.0748	-0.0317
50	-1.8895	-0.8261	-0.4366	-0.3163	-0.2182	-0.1204	-0.0696	-0.0299

Table 5.3: Simulated dimensionless fluxes at various times after the second potential step and various values of D'_{B} for $\tau_s = 10$

D'_{B}	$\tau - \tau_s$							
	0.01	0.1	0.5	1	2	5	10	25
0.01	-25.4686	-7.8654	-3.3629	-2.2976	-1.5470	-0.8852	-0.5595	-0.2838
0.05	-16.1797	-5.0499	-2.2041	-1.5306	-1.0556	-0.6335	-0.4194	-0.2273
0.1	-12.959	-4.0865	-1.8180	-1.2808	-0.9002	-0.5555	-0.3750	-0.2080
0.2	-10.278	-3.2944	-1.5086	-1.0835	-0.7776	-0.4923	-0.3379	-0.1910
0.3	-8.9473	-2.9065	-1.3605	-0.9893	-0.7183	-0.4607	-0.3189	-0.1820
0.4	-8.1025	-2.6626	-1.2686	-0.9305	-0.6808	-0.4404	-0.3065	-0.1761
0.5	-7.5005	-2.4902	-1.2040	-0.8889	-0.6540	-0.4256	-0.2974	-0.1717
0.6	-7.0414	-2.3598	-1.1551	-0.8572	-0.6335	-0.4142	-0.2903	-0.1682
0.7	-6.6752	-2.2564	-1.1164	-0.8319	-0.6169	-0.4050	-0.2846	-0.1654
0.8	-6.3737	-2.1718	-1.0846	-0.8110	-0.6032	-0.3972	-0.2797	-0.1630
0.9	-6.1195	-2.1008	-1.0578	-0.7934	-0.5916	-0.3906	-0.2756	-0.1609
1.0	-5.9010	-2.0402	-1.0348	-0.7781	-0.5814	-0.3849	-0.2719	-0.1591
2.0	-4.6581	-1.6982	-0.9031	-0.6895	-0.5219	-0.3505	-0.2500	-0.1480
3.0	-4.0702	-1.5310	-0.8391	-0.6456	-0.4919	-0.3328	-0.2386	-0.1421
4.0	-3.7071	-1.4422	-0.7983	-0.6174	-0.4724	-0.3212	-0.2311	-0.1381
5.0	-3.4534	-1.3748	-0.7691	-0.5970	-0.4582	-0.3127	-0.2255	-0.1352
6.0	-3.2629	-1.3228	-0.7466	-0.5812	-0.4472	-0.3061	-0.2211	-0.1329
7.0	-3.1129	-1.2815	-0.7285	-0.5684	-0.4383	-0.3007	-0.2176	-0.1310
8.0	-2.9906	-1.2463	-0.7135	-0.5577	-0.4308	-0.2961	-0.2145	-0.1295
9.0	-2.8884	-1.2188	-0.7006	-0.5486	-0.4244	-0.2922	-0.2119	-0.1281
10	-2.8013	-1.1941	-0.6895	-0.5407	-0.4188	-0.2888	-0.2097	-0.1269
20	-2.3175	-1.0516	-0.6236	-0.4934	-0.3851	-0.2680	-0.1958	-0.1193
50	-1.8614	-0.9048	-0.5526	-0.4416	-0.3477	-0.2445	-0.1799	-0.1107

Table 5.4: Simulated dimensionless fluxes at various times after the second potential step and various values of D'_{B} for $\tau_s = 100$

D'_{B}	$\tau - \tau_s$							
	0.01	0.1	0.5	1	2	5	10	25
0.01	-32.071	-10.135	-4.5217	-3.1914	-2.2514	-1.4164	-0.9970	-0.6234
0.05	-18.293	-5.8761	-2.7000	-1.9473	-1.4153	-0.9390	-0.6925	-0.4597
0.1	-14.199	-4.6252	-2.1765	-1.5959	-1.1835	-0.8073	-0.6064	-0.4106
0.2	-10.984	-3.6523	-1.7770	-1.3301	-1.0077	-0.7047	-0.5375	-0.3700
0.3	-9.4456	-3.1919	-1.5911	-1.2062	-0.9246	-0.6548	-0.5033	-0.3494
0.4	-8.4879	-2.9075	-1.4771	-1.1297	-0.8726	-0.6231	-0.4813	-0.3360
0.5	-7.8142	-2.7087	-1.3976	-1.0760	-0.8357	-0.6003	-0.4654	-0.3263
0.6	-7.3053	-2.5594	-1.3378	-1.0353	-0.8076	-0.5828	-0.4531	-0.3187
0.7	-6.9023	-2.4418	-1.2906	-1.0030	-0.7851	-0.5687	-0.4432	-0.3125
0.8	-6.5725	-2.3459	-1.2520	-0.9764	-0.7665	-0.5569	-0.4349	-0.3073
0.9	-6.2958	-2.2658	-1.2195	-0.9539	-0.7508	-0.5469	-0.4278	-0.3029
1.0	-6.0590	-2.1975	-1.1918	-0.9346	-0.7371	-0.5383	-0.4216	-0.2990
2.0	-4.7294	-1.8182	-1.0337	-0.8232	-0.6576	-0.4869	-0.3848	-0.2756
3.0	-4.1110	-1.6432	-0.9576	-0.7685	-0.6179	-0.4608	-0.3659	-0.2635
4.0	-3.7323	-1.5358	-0.9094	-0.7336	-0.5923	-0.4438	-0.3535	-0.2554
5.0	-3.4693	-1.4605	-0.8750	-0.7084	-0.5738	-0.4315	-0.3444	-0.2495
6.0	-3.2725	-1.4037	-0.8486	-0.6890	-0.5594	-0.4218	-0.3372	-0.2449
7.0	-3.1180	-1.3587	-0.8273	-0.6733	-0.5478	-0.4139	-0.3315	-0.2411
8.0	-2.9924	-1.3217	-0.8097	-0.6602	-0.5380	-0.4074	-0.3266	-0.2379
9.0	-2.8877	-1.2905	-0.7947	-0.6491	-0.5297	-0.4017	-0.3224	-0.2351
10	-2.7986	-1.2637	-0.7817	-0.6394	-0.5225	-0.3968	-0.3188	-0.2327
20	-2.3058	-1.1096	-0.7051	-0.5818	-0.4791	-0.3670	-0.2965	-0.2179
50	-1.8447	-0.9519	-0.6230	-0.5192	-0.4312	-0.3336	-0.2713	-0.2009

Table 5.5: Simulated dimensionless fluxes at various times after the second potential step and various values of D'_{B} for $\tau_s = 1000$

5.4 Experimental

All experimental data in this chapter was obtained by Ms. Linhongjia Xiong.

5.4.1 Chemicals

Ferrocene ($Fe(C_5H_5)_2$, Aldrich, 98%), acetonitrile (MeCN, Fischer Scientific, dried and distilled, 99%), tetra-n-butylammonium perchlorate (TBAP, Fluka, Puriss electrochemical grade, 99%), decamethylferrocene ($Fe(C_{10}H_{15})_2$, Fluka, 95%) and 1-propyl-3-methylimidazolium bistrifluoromethylsulfonylimide ([Pmim][NTf_2], kindly donated by Queen's University, Belfast) were used as received without further purification.

5.4.2 Instrumental

All electrochemical experiments were carried out using a computer-controlled PGSTAT30-Autolab potentiostat (Eco-Chemie, Netherlands). Solutions were housed in a sealed glass vial, with a three-electrode arrangement consisting of either a 5.0 μm radius Pt disc or a Pt microband (see below) working electrode, a silver wire reference electrode and Pt coil wire counter electrode. The platinum microdisc working electrode was polished on soft lapping pads (Kemet Ltd., UK) using alumina powders (Buehler, IL) of sizes 1.0, 0.3 and 0.05 μm. The electrode radius was calibrated electrochemically by analysing the steady-state voltammetry of a 2.0 mM solution of ferrocene in MeCN containing 0.1 M TBAP, using a diffusion coefficient for ferrocene of 2.30×10^{-9} m^2 s^{-1} at 298 K [52]. The ionic liquid was degassed under vacuum overnight to remove water and other impurities. All experiments were performed inside a thermostated box (previously described by Evans *et. al.* [53]) which also functioned as a Faraday cage. The temperature was maintained

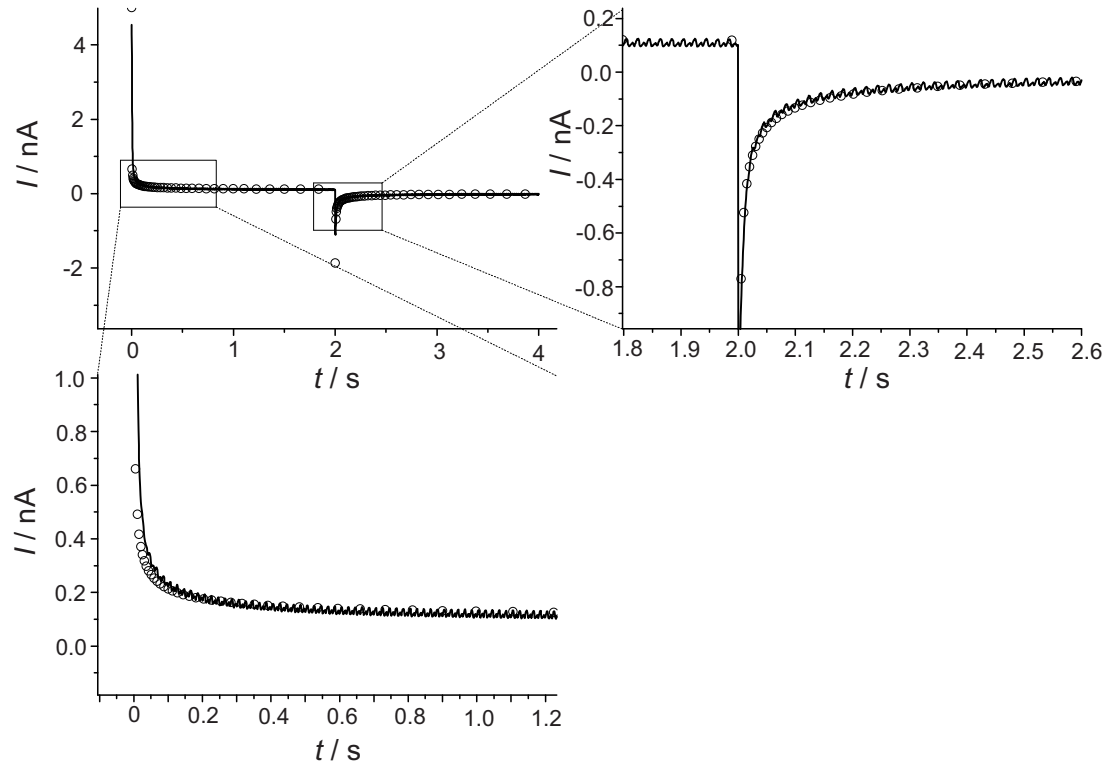


Figure 5.6: Experimental (solid lines) and simulated (circles) double potential step chronoamperograms of DMFc at a Pt microdisc electrode, with parts shown zoomed in for clarity.

at 298 (±0.5) K. A platinum microband electrode of dimensions 6.28 mm × 50 μm was fabricated using the method of Wadhawan *et. al.* [22].

5.5 Experimental Results

Experimental results presented in this section were obtained by Ms. Linhongjia Xiong, as noted above.

To validate the band electrode model outlined above, we can compare experimental and theoretical data at a band electrode to data collected at a microdisc electrode, simulated using the well established model developed by Klymenko *et. al.* [10].

Double potential step chronoamperometry was carried out on 2.0 mM decamethyl-

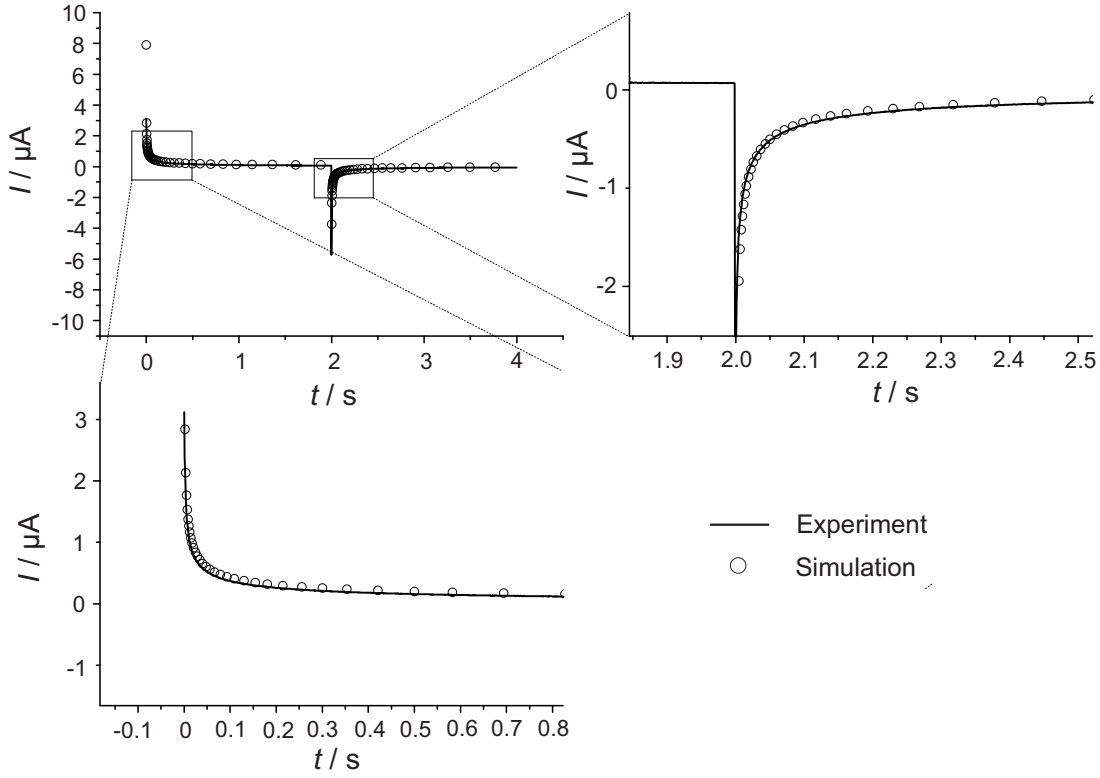


Figure 5.7: Experimental (solid lines) and simulated (circles) double potential step chronoamperograms of DMFc at a Pt microband electrode, with parts shown zoomed in for clarity.

ferrocene (DMFc) in the room temperature ionic liquid [Pmim][NTf_2] on both a planar microdisc electrode (r_{disc} = 5.0 μm) and the microband (width = 50 μm, length = 6.28 mm) electrode fabricated as described by Wadhawan *et. al.* [22]. In both cases, the potential was initially held at -0.25 V for 20 s, before being stepped to +0.2 V for 2 s then to -0.25 V for 2 s, all vs a silver wire reference electrode. The results for the disc electrode are shown in Figure 5.6. *Via* the simulations, diffusion coefficients for DMFc and $DMFc^+$ of 2.49($\pm$0.2) $\times$ 10^{-11} m^2 s^{-1} and 9.57($\pm$0.6) $\times$ 10^{-12} m^2 s^{-1} respectively were determined in [Pmim][NTf_2]. For comparison, a value for the diffusion coefficient of ferrocene in the similar ionic liquid 1-ethyl-3-methylimidazolium bistrifluoromethylsulfonylimide ([Emim][NTf_2]) has been found to be 4.7 $\times$ 10^{-7} m^2 s^{-1} [54]. The lower value for DMFc is consistent with this due to its bulkier size.

The same experiment was then carried out at a band electrode. The results are shown in Figure 5.7. Diffusion coefficients of DMFc and $DMFc^+$ were determined to be $2.50(\pm 0.2) \times 10^{-11}$ m^2 s^{-1} and $9.50(\pm 0.2) \times 10^{-12}$ m^2 s^{-1} respectively in [Pmim][NTf_2], in good agreement with those determined from the disc electrode data. This suggests that the program used to simulate the band electrode data is accurate.

5.6 Conclusions

A computational model for the simulation of double potential step chronoamperometry at a microband electrode has been developed, which is shown to successfully reproduce experimental data. It has been shown that microband electrodes can usefully be employed to simultaneously determine the diffusion coefficients of both members of a redox couple. Double potential step chronoamperometry was carried out on decamethylferrocene (DMFc) in the ionic liquid [Pmim][NTf_2] at both a microdisc electrode and a microband electrode, and it was found that the well established double potential step simulations for a disc produced the same diffusion coefficients as the program developed here for a microband electrode.

The following chapter extends this model for a single band to dual bands working in generator-collector mode, and simple procedure is proposed to determine the concentrations of two species in solution simultaneously.

References

[1] Barnes, E. O.; Xiong, L.; Ward, K. R.; Compton, R. G. *J. Electroanal. Chem.* **2013**, *701*, 59 – 68.

[2] Compton, R. G.; Banks, C. E. *Understanding Voltammetry*, 2nd ed.; World Scientific: Singapore, 2010.

[3] Aoki, K.; Osteryoung, J. *J. Electroanal. Chem.* **1981**, *122*, 19–35.

[4] Amatore, C.; Oleinick, A.; Svir, I. *Anal. Chem.* **2008**, *80*, 7947–7956.

[5] Barnes, E. O.; O'Mahony, A. M.; Aldous, L.; Hardacre, C.; Compton, R. G. *J. Electroanal. Chem.* **2010**, *646*, 11–17.

[6] Oldham, K. B. *J. Electroanal. Chem.* **1981**, *122*, 1–17.

[7] Heinze, J. *J. Electroanal. Chem.* **1981**, *124*, 73–86.

[8] Paddon, C. A.; Silvester, D. S.; Bhatti, F. L.; Donohoe, T. J.; Compton, R. G. *Electroanalysis* **2007**, *19*, 11–22.

[9] Shoup, D.; Szabo, A. *J. Electroanal. Chem.* **1982**, *140*, 237–245.

[10] Klymenko, O. V.; Evans, R. G.; Hardacre, C.; Svir, I. B.; Compton, R. G. *J. Electroanal. Chem.* **2004**, *571*, 211–221.

[11] Streeter, I.; Compton, R. G. *J. Phys. Chem. C* **2008**, *112*, 13716–13728.

[12] Barnes, E. O.; Lewis, G. E. M.; Dale, S. E. C.; Marken, F.; Compton, R. G. *Analyst* **2012**, *137*, 1068–1081.

[13] Bai, Y.-H.; Del Campo, J. F.; Tsai, Y.-C. *Biosens. Bioelectron.* **2013**, *42*, 17–22.

[14] Huan, T. N.; Hung, L. Q.; Ha, V. T. T.; Anh, N. H.; Khai, T. V.; Shim, K. B.; Chung, H. *Talanta* **2012**, *94*, 284 – 288.

[15] Metters, J. P.; Kadara, R. O.; Banks, C. E. *Sens. Actuators, B* **2012**, *169*, 136.

[16] Walsh, D. A.; Lovelock, K. R. J.; Licence, P. *Chem. Soc. Re v.* **2010**, *39*, 4185–4194.

[17] Broder, T. L.; Silvester, D. S.; Aldous, L.; Hardacre, C.; Crossley, A.; Compton, R. G. *New J. Chem.* **2007**, *31*, 966–972.

[18] Galvez, J.; Alcaraz, M.-L. *J. Electroanal. Chem.* **1992**, *341*, 15–34.

[19] Limon-Petersen, J. G.; Streeter, I.; Rees, N. V.; Compton, R. G. *J. Phys. Chem. C* **2009**, *113*, 333–337.

[20] http://www.nanoflux.com.sg/.

[21] http://micruxfluidic.com.

[22] Welford, P. J.; Freeman, J.; Wilkins, S. J.; Wadhawan, J. D.; Hahn, C. E. W.; Compton, R. G. *Anal. Chem.* **2001**, *73*, 6088–6092.

[23] Compton, R. G.; Fisher, A. C.; Wellington, R. G.; Dobson, P. J.; Leigh, P. A. *J. Phys. Chem.* **1993**, *97*, 10410–10415.

[24] Alden, J. A.; Compton, R. G.; Dryfe, R. A. *J. Electr* **1995**, *397*, 11–17.

[25] Alden, J. A.; Compton, R. G. *J. Electroanal. Chem.* **1996**, *404*, 27 – 35.

[26] Alden, J. A.; Compton, R. G. *J. Elec* **1996**, *402*, 1–10.

[27] Ueno, K.; Kim, H.-B.; Kitamura, N. *Anal. Chem.* **2003**, *75*, 2086–2091.

[28] Amatore, C.; Lemmer, C.; Sella, C.; Thouin, L. *Anal. Chem.* **2011**, *83*, 4170–4177.

[29] Amatore, C.; Lemmer, C.; Perrodin, P.; Sella, C.; Thouin, L. *Electrochem. Commun.* **2011**, *13*, 1459 – 1461.

[30] Matthews, S. M.; Shiddiky, M. J. A.; Yunus, K.; Elton, D. M.; Duffy, N. W.; Gu, Y.; Fisher, A. C.; Bond, A. M. *Anal. Chem.* **2012**, *84*, 6686–6692.

[31] Fosset, B.; Amatore, C. A.; Bartelt, J. E.; Michael, A. C.; Wightman, R. M. *Anal. Chem.* **1991**, *63*, 306–314.

[32] Unwin, P. R. *J. Electroanal. Chem.* **1991**, *297*, 103 – 124.

[33] Rajantie, H.; Williams, D. E. *Analyst* **2001**, *126*, 1882–1887.

[34] Paixão, T. R.; Matos, R. C.; Bertotti, M. *Electrochim. Acta* **2003**, *48*, 691 – 698.

[35] Svir, I. B.; Oleinick, A. I.; Compton, R. G. *J. Electroanal. Chem.* **2003**, *560*, 117–126.

[36] Amatore, C.; Sella, C.; Thouin, L. *J. Electroanal. Chem.* **2006**, *593*, 194 – 202.

[37] Compton, R. G.; Winkler, J. *J. Phys. Chem.* **1995**, *99*, 5029–5034.

[38] Alden, J. A.; Compton, R. G. *Electroanalysis* **1996**, *8*, 30–33.

[39] Aoki, K.; Tokuda, K.; Matsuda, H. *J. Ele* **1987**, *230*, 61.

[40] Barrosse-Antle, L. E.; Bond, A. M.; Compton, R. G.; O'Mahony, A. M.; Rogers, E. I.; Silvester, D. S. *Chem. Asian J.* **2010**, *5*, 202–230.

[41] Silvester, D. S.; Compton, R. G. *Z. Phys. Chem.* **2006**, *220*, 1247–1274.

[42] Xiong, L.; Fletcher, A. M.; Ernst, S.; Davies, S. G.; Compton, R. G. *Analyst* **2012**, *137*, 2567.

[43] Xiong, L.; Fletcher, A. M.; Davies, S. G.; Norman, S. E.; Hardacre, C.; Compton, R. G. *Analyst* **2012**, *137*, 4951.

[44] Buzzeo, M. C.; Klymenko, O. V.; Wadhawan, J. D.; Hardacre, C.; Seddon, K. R.; Compton, R. G. *J. Phys. Chem. A* **2003**, *107*, 8872–8878.

[45] Gavaghan, D. J. *J. Electroanal. Chem.* **1998**, *456*, 25–35.

[46] Gavaghan, D. J. *J. Electroanal. Chem.* **1998**, *456*, 13–23.

[47] Gavaghan, D. J. *J. Electroanal. Chem.* **1998**, *456*, 1–12.

[48] Press, W. H., Teukolsky, S. A., Vetterling, W. T., Flannery, B. P., Eds. *Numerical Recipes: The Art of Scientific Computing*; Cambridge University Press, 2007.

[49] Amatore, C.; Svir, I. *Journal of Electroanalytical Chemistry* **2003**, *557*, 75 – 90.

[50] Amatore, C.; Oleinick, A.; Svir, I. *Electrochem. Commun.* **2004**, *6*, 1123 – 1130.

[51] Barnes, E. O.; Zhou, Y.-G.; Rees, N. V.; Compton, R. G. *Journal of Electroanalytical Chemistry* **2013**, *691*, 28 – 34.

[52] Rogers, E. I.; Silvester, D. S.; Poole, D. L.; Aldous, L.; Hardacre, C.; Compton, R. G. *J. Phys. Chem. C* **2008**, *112*, 2729–2735.

[53] Evans, R. G.; Klymenko, O. V.; Saddoughi, S. A.; Hardacre, C.; Compton, R. G. *J. Phys. Chem. B* **2004**, *108*, 7878–7886.

[54] Meng, Y.; Aldous, L.; Compton, R. G. *J. Phys. Chem. C* **2011**, *115*, 14334–14340.

Chapter 6

Dual Band Electrodes in Generator−Collector Mode: Simultaneous Measurement of Two Species

Having developed a model for double potential step chronoamperometry at a single band electrode in the previous chapter, the electrochemistry of two band electrodes working in generator-collector mode is now studied. A computational model for the simulation of a double band generator-collector experiment is applied to the situation where two electrochemical reactions occur concurrently. It is shown that chronoamperometric measurements can be used to take advantage of any significant differences in diffusion coefficients to measure the concentrations of both electroactive species simultaneously, by measuring the time at which the collection efficiency reaches a specific value. The separation of the electrodes is shown not to affect the sensitivity of the method (in terms of percentage changes in the measured time to reach the specified collection efficiency), but wider gaps can provide a greater range of (larger) absolute values of this characteristic time. It is also shown that measuring the time taken to reach smaller collection efficiencies can allow for the detection of smaller amounts of whichever species diffuses faster. The case of a system containing both ascorbic acid and dopamine in water is used to exemplify the

method, and it is shown that mole fractions of ascorbic acid between 0.055 and 0.96 can, in principle, be accurately measured. This work, carried out in collaboration with Ms. G. E. M. Lewis, Dr. S. E. C. Dale and Prof F. Marken of the University of Bath, has been published in *The Journal of Electroanalytical Chemistry* [1].

6.1 Introduction

Generator-collector double electrode systems have found great utility in electrochemistry [2] since their conception in the late 1950s [3]. In general, a generator-collector experiment consists of a reduction (or oxidation) at the generator electrode:

$$\mathrm{A} \pm \mathrm{e}^- \rightleftharpoons \mathrm{B} \tag{6.1}$$

with a subsequent reaction, often the reverse of the first one, occurring at the collector electrode:

$$\mathrm{B} \mp \mathrm{e}^- \rightleftharpoons \mathrm{A} \tag{6.2}$$

The collection efficiency, N, is defined as the ratio of the current measured at the collector electrode to that measured at the generator electrode:

$$N = -\frac{I_{\mathrm{col}}}{I_{\mathrm{gen}}} \tag{6.3}$$

Measuring the collection efficiency can give information on the species involved in the reactions. If, for example, species B in the above scheme is unstable, and decomposes before it can reach the collector electrode, the collection efficiency will decrease, giving a measure of the rate at which the intermediate reaction occurs [4, 5].

A great variety of geometries of generator-collector systems have been studied. The earliest of these was Nekresov's original rotating ring disc [3], which was also extensively studied by Albery and coworkers [4–27], amongst others [28–37]. Other geometries include wall jet ring discs [38–45], dual band electrodes [46–78], dual discs [79–81] and hemispheres [82–85], and ring- or plane-recessed disc electrodes [86–88].

Many of these electrodes work in hydrodynamic mode, where forced convection flows the solution over the electrodes. This is an intrinsic feature of rotating ring disc electrodes and wall jet ring disc electrodes. Dual band electrodes can also be used in hydrodynamic mode by setting the electrodes in a flow cell, which will pump solution over the electrodes from the generator to the collector [50–53].

The uses of collector-generator systems have proved at least as varied as their geometries. In addition to the probing of follow up kinetics mentioned above, mechanistic details can be elucidated, for example the extent to which hydrogen peroxide plays a role as an intermediate in the reduction of oxygen to water [28–30]. Other areas in which generator-collector systems have been successfully employed include detection of micromolar concentrations [85], studies of triple phase boundaries [83], and measurement of one species in the presence of other, interfering, species [88].

Dual microband electrodes have been used analytically by Williams *et. al.* [46–48] in electrochemical titration experiments, where a species which has been electrogenerated at the generator electrode undergoes a reaction with a target analyte in solution. Any

surviving electrogenerated species is then detected at the collector electrode:

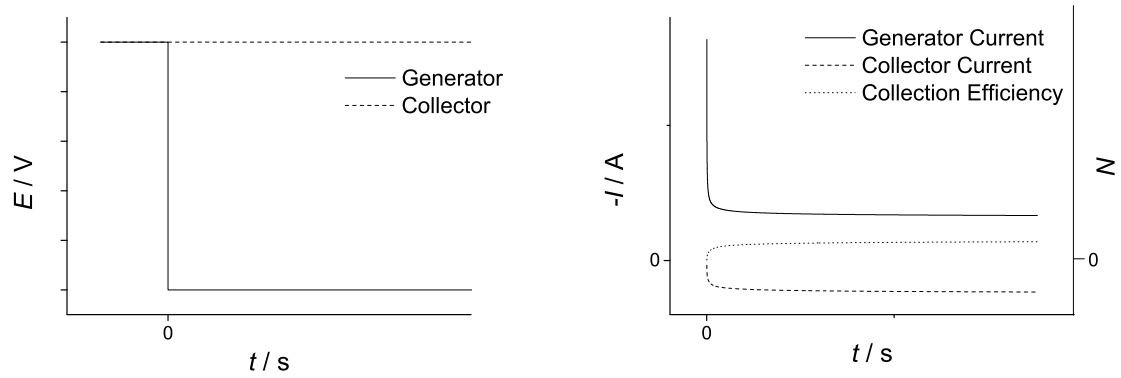
$$\mathrm{A} \pm \mathrm{e}^- \rightarrow \mathrm{B} \quad \text{Generator electrode} \tag{6.4}$$

$$\mathrm{B} + \mathrm{W} \rightarrow \mathrm{Z} \quad \text{Solution} \tag{6.5}$$

$$\mathrm{B} \mp \mathrm{e}^- \rightarrow \mathrm{A} \quad \text{Collector electrode} \tag{6.6}$$

Measuring the collection efficiency as a function of time yields information on the rate of the intermediate reaction, and hence the concentration of W, the target analyte. Further studies by Amatore *et. al.* [49] have theoretically investigated applying potential pulses to the generator electrode, and using the response at the collector electrode to obtain a time of flight for the electrogenerated species, and hence a measure of its diffusion coefficient.

In this chapter, we consider a chronoamperometric experiment using dual microband electrodes, with two electroactive species initially present in solution, A and X. Before the experiment starts, the potentials applied to both electrodes are such that no reduction occurs. At the beginning of the experiment, the potential applied to the generator electrode is stepped to a value such that reduction of the electroactive species A and X occurs at a mass transport controlled rate, forming B and Y. The potential at the collector electrode, however, remains at a value to re-oxidise the electrogenerated species at a mass transport controlled rate. Schematic representations of the applied potentials, the currents produced, and the collection efficiency as the experiment progresses are shown in Figure 6.1. The collection efficiency is seen to increase with time, and continues to do so until it approaches 1 as time $t \rightarrow \infty$. The rate at which it increases will be dependent on how quickly the intermediate species, B and Y, diffuse across the inter-electrode gap. If all species diffuse at the same rate, then the relative initial concentrations of A and X



(a) Potential (b) Current

Figure 6.1: Schematic diagram of (a) the potentials applied to the generator and collector electrodes during a chronoamperometric experiment and (b) the current responses and the collection efficiency.

will have no effect on how the collection efficiency varies with time.

If, however, the diffusion coefficients of the species produced at the generator are different, they will traverse the gap between the two electrodes at different rates, and thus the collection efficiencies attributable to each reaction will increase at different rates. The overall measured collection efficiency will therefore depend upon the relative concentrations of the two species. This chapter investigates the extent to which this is the case, and explores the application of this to the simultaneous determination of the concentration of both electroactive species in solution.

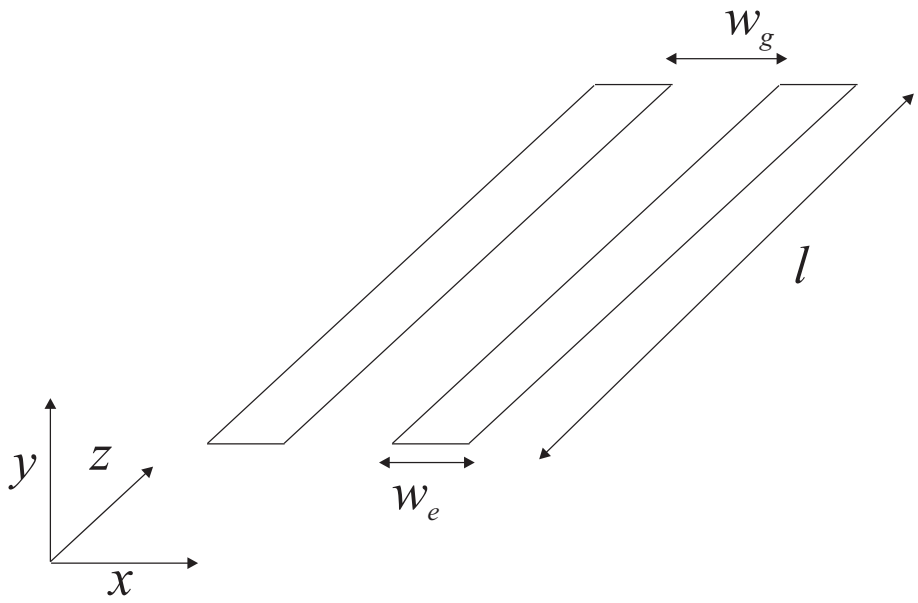


Figure 6.2: Schematic diagram of a dual microband electrode system.

6.2 Theory

In this chapter we consider potential step chronoamperometry at dual microband electrodes. Two concurrent one electron reductions are considered to occur:

$$\mathrm{A} + \mathrm{e}^- \rightleftharpoons \mathrm{B} \tag{6.7}$$

$$\mathrm{X} + \mathrm{e}^- \rightleftharpoons \mathrm{Y} \tag{6.8}$$

The dual microband electrodes are considered to be parallel and effectively of infinite length. One electrode (the generator electrode) has an applied potential such that the reductions both occur at a mass transport controlled rate, and the other electrode (the collector electrode) has an applied potential such that the reverse, oxidation, reactions occur at a mass transport controlled rate. A schematic diagram of the dual microband electrodes is shown in Figure 6.2, which also defines the Cartesian coordinates.

By considering the case where the length of the electrodes, l, is much greater than

their width, w_e, or the distance between them, w_g, the mass transport equation becomes two dimensional. Assuming an excess amount of inert supporting electrolyte is present, such that mass transport is diffusion only, the mass transport equation is:

$$\frac{\partial c_i}{\partial t} = D_i \left(\frac{\partial^2 c_i}{\partial x^2} + \frac{\partial^2 c_i}{\partial y^2} \right) \tag{6.9}$$

where c_i is the concentration of species i (mol m^{-3}), D_i is the diffusion coefficient of species i (m^2 s^{-1}), and x and y are the coordinates defined in Figure 6.2 (m). All symbols are defined in the Glossary. In dimensionless parameters, also defined in the Glossary, this equation becomes:

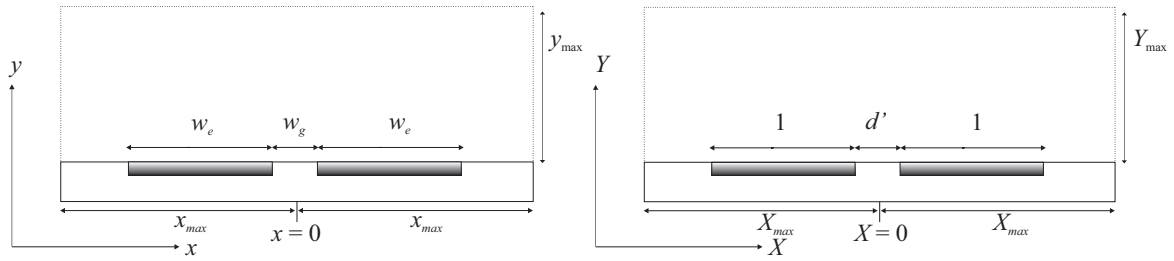
$$\frac{\partial C_i}{\partial \tau} = D_i^{'} \left(\frac{\partial^2 C_i}{\partial X^2} + \frac{\partial^2 C_i}{\partial Y^2} \right) \tag{6.10}$$

6.2.1 Boundary conditions

Initially, throughout solution, species A and X are present in their bulk concentrations, while species B and Y are not present at all:

$$\tau < 0; \text{ all } X; \text{ all } Y; \quad C_A = 1 \quad C_B = 0 \quad C_X = C_X^* \quad C_Y = 0 \tag{6.11}$$

(The simulation space, defining the spatial coordinates and electrode dimensions, is shown in Figure 6.3 in both real and dimensionless parameters). At time $\tau < 0$, the potentials at both electrodes are such that no reactions occur, neither species A nor X are reduced. At $\tau = 0$ the generator electrode potential is stepped to a value such that species A and X are reduced at a mass transport controlled rate. The collector electrode potential remains at the same value throughout the simulation, such that species B and Y are re-oxidised at a



(a) Real space (b) Dimensionless space

Figure 6.3: Schematic diagram of the simulation space used in this study in (a) real apsace and (b) dimensionless space.

mass transport controlled rate. The generator electrode boundary condition is therefore:

$$\tau \geq 0;\ -1-\frac{d'}{2} \leq X \leq -\frac{d'}{2};\ Y=0 \begin{cases} C_{\mathrm{A}}=0,\ D'_{\mathrm{B}}\left(\frac{\partial C_{\mathrm{B}}}{\partial Y}\right) = -\left(\frac{\partial C_{\mathrm{A}}}{\partial Y}\right) \\ C_{\mathrm{X}}=0,\ D'_{\mathrm{Y}}\left(\frac{\partial C_{\mathrm{Y}}}{\partial Y}\right) = -D'_{\mathrm{X}}\left(\frac{\partial C_{\mathrm{X}}}{\partial Y}\right) \end{cases} \tag{6.12}$$

and the collector electrode condition:

$$\tau \geq 0;\ \frac{d'}{2} \leq X \leq 1+\frac{d'}{2};\ Y=0 \begin{cases} \left(\frac{\partial C_{\mathrm{A}}}{\partial Y}\right) = -D'_{\mathrm{B}}\left(\frac{\partial C_{\mathrm{B}}}{\partial Y}\right),\ C_{\mathrm{B}}=0 \\ D'_{\mathrm{X}}\left(\frac{\partial C_{\mathrm{X}}}{\partial Y}\right) = -D'_{\mathrm{Y}}\left(\frac{\partial C_{\mathrm{Y}}}{\partial Y}\right),\ C_{\mathrm{Y}}=0 \end{cases} \tag{6.13}$$

On the insulating surface around (and between) the electrodes, a zero flux condition is imposed:

$$\tau \geq 0;\ Y=0; \begin{cases} -1-\frac{d'}{2} < X \\ -\frac{d'}{2} < X < \frac{d'}{2} \qquad \left(\frac{\partial C_{\mathrm{i}}}{\partial Y}\right)=0 \\ X > \frac{d'}{2}+1 \end{cases} \tag{6.14}$$

The bulk solution boundary is defined as being $6\sqrt{D'_{\max}\tau_{\max}}$ from the electrode surfaces in the X and Y directions, where $D_{\max}$ is the largest diffusion coefficient in the system

and $t_{\max}$ is the duration of the experiment. This is known to be well outside the diffusion layer [89–91]. At these boundaries, concentrations are set at their bulk values. Defining $X_{\max}$ as $\frac{d'}{2} + 1 + 6\sqrt{D'_{\max}\tau_{\max}}$ and $Y_{\max}$ as $6\sqrt{D'_{\max}\tau_{\max}}$:

$$\tau \geq 0; \begin{cases} X = -X_{\max}; \text{ all } Y \\ X = X_{\max}; \text{ all } Y \qquad C_{\mathrm{A}} = 1 \quad C_{\mathrm{B}} = 0 \quad C_{\mathrm{X}} = C^*_{\mathrm{X}} \quad C_{\mathrm{Y}} = 0 \\ \text{all } X;\ Y = Y_{\max} \end{cases} \tag{6.15}$$

These boundary conditions are summarised in Table 6.1.

The dimensionless current is calculated by integrating the flux of species A and X across the electrode surfaces. At the generator electrode, this is given by:

$$J_{\mathrm{gen}} = \int_{-\frac{d'}{2}}^{-1-\frac{d'}{2}} \left(\frac{\partial C_{\mathrm{A}}}{\partial Y}\right)_{Y=0} + D'_{\mathrm{X}} \left(\frac{\partial C_{\mathrm{X}}}{\partial Y}\right)_{Y=0} \mathrm{d}X \tag{6.16}$$

and at the collector electrode by:

$$J_{\mathrm{col}} = \int_{1+\frac{d'}{2}}^{\frac{d'}{2}} \left(\frac{\partial C_{\mathrm{A}}}{\partial Y}\right)_{Y=0} + D'_{\mathrm{X}} \left(\frac{\partial C_{\mathrm{X}}}{\partial Y}\right)_{Y=0} \mathrm{d}X \tag{6.17}$$

The collection efficiency is then given by:

$$N = -\frac{J_{\mathrm{col}}}{J_{\mathrm{gen}}} \tag{6.18}$$

<table>
<tr><th colspan="3">Boundary</th><th>Condition</th></tr>
<tr><td>$\tau < 0$</td><td>All X</td><td>All Y</td><td>$C_{\mathrm{A}} = 1$, $C_{\mathrm{B}} = 0$
$C_{\mathrm{X}} = C_{\mathrm{X}}^{*}$, $C_{\mathrm{Y}} = 0$</td></tr>
<tr><td rowspan="6">$\tau \geq 0$</td><td>$-1 - \frac{d'}{2} \leq X \leq -\frac{d'}{2}$</td><td rowspan="4">$Y = 0$</td><td>$C_{\mathrm{A}} = 0$, $D'_{\mathrm{B}} \left(\frac{\partial C_{\mathrm{B}}}{\partial Y}\right) = -\left(\frac{\partial C_{\mathrm{A}}}{\partial Y}\right)$
$C_{\mathrm{X}} = 0$, $D'_{\mathrm{Y}} \left(\frac{\partial C_{\mathrm{Y}}}{\partial Y}\right) = -D'_{\mathrm{X}} \left(\frac{\partial C_{\mathrm{X}}}{\partial Y}\right)$</td></tr>
<tr><td>$\frac{d'}{2} \leq X \leq 1 + \frac{d'}{2}$</td><td>$\left(\frac{\partial C_{\mathrm{A}}}{\partial Y}\right) = -D'_{\mathrm{B}} \left(\frac{\partial C_{\mathrm{B}}}{\partial Y}\right)$, $C_{\mathrm{B}} = 0$
$D'_{\mathrm{X}} \left(\frac{\partial C_{\mathrm{X}}}{\partial Y}\right) = -D'_{\mathrm{Y}} \left(\frac{\partial C_{\mathrm{Y}}}{\partial Y}\right)$, $C_{\mathrm{Y}} = 0$</td></tr>
<tr><td>$X < -1 - \frac{d'}{2}$</td><td rowspan="2">$\frac{\partial C_{\mathrm{i}}}{\partial Y} = 0$</td></tr>
<tr><td>$X > 1 + \frac{d'}{2}$</td></tr>
<tr><td>$X = -X_{\max}$</td><td rowspan="2">All Y</td><td rowspan="3">$C_{\mathrm{A}} = 1$, $C_{\mathrm{B}} = 0$
$C_{\mathrm{X}} = C_{\mathrm{X}}^{*}$, $C_{\mathrm{Y}} = 0$</td></tr>
<tr><td>$X = X_{\max}$</td></tr>
<tr><td>All X</td><td>$Y = Y_{\max}$</td></tr>
</table>

Table 6.1: Dimensionless boundary conditions for double potential step chronoamperometry simulations at dual microband electrodes.

6.2.2 Numerical methods

To obtain a numerical solution to the problem outlined above, the mass transport equation and the boundary conditions are discretised according to the Crank Nicolson method [92] and solved using the alternating direction implicit (ADI) method in conjunction with the Thomas algorithm [93] (as outlined in Chapter 2).

In addition to discretising the equations, spatial and temporal grids must be defined to solve the equations over. The temporal grid begins at $\tau_0 = 0$ and is initially linear, with a step size of $\Delta\tau$, until some switching time τ_s after which the grid expands:

$$\tau < \tau_s \quad \tau_k = \tau_{k-1} + \Delta\tau \tag{6.19}$$

$$\tau \geq \tau_s \quad \tau_k = \tau_{k-1} + \gamma_\tau \left(\tau_{k-1} - \tau_{k-2}\right) \tag{6.20}$$

The spatial grid in the Y direction simply expands away from the electrode/insulating surface. The first point, Y_0, is set as 0, and the second point some value ΔY. The rest of the grid is defined:

$$Y_j = \gamma_Y Y_{j-1} \tag{6.21}$$

In the X direction, the grid is similarly defined, and expands away from points located at both edges of each electrode, until it reaches either the centre of an electrode ($X = \pm\left(0.5 + \frac{d'}{2}\right)$), the centre of the inter-electrode gap ($X = 0$), or the edge of the simulation space. To achieve convergence, the following parameters were used: $\Delta\tau = 1 \times 10^{-7}$, $\tau_s = 1 \times 10^{-4}$, $\gamma_\tau = 1.0001$, $\Delta Y = 8 \times 10^{-5}$, $\gamma_Y = 1.125$. The model was programmed in C++, with multithreaded parallel programming employed to increase efficiency, and all simulations carried out on an Intel(R) Xenon(R) 2.26 GHz PC with 2.25 GB RAM.

6.3 Theoretical Results

6.3.1 Varying relative concentrations of species A and X

During a generator-collector chronoamperometry experiment, the collection efficiency will be a function of time, as a species created at the generator electrode needs to diffuse over to the collector electrode to be detected. If just a single electroactive species is present in solution, the rate at which the collection efficiency increases will be a function of the distance between the two electrodes, and the diffusion coefficient of the species in question. Species which diffuse more slowly will traverse the gap more slowly, resulting in a lower collection efficiency at any given time from the start of the experiment. It follows that if two separate experiments are run, one with reaction 6.7 and one with reaction 6.8, and species B and Y have different diffusion coefficients, then at any given time after the beginning of the experiment the measured collection efficiencies will be different. If both reactions occur together in the same experiment, the measured collection efficiency will be somewhere between the two individual cases.

This is exemplified in Figure 6.4, which shows simulated collection efficiencies for a variety of relative initial concentrations of species A and B. In the simulations, $D'_{\mathrm{A}} = D'_{\mathrm{B}} = 1$, $D'_{\mathrm{X}} = D'_{\mathrm{Y}} = 0.1$ and $d' = 0.1$. It is seen that as C_{X} approaches zero, the measured collection efficiency curves begin to converge on each other, eventually reaching the result obtained when only species A is present in solution. Conversely, as C_{X} becomes very large, the results converge on the limit where only species X is initially present in solution.

Using this result, the relative concentrations of species A and X in a solution of unknown composition can be determined. If the time taken for the collection efficiency to

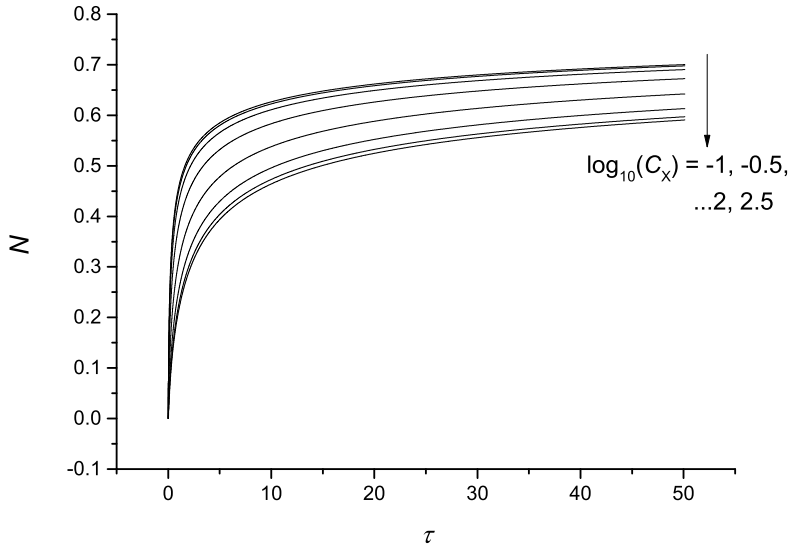


Figure 6.4: Collection efficiencies for various values of C_{X} as a function of dimensionless time. $d' = 0.1$, $D'_{\mathrm{B}} = D'_{\mathrm{A}} (= 1)$, $D'_{\mathrm{Y}} = D'_{\mathrm{X}} = 0.1$.

reach some specified value, say 0.5, is measured, and compared to a calibration curve, the relative concentrations of species A and X can be estimated. The absolute (un-normalised) values can then be calulated from the magnitudes of the collector and generator currents.

Figure 6.5 shows the dimensionless time taken for the collection efficiency to reach 0.5, $\tau_{0.5}$, for various values of C_{X} and D'_{X}. In each case, $d' = 0.1$, $D'_{\mathrm{B}} = D'_{\mathrm{A}}$ and $D'_{\mathrm{Y}} = D'_{\mathrm{X}}$. It is seen that the sensitivity of this method increases as the relevant diffusion coefficients become more and more different from each other (uppermost line in Figure 6.5). Conversely, when the diffusion coefficients are equal to each other, this method becomes completely insensitive to the solution composition. More specifically, it is seen that:

$$\frac{\tau_{0.5}^{C_{\mathrm{X}} \to \infty}}{\tau_{0.5}^{C_{\mathrm{X}}=0}} = \frac{D'_{\mathrm{A}}}{D'_{\mathrm{X}}} \tag{6.22}$$

so if species A and B diffuse 10 times faster than species X and Y, $\tau_{0.5}$ increases 10 fold

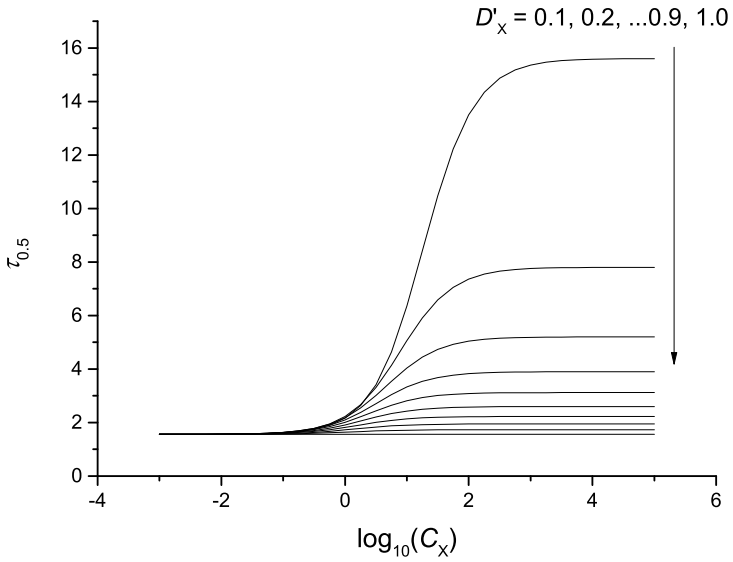


Figure 6.5: $\tau_{0.5}$, the time taken for the collection efficiency to reach 0.5, as a function of $\log_{10}(C_{\mathrm{X}})$, for various values of D'_{X}. $d' = 0.1$, $D'_{\mathrm{B}} = D'_{\mathrm{A}} (= 1)$, $D'_{\mathrm{Y}} = D'_{\mathrm{X}}$.

between the limits of only A initially present and only X initially present.

6.3.2 Effect of Inter-Electrode Distance

By changing the value of d', the effect of the inter-electrode distance on the sensitivity of this method to determine two concentration simultaneously can be investigated. Figure 6.6 (a) shows the calibration curves obtained when $D'_{\mathrm{X}} = 0.1$ for the three dimensionless inter-electrode distances $d' = 0.1$, 0.5 and 1. Figure 6.6 (b) shows these curves normalised to the values of $\tau_{0.5}$ obtained when $C_{\mathrm{X}} = 0$, $\tau_{0.5}^{C_{\mathrm{X}}=0}$. (c) and (d) show the same, but now for $D'_{\mathrm{X}} = 0.9$. It is seen from (a) and (c) that larger gaps between the electrodes produce larger absolute differences between the extremes of the calibration curves. The normalised curves, however, show that the values of $\tau_{0.5}$ taken relative to the lower extremes are completely insensitive to the inter-electrode distance, whether the diffusion coefficients are very different or nearly the same. This insensitivity (in the relative values) makes the

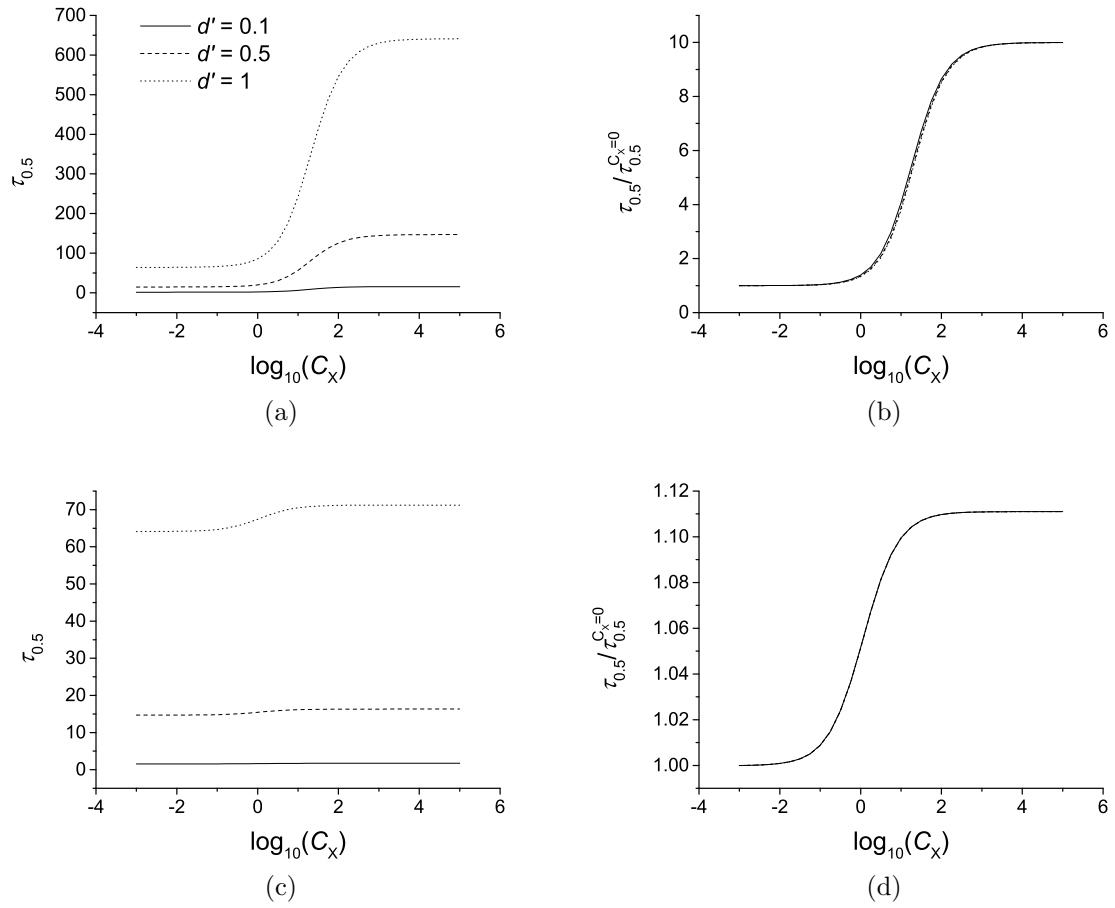
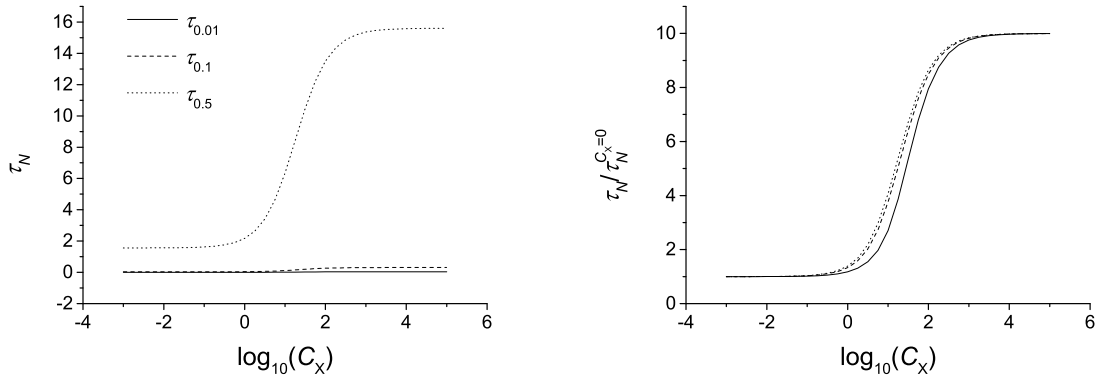


Figure 6.6: (a): Absolute values of $\tau_{0.5}$ as a function of $\log_{10}(C_{\mathrm{X}})$ for various gap sizes, with $D'_{\mathrm{X}} = 0.1$. (b): as (a), but $\tau_{0.5}$ values taken relative to its value when $C_{\mathrm{X}} = 0$ for each gap size. (c) and (d) as (a) and (b), except with $D'_{\mathrm{X}} = 0.9$.

ideal gap size a matter of experimental convenience. This may favour larger gap sizes which produce greater changes in the absolute values of $\tau_{0.5}$ across the calibration curve, although this must be balanced with the longer experimental timescales necessary with larger gaps.

6.3.3 Effect of the Chosen Collection Efficiency

In the above considerations, a collection efficiency of 0.5 was arbitrarily chosen as the point at which to construct the calibartion curves. Other points may however be used. Figure



(a) (b)

Figure 6.7: (a): Absolute values of τ_N as a function of $\log_{10}(C_{\mathrm{X}})$ for various values of N, with $d' = 0.1$ and $D'_{\mathrm{X}} = 0.1$. (b): as (a), but τ_N values taken relative to its value when $C_{\mathrm{X}} = 0$ for each value of N.

6.7 shows the calibration curves obtained by taking measurements at collection efficiencies of 0.01, 0.1 and 0.5, corresponding to $\tau_N = \tau_{0.01}$, $\tau_{0.1}$ and $\tau_{0.5}$ respectively. Figure 6.7 (a) shows the absolute τ_N values taken at each point, and Fiure 6.7 (b) shows these values relative to the lower extremes where $C_{\mathrm{X}} = 0$, $\tau_N^{C\mathrm{X}=0}$. In each case, $D'_{\mathrm{A}} = D'_{\mathrm{B}} = 1$, $D'_{\mathrm{X}} = D'_{\mathrm{Y}} = 0.1$ and $d' = 0.1$. The un-normalied plots show that calibration curves taken at higher collection efficiencies produce a much larger range of absolute τ values, with smaller collection efficiencies producing extremely small values of τ which may prove difficult to measure experimentally ($\tau_{0.01}$ varies between the extremes of 0.003689 and 0.03689). However, the normalised plots in Figure 6.7 (b) show that using a smaller collection efficiency, here 1%, can make the calibration curve sensitive to smaller (relative) concentrations of species A, the faster diffusing species (*i.e.* higher values of C_{X}). If, therefore, the difficulties in accurately measuring such small times can be overcome, using a small collection efficiency as the basis of the calibration curve may be desirable if one of the two species (the faster diffusing one) is present in trace quantities.

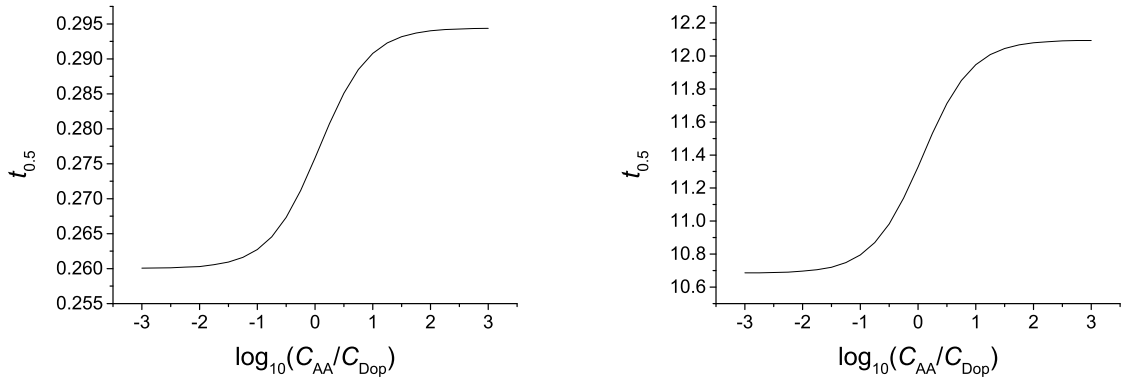
6.3.4 Theoretical Application to Simultaneous Measurement of Ascorbic Acid and Dopamine

Ascorbic acid (AA) and dopamine (Dop) are biologically important molecules, both vital to human health, and a great deal of research has been conducted to detect one in the presence of the other (see for example [88, 94, 95]). To show how this method of measuring the concentration of two species simultaneously can be used, these two molecules are taken as examples. Dual band chronoamperometry is simulated, oxidising AA and Dop at the generator electrode and re-reducing them at the collector. The diffusion coefficients of AA and Dop in water have been measured as 0.53×10^{-5} and 0.60×10^{-5} cm^2 s^{-1} respectively [96], and the diffusion coefficients of the oxidised species are assumed to be the same as for the parent species. The band electrodes are taken to be 10 μm in width, and two gap sizes are considered, 1 μm and 10 μm. The simulated calibration curves produced are shown in Figure 6.8. For both inter-electrode distances, the central 90% of the $\tau_{0.5}$ range covers values of $c_{\mathrm{AA}}/c_{\mathrm{Dop}}$ ranges of 0.058 to 21.88 (corresponding to mole fractions of AA of 0.055 to 0.96).

6.4 Summary of Method

The steps involved in using this method to simultaneously determine two concentrations can be summarised as follows:

i) Construct [97] or purchase dual microband electrodes of known dimensions. A larger inter-electrode distance will result in a greater range of times to reach a given collection efficiency, although the relative sensitivity is not affected by the inter-electrode



(a) $w_e = 1$ µm (b) $w_e = 10$ µm

Figure 6.8: $t_{0.5}$ as a function of $\log_{10}(\frac{C_{\mathrm{AA}}}{C_{\mathrm{Dop}}})$. Electrode widths, $w_e = 10$ μm. (a): Gap size, $w_g = 1\mu$m, (b): Gap size, $w_g = 10$ μm.

distance.

ii) If the diffusion coefficients of species A, B, X and Y are unknown, these should be measured using single and/or double potential step chronoamperometry at a single electrode (*e.g.* a microdisc).

iii) Construct a calibration curve of relative concentration plotted against the time taken for the collection efficiency to reach a certain value when performing potential step chronoamperometry at dual microband electrodes. This can be done computationally as outlined above, or experimentally using solutions of known relative concentrations. Choosing a smaller collection efficiency will allow for more accurate measurement of trace amounts of the faster diffusing species, but will also require smaller timescales to be accurately measured.

iv) The time taken for the collection efficiency to reach the specified value can then be measured for a solution of unknown composition, and the relative concentrations determined from the calibration curve.

It should be noted that in this work, only analytes which do not undergo follow up homogeneous kinetics are considered. The effect of homogeneous kinetics would lower the collection efficiencies, and will add some difficulties in selecting an appropriate collection efficiency target and electrode geometry (the previously advantageous larger gap size would now only further decrease collection efficiencies as follow up kinetics have longer to progress). Further, the scope of this work only includes electron transfers in the infinitely fast Nernstian limit. The effect of slower electron transfer on chronoamperometry has been studied by this group previously [98], and its application to this method is facile.

6.5 Conclusions

In this chapter, we have demonstrated the use of dual microband electrodes in chronoamperometric generator/collector mode to detect the concentrations of two competing electroactive species simultaneously, provided the diffusion coefficients involved are known or separately measured, and are not equal to each other. An example case of ascorbic acid and dopamine in water was examined computationally, and a theoretical range of detectable mole fractions of ascorbic acid was found to be between 0.055 and 0.96. It has been shown that the timescales involved using dual bands in this method are reasonable and easily measurable, whereas an interdigitated array, for example, would produce high collection efficiencies at much shorter and harder to measure times. A further possible example where this could be usefully applied would be for detecting the relative concentrations of two enantiomers, which could be given different diffusion coefficients by the use of a chiral solvent. After calibration, the experimental ease of this method makes it ideal for use in detecting the individual concentrations of two otherwise difficult to discriminate

species in a quick and cheap manner.

The next chapter develops a model to simulate cyclic voltammetry at interdigitated band electrode arrays and interdigitated ring electrode arrays in generator-collector mode, and compares the two geometries.

References

[1] Barnes, E. O.; Lewis, G. E. M.; Dale, S. E. C.; Marken, F.; Compton, R. G. *J. Electroanal. Chem.* **2013**, *703*, 38 – 44.

[2] Barnes, E. O.; Lewis, G. E. M.; Dale, S. E. C.; Marken, F.; Compton, R. G. *Analyst* **2012**, *137*, 1068 – 1081.

[3] Frumkin, A.; Nekrasov, L.; Levich, B.; Ivanov, J. *J. Electroanal. Chem.* **1959**, *1*, 84 – 90.

[4] Albery, W. J.; Bruckenstein, S. *Trans. Faraday Soc.* **1966**, *62*, 1946 – 1954.

[5] Albery, W. J.; Bruckenstein, S. *Trans. Faraday Soc.* **1966**, *62*, 2584 – 2595.

[6] Albery, W. J. *Trans. Faraday Soc.* **1966**, *62*, 1915 – 1919.

[7] Albery, W. J.; Bruckenstein, S. *Trans. Faraday Soc.* **1966**, *62*, 1920 – 1931.

[8] Albery, W. J.; Bruckenstein, S.; Napp, D. T. *Trans. Faraday Soc.* **1966**, *62*, 1932 – 1937.

[9] Albery, W. J.; Bruckenstein, S.; Johnson, D. C. *Trans. Faraday Soc.* **1966**, *62*, 1938 – 1945.

[10] Albery, W. J.; Bruckenstein, S. *Trans. Faraday Soc.* **1966**, *62*, 2596 – 2606.

[11] Albery, W. J. *Trans. Faraday Soc.* **1967**, *63*, 1771 – 1781.

[12] Albery, W. J.; Hitchman, M. L.; Ulstrup, J. *Trans. Faraday Soc.* **1968**, *64*, 2831 – 2840.

[13] Albery, W. J.; Hitchman, M. L.; Ulstrup, J. *Trans. Faraday Soc.* **1969**, *65*, 1101 – 1112.

[14] Albery, W. J. *Trans. Faraday Soc.* **1971**, *67*, 153 – 160.

[15] Albery, W. J.; Drury, J. S.; Hitchman, M. L. *Trans. Faraday Soc.* **1971**, *67*, 161 – 165.

[16] Albery, W. J.; Drury, J. S.; Hitchman, M. L. *Trans. Faraday Soc.* **1971**, *67*, 166 – 169.

[17] Albery, W. J.; Drury, J. S.; Hitchman, M. L. *Trans. Faraday Soc.* **1971**, *67*, 2162 – 2166.

[18] Albery, W. J.; Drury, J. S.; Hutchinson, A. P. *Trans. Faraday Soc.* **1971**, *67*, 2414 – 2418.

[19] Albery, W. J.; Drury, J. S. *J. Chem. Soc., Faraday Trans. 1* **1972**, *68*, 456 – 464.

[20] Bruckenstein, S.; Tokuda, K.; Albery, W. J. *J. Chem. Soc., Faraday Trans. 1* **1977**, *73*, 823 – 829.

[21] Albery, W. J. *J. Chem. Soc., Faraday Trans. 1* **1978**, *74*, 1007 – 1019.

[22] Albery, W. J.; Hillman, A. R. *J. Chem. Soc., Faraday Trans. 1* **1979**, *75*, 1623 – 1634.

[23] Albery, W. J.; Boutelle, M. G.; Colby, P. J.; Hillman, A. R. *J. Chem. Soc., Faraday Trans. 1* **1982**, *78*, 2757 – 2763.

[24] Albery, W. J.; Calvo, E. J. *J. Chem. Soc., Faraday Trans. 1* **1983**, *79*, 2583 – 2596.

[25] Albery, W. J.; Mount, A. R. *J. Chem. Soc., Faraday Trans. 1* **1989**, *85*, 1181 – 1188.

[26] Albery, W. J.; Mount, A. R. *J. Chem. Soc., Faraday Trans. 1* **1989**, *85*, 1189 – 1198.

[27] Albery, W. J.; Mount, A. R. *J. Chem. Soc., Faraday Trans. 1* **1989**, *85*, 3717 – 3724.

[28] Damjanovic, A.; Genshaw, M. A.; Bockris, J. O. *J. Phys Chem.* **1966**, *70*, 3761 – 3762.

[29] Damjanovic, A.; Genshaw, A. M. A.; Bockris, J. O. *J. Electrochem. Soc.* **1967**, *114*, 1107 – 1112.

[30] Damjanovic, A.; Genshaw, M. A.; Bockris, J. O. *J. Electrochem. Soc.* **1967**, *114*, 466 – 72.

[31] Damjanovic, A.; Genshaw, M. A.; Bockris, J. O. *J. Chem. Phys.* **1966**, *45*, 4057–4059.

[32] Genshaw, M. A.; Damjanovic, A.; Bockris, J. O. *J. Phys. Chem.* **1967**, *71*, 3722–3731.

[33] Nekrasov, L. N.; Khrushcheva, E. I. *Elektrokhimiya* **1967**, *3*, 166–172.

[34] Nekrasov, L. N.; Krushcheva, E. I. *Elektrokhimiya* **1967**, *3*, 677–680.

[35] Khrushcheva, E. I.; Nekrasov, L. N.; Shumilova, N. A.; Tarasevich, M. R. *Elektrokhimiya* **1967**, *3*, 831–835.

[36] Kramm, U. I.; Herrmann-Geppert, I.; Bogdanoff, P.; Fiechter, S. *J. Phys. Chem. C* **2011**, *115*, 23417–23427.

[37] Wu, J.; Dun, Z.; Wang, Y.; Wan, Y.; Hou, B. *J. Power Sources* **2012**, *198*, 122–126.

[38] Brett, C. M. A.; Neto, M. M. P. M. *J. Electroanal. Chem.* **1989**, *258*, 345 – 355.

[39] Brett, C. M. A.; Oliveira Brett, A. M. C. F.; Compton, R. G.; Fisher, A. C.; Tyley, G. P. *Electroanalysis* **1991**, *3*, 631 – 636.

[40] Compton, R. G.; Fisher, A. C.; Latham, M. H.; Brett, C. M. A.; Oliveira Brett, A. M. C. F. *J. Appl. Electrochem.* **1992**, *22*, 1011 – 1016.

[41] Albery, W. J.; Brett, C. M. A. *J. Electroanal. Chem.* **1983**, *148*, 201 – 210.

[42] Albery, W. J.; Brett, C. M. A. *J. Electroanal. Chem.* **1983**, *148*, 211 – 220.

[43] Compton, R. G.; Fisher, A. C.; Latham, M. H.; Wellington, R. G.; Brett, C. M. A.; Oliveira Brett, A. M. C. F. *J. Appl. Electrochem.* **1993**, *23*, 98–102.

[44] Sue, J.-W.; Ku, H.-H.; Chung, H.-H.; Zen, J.-M. *Electrochem. Commun.* **2008**, *10*, 987 – 990.

[45] Yang, T.-H.; Venkatesan, S.; Lien, C.-H.; Chang, J.-L.; Zen, J.-M. *Electrochim. Acta* **2011**, *56*, 6205 – 6210.

[46] Rajantie, H.; Strutwolf, J.; Williams, D. E. *J. Electroanal. Chem.* **2001**, *500*, 108 – 120.

[47] Rajantie, H.; Williams, D. E. *Analyst* **2001**, *126*, 1882 – 1887.

[48] Rajantie, H.; Williams, D. E. *Analyst* **2001**, *126*, 86 – 90.

[49] Amatore, C.; Sella, C.; Thouin, L. *J. Electroanal. Chem.* **2006**, *593*, 194 – 202.

[50] Aoki, K.; Tokuda, K.; Matsuda, H. *J. Electroanal. Chem.* **1977**, *79*, 49 – 78.

[51] Fisher, A. C.; Compton, R. G. *J. Appl. Electrochem.* **1991**, *21*, 208 – 212.

[52] Compton, R. G.; Stearn, G. M. *J. Chem. Soc., Faraday Trans. 1* **1988**, *84*, 4359 – 4367.

[53] Cooper, J. A.; Compton, R. G. *Electroanalysis* **1998**, *10*, 141 – 155.

[54] Schieffer, G. W.; Blaedel, W. J. *Anal. Chem.* **1977**, *49*, 49–53.

[55] Schieffer, G. W.; Blaedel, W. J. *Anal. Chem.* **1978**, *50*, 99–102.

[56] Coles, B. A.; Dryfe, R. A.; Rees, N. V.; Compton, R. G.; Davies, S. G.; McCarthy, T. D. *J. Electroanal. Chem.* **1996**, *411*, 121 – 127.

[57] Paixão, T. R.; Matos, R. C.; Bertotti, M. *Electrochim. Acta* **2003**, *48*, 691 – 698.

[58] Amatore, C.; Oleinick, A.; Svir, I. *Electrochem. Commun.* **2004**, *6*, 1123 – 1130.

[59] Thompson, M.; Compton, R. G. *J. Electroanal. Chem.* **2005**, *583*, 318–326.

[60] Amatore, C.; Oleinick, A.; Klymenko, O. V.; Svir, I. *ChemPhysChem* **2005**, *6*, 1581–1589.

[61] Klymenko, O. V.; Oleinick, A. I.; Amatore, C.; Svir, I. *Electrochim. Acta* **2007**, *53*, 1100 – 1106.

[62] Amatore, C.; Da Mota, N.; Lemmer, C.; Pebay, C.; Sella, C.; Thouin, L. *Anal. Chem.* **2008**, *80*, 9483–9490.

[63] Gerischer, H.; Mattes, I.; Braun, R. *J. Electroanal. Chem.* **1965**, *10*, 553 – 567.

[64] Braun, R. *J. Electroanal. Chem.* **1968**, *19*, 23 – 35.

[65] Unwin, P. R. *J. Electroanal. Chem.* **1991**, *297*, 103 – 124.

[66] Compton, R. G.; Coles, B. A.; Gooding, J. J.; Fisher, A. C.; Cox, T. I. *J. Phys. Chem.* **1994**, *98*, 2446–2451.

[67] Sasaki, H.; Maeda, M. *J. Electrochem. Soc.* **2010**, *157*, C414–C418.

[68] Sasaki, H.; Miyake, M.; Maeda, M. *J. Electrochem. Soc.* **2010**, *157*, E82–E87.

[69] Shrestha, B. R.; Yadav, A. P.; Nishikata, A.; Tsuru, T. *Electrochim. Acta* **2011**, *56*, 9714 – 9720.

[70] Compton., R. G.; Prtichard, K. L.; Unwin, P. R. *Freshwater Biol.* **1989**, *22*, 285–288.

[71] Compton, R. G.; Pritchard, K. L.; Unwin, P. R.; Grigg, G.; Silverster, P.; Lees, M.; House, W. A. *J. Chem. Soc., Faraday Trans. 1* **1989**, *85*, 4335–4366.

[72] Barwise, A. J.; Compton, R. G.; Uniwin, P. R. *J. Chem. Soc., Faraday Trans. 1* **1990**, *86*, 137–144.

[73] Unwin, P. R.; Compton, R. G. *J. Chem. Soc., Faraday Trans. 1* **1990**, *86*, 1517–1525.

[74] Compton, R. G.; Pritchard, K. L. *J. Chem. Soc., Faraday Trans.* **1990**, *86*, 129–136.

[75] Orton, R.; Unwin, P. R. *J. Chem. Soc., Faraday Trans.* **1993**, *89*, 3947–3954.

[76] Compton, R. G.; Harding, M. S.; Pluck, M. R.; Atherton, J. H.; Brennan, C. M. *J. Phys. Chem.* **1993**, *97*, 10416–10420.

[77] Hill, E.; Compton, R. G. *Res. Chem. Kinet.* **1997**, *4*, 203–229.

[78] Wilkins, S. J.; Compton, R. G.; Taylor, M. A.; Viles, H. A. *J. Colloid Interface Sci.* **2001**, *236*, 354 – 361.

[79] Phillips, C. G.; Stone, H. *J. Electroanal. Chem.* **1997**, *437*, 157 – 165.

[80] Baur, J. E.; Motsegood, P. N. *J. Electroanal. Chem.* **2004**, *572*, 29 – 40.

[81] Cutress, I. J.; Wang, Y.; Limon-Petersen, J. G.; Dale, S. E. C.; Rassaei, L.; Marken, F.; Compton, R. G. *J. Electroanal. Chem.* **2011**, *655*, 147 – 153.

[82] Fulian, Q.; Williams, N. A.; Fisher, A. C. *Electrochem. Commun.* **1999**, *1*, 124 – 127.

[83] French, R. W.; Chan, Y.; Bulman-Page, P. C.; Marken, F. *Electrophoresis* **2009**, *30*, 3361 – 3365.

[84] French, R.; Marken, F. *J. Solid State Electrochem.* **2009**, *13*, 609 – 617.

[85] Dale, S. E. C.; Vuorema, A.; Ashmore, E. M. Y.; Kasprzyk-Horden, B.; Sillanpää, M.; Denuault, G.; Marken, F. *Chem. Rec.* **2012**, *12*, 143 – 148.

[86] Menshykau, D.; del Campo, F. J.; Muoz, F. X.; Compton, R. G. *Sens. Actuators B* **2009**, *138*, 362 – 367.

[87] Menshykau, D.; O'Mahony, A. M.; del Campo, F. J.; Munoz, F. X.; Compton, R. G. *Anal. Chem.* **2009**, *81*, 9372 – 9382.

[88] Zhu, F.; Yan, J.; Lu, M.; Zhou, Y.; Yang, Y.; Mao, B. *Electrochim. Acta* **2011**, *56*, 8101 – 8107.

[89] Gavaghan, D. J. *J. Electroanal. Chem.* **1998**, *456*, 25 – 35.

[90] Gavaghan, D. J. *J. Electroanal. Chem.* **1998**, *456*, 13 – 23.

[91] Gavaghan, D. J. *J. Electroanal. Chem.* **1998**, *456*, 1 – 12.

[92] Crank, J.; Nicolson, E. *Proc. Camb. Phil. Soc.* **1947**, *43*, 50 – 67.

[93] Press, W. H., Teukolsky, S. A., Vetterling, W. T., Flannery, B. P., Eds. *Numerical Recipes: The Art of Scientific Computing*; Cambridge University Press, 2007.

[94] Oliveira, A. X.; Silva, S. M.; Leite, F. R. F.; Kubota, L. T.; Damos, F. S.; Luz, R. C. S. *Electroanalysis* **2013**, *25*, 723 – 731.

[95] Zhang, B.; Huang, D.; Xu, X.; Alemu, G.; Zhang, Y.; Zhan, F.; Shen, Y.; Wang, M. *Electrochim. Acta* **2013**, *91*, 261 – 266.

[96] Gerhardt, G.; Adams, R. N. *Anal. Chem.* **1982**, *54*, 2618 – 2620.

[97] Williams, D. E.; Ellis, K.; Colville, A.; Dennison, S. J.; Laguillo, G.; Larsen, J. *J. Electroanal. Chem.* **1997**, *432*, 159 – 169.

[98] Belding, S. R.; Rogers, E. I.; Compton, R. G. *J. Phys. Chem. C* **2009**, *113*, 4202 – 4207.

Chapter 7

Interdigitated Ring Arrays: Theory and Experiment

In this chapter, the oxidation of potassium ferrocyanide, $K_4Fe(CN)_6$, in aqueous solution under fully supported conditions is investigated at interdigitated band and ring electrode arrays, and compared to theoretical models developed to simulate the processes. Simulated data is found to fit well with experimental results using literature values of diffusion coefficients for $Fe(CN)_6^{4-}$ and $Fe(CN)_6^{3-}$. The theoretical models are used to compare responses from interdigitated band and ring arrays, and the size of ring array required to approximate the response to a linear band array is investigated. An equation is developed for the radius of ring required for a pair of electrodes in a ring array to give a result with 5% of a pair of electrodes in a band array. This equation is found to be independent of the scan rate used over six orders of magnitude. This work has been published in *The Journal of Electroanalytical Chemistry* [1]. Experiments in this chapter were carried out by Dr. Anna Fernández-la-Villa, Dr. Diego F. Pozo-Ayuso and Dr. Mario Castaño-Álvarez of Micrux Technologies®.

7.1 Introduction

Microelectrode arrays are widely employed in electrochemistry [2, 3], since they can provide the advantages of microelectrodes (fast mass transport, the use of two rather than three electrode control, observation of steady state currents) whilst providing the large currents usually associated with macroelectrodes. These arrays also have considerably less capacitative current than macroelectrodes, although generally more than isolated microelectrodes, representing an intermediate case [4]. However, while single microelectrodes typically have a much smaller ohmic drop than macroelectrodes (due to the smaller currents drawn), a microelectrode array has significantly larger ohmic drop than a macroelectrode of equivalent overall area [2]. The main types of array electrodes are arrays of microdiscs (where the array may be regular or random) and arrays of microbands.

Microband arrays, as well as a single pair of bands, have been used as generator-collector systems [5–13], with great success. In a collector generator system, some target species in solution is oxidised (or reduced) at the generator electrode, with the product of this reaction then detected by re-reduction (or oxidation) at the collector electrode, as outlined in Chapter 6. If single step chronoamperometry, for example, were to be carried out, then some species might would be oxidised at the generator electrode to produce species B, which would then be reduced at the collector electrode, both under diffusion control:

$$\mathrm{A} \pm \mathrm{e}^- \rightarrow \mathrm{B} \quad \text{Generator} \tag{7.1}$$

$$\mathrm{B} \mp \mathrm{e}^- \rightarrow \mathrm{A} \quad \text{Collector} \tag{7.2}$$

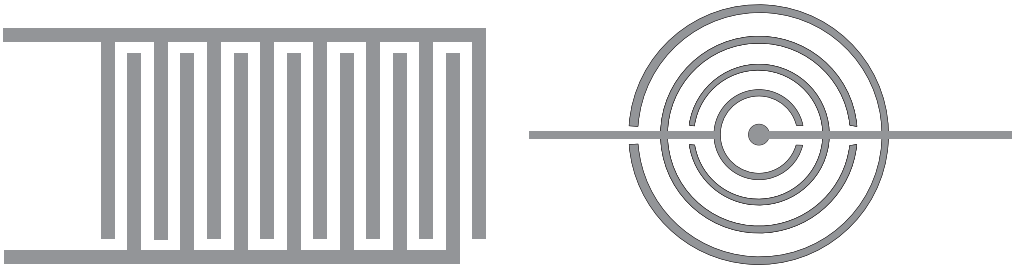
An important feature in an experiment of this type is the collection efficiency, N, the ratio of the collector current to the generator current, again described in Chapter 6:

$$N = -\frac{I_{\text{col}}}{I_{\text{gen}}} \tag{7.3}$$

This simple experiment can be extended to performing cyclic voltammetry at the generator electrode, while keeping the collector electrode fixed at the potential to reduce species B. This approach has been used to study, for example, competing modes of transport at a phase boundary (transport along the interface vs transport in bulk) [14]. Other uses of collector generator systems include mechanistic investigations [15–18], probing intermediate kinetics [19, 20], electrochemical sensing with very low detection limits [21], targeted detection of one species in the presence of another [22], and as shown in the previous chapter, the simultaneous measurement of two species [23].

Microband arrays lend themselves particularly well to generator-collector systems. They consist of a series of parallel bands, which alternate between being generator and collector. This is shown in Figure 7.1(a), and the apparatus is known as an interdigitated band array (IDBA). This ensures a very high collection efficiency [24], since any species produced at the generator electrode is likely to diffuse to the collector electrode with a high probability of detection if the separation is small. This spatial arrangement also allows for efficient redox cycling [24], where species cycle between generator and collector electrodes, enhancing the measured current.

IDBAs have been used to simultaneously measure both the concentration and diffusion coefficient of a species. Aoki *et. al.* [9] developed a theoretical equation for the steady state current produced at a parallel microband array electrode during a chronoampero-



(a) IDBA (b) IDRA

Figure 7.1: Schematic diagram of the two interdigitated arrays investigated in this chapter.

metric experiment as outlined above:

$$I_{SS} = nFDc^{*}l\frac{K(1-p)}{K(p)} \tag{7.4}$$

where I_{ss} is the steady state current (A), n is the number of electrons transferred, F is the Faraday constant, D is the diffusion coefficient of the species under investigation ($m^2\ s^{-1}$), c^* is this species' bulk concentration (mol m^{-3}), l is the length of the individual band electrodes (m), and p is some function of the electrode geometry. The function K is a total elliptic integral, and $K(1-p)/K(p)$ can be approximated as:

$$\frac{K(1-p)}{K(p)} \approx 0.318\ln\left[2.55\left(1+\frac{w_e}{w_g}\right)\right] - 0.095\left(1+\frac{w_e}{w_g}\right)^{-2} \tag{7.5}$$

where w_g and w_e are the inter-electrode distance and the electrode width respectively. Also developed was an empirical equation to described the time taken for the current at the collector electrode to reach half of its steady state value, $t_{0.5}$:

$$t_{0.5} \approx 0.90\frac{\left(w_g+\frac{w_e}{6}\right)^2}{D} \tag{7.6}$$

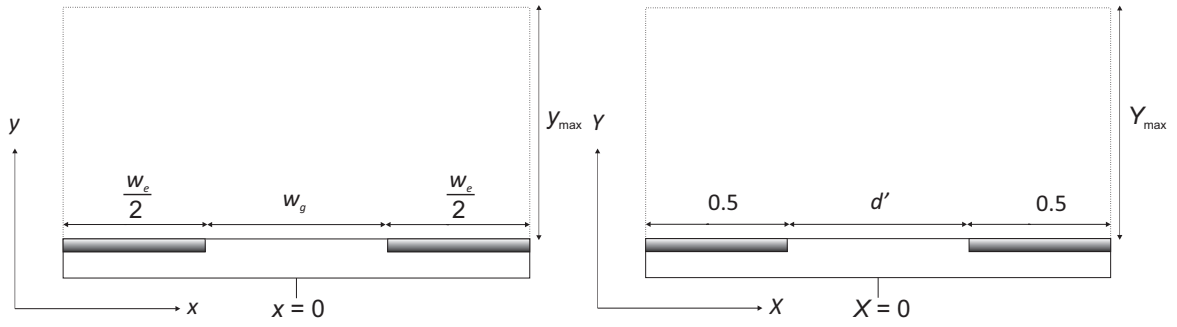
So by measuring the steady state current and the time taken to reach half this value,

equations 7.4 and 7.6 can be solved simultaneously to determine c^* and D.

A convenient and important variation on IDBAs are interdigitated ring electrode arrays, IDRAs [25]. a schematic of an IDRA is shown in Figure 7.1(b). They consist of a central disc electrode (throughout this chapter considered to be a generator electrode) surrounded by expanding concentric ring electrodes which alternate between collector and generator in character. The obvious difference between this and an IDBA is the cylindrical nature of the diffusion. The radial component will, at least for rings of small radii, enhance the mass transport between the electrodes, leading to an increased rate of redox cycling and a greater current enhancement in comparison with linear IDBAs. For very large rings, however, the diffusion will be become less cylindrical and these effects will be lost, with the behavior tending to that of parallel bands. This chapter investigates the extent to which this is the case, and explores how well experiments carried out at an IDRA can be simulated a simplified IDBA model.

7.2 Theory

Cyclic voltammetry is simulated at both linear interdigitated arrays (IDBAs) and interdigitated ring arrays (IDRAs), shown in Figure 7.1(a) and 7.1(b) respectively. In each case, a single electroactive species, A, is considered to be initially present in solution, along with a large amount of an inert electrolyte to suppress electric fields and render the mass transport diffusion only. The generator electrodes are subject to a linearly sweeping potential to set up a potential dependent equilibrium between species A and its oxidised form, species B, while the collector electrodes are set at a fixed potential to reduce species



(a) Dimensional simulation space (b) Dimensionless simulation space

Figure 7.2: Schematic diagram of the IDBA simulation space used in this study in (a) real space and (b) dimensionless space.

B at a mass transport controlled rate:

$$\mathrm{A} \pm \mathrm{e}^- \rightleftharpoons \mathrm{B} \quad \text{Generator} \tag{7.7}$$

$$\mathrm{B} \mp \mathrm{e}^- \rightarrow \mathrm{A} \quad \text{Collector} \tag{7.8}$$

7.2.1 Interdigitated band arrays

To simulate an interdigitated band array, we make the assumption that the electrodes are much longer than they are wide, as in the previous two chapters. This reduces the problem from three dimensions to two, and the mass transport equation (in dimensionless parameters) is:

$$\frac{\partial C_\mathrm{i}}{\partial \tau} = D_\mathrm{i}^{'} \left(\frac{\partial^2 C_\mathrm{i}}{\partial X^2} + \frac{\partial^2 C_\mathrm{i}}{\partial Y^2} \right) \tag{7.9}$$

Dimensionless parameters are discussed in Chapter 2 and a full list, with definitions, is given in the Glossary. The simulation space which this is solved over is shown schematically in Figure 7.2(a). The mass transport equation is solved subject to boundary condi-

tions. At the generator electrode surface, Butler-Volmer kinetics are applied:

$$\frac{\partial C_{\mathrm{A}}}{\partial Y} = K^0 C_{\mathrm{A}}^0 \exp\left[-\alpha\theta\right] - K^0 C_{\mathrm{B}}^0 \exp\left[(1-\alpha)\,\theta\right] \tag{7.10}$$

and equal fluxes of species are maintained by virtue of conservation of mass:

$$D_{\mathrm{B}}^{'}\left(\frac{\partial C_{\mathrm{B}}}{\partial Y}\right) = \left(\frac{\partial C_{\mathrm{A}}}{\partial Y}\right) \tag{7.11}$$

At the collector electrode surface, the potential is such that species B is reduced to species A and a mass transport controlled rate, and equal fluxes are again maintained:

$$C_{\mathrm{B}} = 0 \tag{7.12}$$

$$\left(\frac{\partial C_{\mathrm{A}}}{\partial Y}\right) = -D_{\mathrm{B}}^{'}\left(\frac{\partial C_{\mathrm{B}}}{\partial Y}\right) \tag{7.13}$$

The edges of the simulation space are set at the centres of the electrodes ($X_{\min} = -\frac{1}{2}d' - 0.5$ and $X_{\max} = \frac{1}{2}d' + 0.5$) and a distance along the y axis from the electrodes known to be well outside the diffusion layer [26–28] ($Y_{\max} = 6\sqrt{D_{\max}^{'}\tau_{\max}}$) where $D_{\max}^{'}$ and $\tau_{\max}$ are the largest dimensionless diffusion coefficient in the system, and the total dimensionless time of the experiment. At the simulation edges, a zero flux condition is imposed on all species:

$$\left(\frac{\partial C_{\mathrm{i}}}{\partial X}\right)_{X_{\min},\, X_{\max},\, \text{all } Y} = 0 \tag{7.14}$$

$$\left(\frac{\partial C_{\mathrm{i}}}{\partial Y}\right)_{\text{all } X,\, Y_{\max}} = 0 \tag{7.15}$$

The value of the potential applied to the generator electrode at a given time from the start of the experiment must also be defined. If the scan starts at some potential value θ_{s}, and sweeps at a dimensionless scan rate of σ (defined in the glossary) up to a vertex potential θ_{v} before reversing and scanning back to θ_{s}, the the applied dimensionless potential θ at any given τ is:

$$\theta = \theta_{\mathrm{v}} \pm |\theta_{\mathrm{v}} - \theta_{\mathrm{s}} \pm \sigma\tau| \tag{7.16}$$

where + is used for a reduction and − for an oxidation.

These boundary conditions are summarised in Table 7.1.

Calculating the current at an IDBA

Upon the implementation of the above model, the current at both the generator and the collector electrodes must be calculated. The (dimensionless) flux at an individual generator electrode is given by integrating the flux across its width:

$$J_{\mathrm{gen}} = 2\int_{-0.5-\frac{1}{2}d}^{-\frac{1}{2}d} \left(\frac{\partial C_{\mathrm{A}}}{\partial Y}\right)_{Y=0} \mathrm{d}X \tag{7.17}$$

and at the collector:

$$J_{\mathrm{col}} = 2\int_{\frac{1}{2}d}^{0.5+\frac{1}{2}d} \left(\frac{\partial C_{\mathrm{A}}}{\partial Y}\right)_{Y=0} \mathrm{d}X \tag{7.18}$$

Note the factors of 2, these are due to using the symmetry of an interdigitated array to simulate only half of an individual generator and collector electrode. The dimensional current is then given by:

$$I = nFlmDc_{\mathrm{A}}^{*}J \tag{7.19}$$

where m is the number of generator-collector pairs.

Boundary			Condition
$\tau < 0$	All X	All Y	$C_{\mathrm{A}} = 1$, $C_{\mathrm{B}} = 0$
$\tau \geq 0$	$-0.5 - \frac{1}{2}d' < X \leq -\frac{1}{2}d'$	$Y = 0$	$\left(\frac{\partial C_{\mathrm{A}}}{\partial Y}\right) = K^0 C_{\mathrm{A}}^0 \exp\left[-\alpha\theta\right] - K^0 C_{\mathrm{B}}^0 \exp\left[(1-\alpha)\,\theta\right]$ $D_{\mathrm{B}}^{'}\left(\frac{\partial C_{\mathrm{B}}}{\partial Y}\right) = -\left(\frac{\partial C_{\mathrm{A}}}{\partial Y}\right)$
	$\frac{1}{2}d' \leq X < \frac{1}{2}d' + 0.5$		$\left(\frac{\partial C_{\mathrm{A}}}{\partial Y}\right) = -D_{\mathrm{B}}^{'}\left(\frac{\partial C_{\mathrm{B}}}{\partial Y}\right)$ $C_{\mathrm{B}} = 0$
	$-\frac{d'}{2} < X < \frac{d'}{2}$		$\frac{\partial C_{\mathrm{i}}}{\partial Y} = 0$
	$X = -0.5 - \frac{1}{2}d'$	All Y	$\frac{\partial C_{\mathrm{i}}}{\partial X} = 0$
	$X = 0.5 + \frac{1}{2}d'$		
	All X	$Y = Y_{\max}$	$\frac{\partial C_{\mathrm{i}}}{\partial Y} = 0$

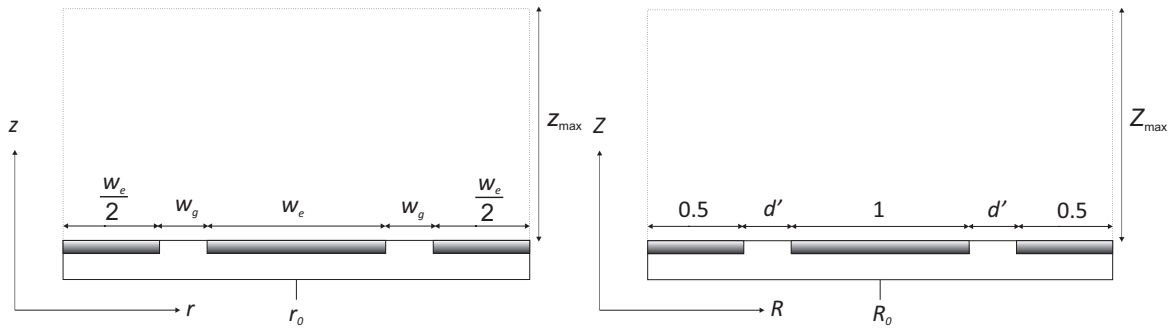
Table 7.1: Normalised boundary conditions for cyclic voltammetry simulations at an IDBA.

7.2.2 Interdigitated ring arrays

To simulate an IDRA, the model developed above must be modified to account for the added radial nature of the diffusion. The new (dimensionless) mass transport equation is:

$$\frac{\partial C_{\mathrm{i}}}{\partial \tau} = D_{\mathrm{i}}^{'}\left(\frac{\partial^2 C_{\mathrm{i}}}{\partial R^2} + \frac{1}{R}\frac{\partial C_{\mathrm{i}}}{\partial R} + \frac{\partial^2 C_{\mathrm{i}}}{\partial Z^2}\right) \tag{7.20}$$

where R is the dimensionless radial coordinate and Z is the dimensionless coordinate perpendicular to the surface of the electrodes, as defined in the Glossary. Figure 7.3(a) and



(a) Dimensional simulation space (b) Dimensionless simulation space

Figure 7.3: Schematic diagram of the two interdigitated arrays investigated in this chapter.

7.3(b) show schematically the dimensional and normalised simulation space this equation is to be solved over. The key difference between this simulation space and that used for the IDBA model (Figure 7.2) is that the whole width of the generator electrode is now included in the centre, with half of the two collector electrodes on either side. The central of the simulation space is now no longer zero, but set at a value R_0, determined by the geometry of the IDRA being simulated. Some of the symmetry that was present in the IDBA model is lost due to the radial diffusion, which will be different on different sides of the generator electrode (due to the different values of R). The edge of the simulation space is in the centre of the collector electrodes, but unlike above where this was a result of symmetry, it is now an approximation.

The boundary conditions are analogous to those used in the IDBA model, and are given in Table 7.2. The potential applied to the generator electrode, θ, varies with time and scan rate in exactly the same way as above.

Boundary			Condition
$\tau < 0$	All R	All Z	$C_{\mathrm{A}} = 1$, $C_{\mathrm{B}} = 0$
$\tau \geq 0$	$R_0 - 0.5 \leq R \leq R_0 + 0.5$	$Z = 0$	$D'_{\mathrm{A}} \left(\frac{\partial C_{\mathrm{A}}}{\partial Z}\right) = K^0 C^0_{\mathrm{A}} \exp\left[-\alpha\theta\right] - K^0 C^0_{\mathrm{B}} \exp\left[(1-\alpha)\,\theta\right]$ $D'_{\mathrm{B}} \left(\frac{\partial C_{\mathrm{B}}}{\partial Z}\right) = -D'_{\mathrm{A}} \left(\frac{\partial C_{\mathrm{A}}}{\partial Z}\right)$
	$R_0 - 0.5 - d' < R$		$D'_{\mathrm{A}} \left(\frac{\partial C_{\mathrm{A}}}{\partial Z}\right) = -D'_{\mathrm{B}} \left(\frac{\partial C_{\mathrm{B}}}{\partial Z}\right)$ $C_{\mathrm{B}} = 0$
	$R > R_0 + 0.5 + d'$		
	$-d' - 0.5 < R < -0.5$		$\frac{\partial C_{\mathrm{i}}}{\partial Z} = 0$
	$0.5 < R < 0.5 + d'$		
	$R = R_0 - 1 - d'$	All Z	$\frac{\partial C_{\mathrm{i}}}{\partial R} = 0$
	$R = R_0 + 1 + d'$		
	All R	$Z = Z_{\max}$	$\frac{\partial C_{\mathrm{i}}}{\partial Z} = 0$

Table 7.2: Normalised boundary conditions for cyclic voltammetry simulations at an IDRA.

Calculating the current at an IDRA

When calculating the current at an IDRA, it must be noted that since we are working in cyclindical coordinates, a factor of R must be included in the integrals to calculate the

overall flux. So the flux at the generator electrode is given by:

$$J_{\text{gen}} = \int_{R_0-0.5}^{R_0+0.5} \left(\frac{\partial C_{\text{A}}}{\partial Z}\right)_{Z=0} \frac{R}{R_0}\,\mathrm{d}R \tag{7.21}$$

and at the collector:

$$J_{\text{col}} = \int_{R_0-d-1}^{R_0-d-0.5} \left(\frac{\partial C_{\text{A}}}{\partial Z}\right)_{Z=0} \frac{R}{R_0}\,\mathrm{d}R + \int_{R_0+d+0.5}^{R_0+d+1} \left(\frac{\partial C_{\text{A}}}{\partial Z}\right)_{Z=0} \frac{R}{R_0}\,\mathrm{d}R \tag{7.22}$$

(the factor $\frac{1}{R_0}$ is included to normalise the response with respect to R_0 and make for easier comparison of IBDA and IDRA responses.) The dimensional current can then be obtained from the expression:

$$I = 2\pi n F w_e R_0 D c_{\text{A}}^* J \tag{7.23}$$

$$= 2\pi n F r_0 D c_{\text{A}}^* J \tag{7.24}$$

This will give the current measured at one pair of generator-collector electrodes, at radial coordinate r_0. To simulate the current measured at the entire array, many simulations must be run, each with a different value of r_0, and the results summed together.

7.2.3 Numerical methods

Methods outlined in Chapter 2 were used to discretise the mass transport equations and boundary conditions to allow them to be solved numerically. The alternating direction implicit method [30] was used, in conjunction with the Thomas algorithm [31] to efficiently solve the diagonal matrices produced, also described in Chapter 2.

The spatial grid the equations were solved over has been successfully employed pre-

viously to simulate arrays of discs [32] and hemispheres [33] In the Y direction (for an IDBA, Z for and IDRA), the first grid point is at the electrode/insulating surface, and has in inital step size of Δ. The grid then expands away from this surface in the following manner:

$$Y_{\mathrm{j}} = \gamma Y_{\mathrm{j}-1} \tag{7.25}$$

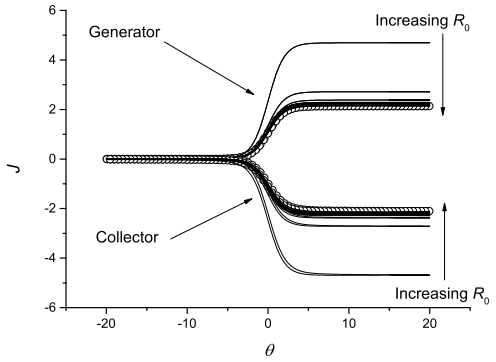
The X (for an IDBA, R for an IDRA) grid is analogous to this, with the grid expanding away from the edges of the electrodes until it meets a grid coming in the other direction (in the centre of gaps or electrodes) or until it meets the edge of the simulation space.

The temporal grid is a regular array of points. For each unit of dimensionless potential, θ, the grid is defined to have N_θ points.

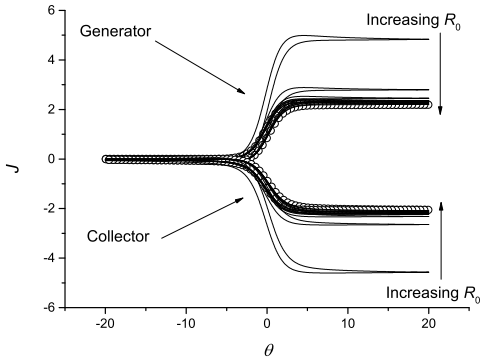
Convergence studies found the following grid parameters sufficient to produce results within 1% of a fully converged value: $\Delta = 8 \times 10^{-5}$, $\gamma = 1.125$, $N_\theta = 1 \times 10^4$. The models were coed in C++, with multithreaded parallel programming employed to increase efficiency, and run on an Intel (R) Xeon (R) 2.26 GHz PC with 2.25 GB RAM, with a typical running time of 20 mins per simulation.

7.3 Theoretical Results

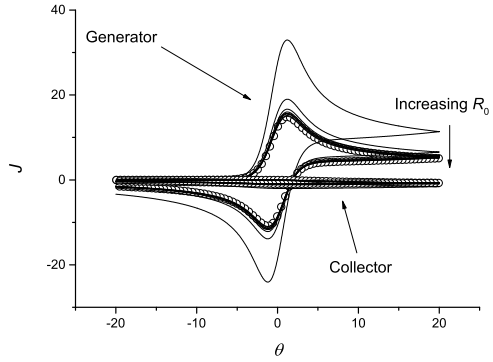
In order to compare and contrast cyclic voltammetry at IDBAs and IDRAs, simulations were carried out at both geometries. A simple, fully electrochemically reversible one electron oxidation was simulated at a generator-collector pair within an IDBA and compared to the same reaction simulated at a generator-collector pair in an IDRA with various values of R_0. The results for σ values of 0.001 (microelectrode/slow scan rate), 1 (intermediate) and 1000 (macroelectrode/fast scan rate) are shown in Figure 7.4. In all cases,



(a) $\sigma = 10^{-3}$



(b) $\sigma = 1$

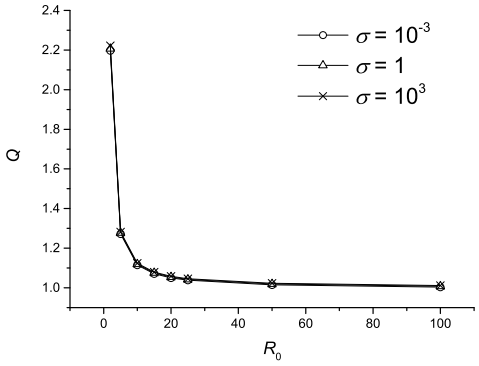


(c) $\sigma = 10^3$

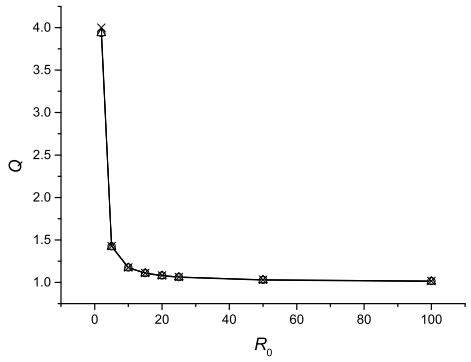
Figure 7.4: Simulated cyclic voltammograms for a one electron oxidation at a pair of electrodes in an IDBA (circles) and a pair in an IDRA at various values of R_0 (= 2, 5, 10, 15, 20, 25, 50 and 100, lines). In all cases, $D'_{\mathrm{B}} = 1$, $\alpha = 0.5$, $K^0 = 1000$. (a): $\sigma = 0.001$, (b): $\sigma = 1$ and (c): $\sigma = 1000$

d' is fixed at 0.1, $D'_{\mathrm{B}} = 1$, $\alpha = 0.5$ and $K^0 = 1000$. It is seen that for all scan rates, a smaller value of R_0 enhances the dimensionless current, due to the greater radial diffusion and more efficient mass transport. As R_0 tends to infinity, the IDRA responses converge onto the response obtained at an IDBA, since the electrodes become effectively linear. As expected, the collector electrode response becomes very small at large values of σ, since in this limit the diffusion is largely planar, so species B does not diffuse outwards towards the collector electrode.

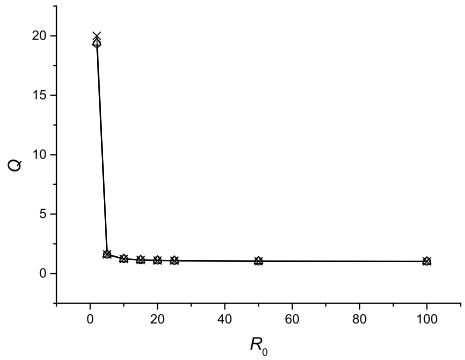
It will be useful to know how much the current at a pair of electrodes in an IDRA



(a) $d' = 0.1$



(b) $d' = 0.5$



(c) $d' = 0.9$

Figure 7.5: Values of Q for various R_0 for values of d' of (a): 0.1, (b): 0.5 and (c): 0.9. In each case, circles correspond to $\sigma = 0.001$, triangles to $\sigma = 1$ and crosses to $\sigma = 1000$. All other parameters as in Figure 7.4.

deviates from that measured at an IDBA as a function of R_0. This deviation, or current enhancement, is defined here as Q, the ratio of the peak (or steady state) generator current simulated in a IDRA simulation to that simulated at an IDBA electrode with equal d'. From Figure 7.4 it is seen that as R_0 decreases, the current enhancement ratio Q increases. Figure 7.5 shows the simulated values of Q for three values of d' (0.1, 0.5 and 0.9), each for the values of sigma (0.001, 1 and 1000). All other values remain the same as in Figure 7.4. It is seen that at small R_0, Q rapidly drops off as R_0 increases, and approaches 1 as $R_0 \to \infty$. It is also seen that, for a given value of d', the variation of Q with R_0 is

essentially independent of σ over six orders of magnitude (differences between Q values for any given R_0 is less than 1%).

Using these curves, it is then possible to calculate a value of R_0 at which Q is a specific value, for example 1.05. Any value of R_0 larger than this will then produce results at an IDRA within 5% of the reuslt for an equivalent IDBA. This value of R_0 is labled $R_{5\%}$. The value of $R_{5\%}$ for a given d' is calculated by performing six IDRA simulations with various R_0 which give values of Q between 1.04 and 1.06, and fitting a polynomial equation to the Q vs R_0 curve using the Microsoft Excel graph fitting tool (a cubic equation was found to be sufficient, higher orders produced no more accurate results). This equation can then be set equal to 1.05 and solved to give a value of $R_{5\%}$. This was done for values of d' between 0.1 and 1.0. For each d', σ values of 0.001, 1 and 1000 were used, and an avergage $R_{5\%}$ taken. The results are shown in Figure 7.6. It is seen that, for this range of d' values, $R_{5\%}$ varies linearly with d'. A line of best fit was found using Microsoft Excel to be $R_{5\%} = 22.4d' + 19.7$.

In an IDRA, the overall measured current will be dominated by the outermost electrodes, since these are largest in area. Any pair of electrodes with an R coordinate at the centre of the generator greater than $R_{5\%}$ will produce currents within 5% of those produced at an IDBA. Hence, an IDRA whose outermost electrode pair satisfies this condition is likely to be able to be simulated with reasonable accuracy as an IDBA (weighting each electrode pair's contribution according to its size).

7.4 Experimental

All experimental data in this chapter was obtained by Dr. Anna Fernández-la-Villa, Dr. Diego F. Pozo-Ayuso and Dr. Mario Castaño-Álvarez of Micrux Technologies®.

Potassium ferrocyanide ($K_4Fe(CN)_6$), potassium chloride (KCl) and nitrogen gas (N_2) were purchased from Sigma Aldrich (USA) and used as received, without purification. Solutions were prepared in deionised water of resistivity of no less than 18.2 MΩ cm at 298 K (Millipore). Solutions were thoroughly degassed by bubbling nitrogen (oxygen free) for at least 30 mins. Electrochemical experiments were carried out in a thermostated Faraday cage at 298 (± 1) K, using a PalmSens Bipotentiostat, (Palm Instruments BV, Netherlands). The platinum interdigitated ring/band working electrodes were fabricated by Micrux Technologies (Spain) using photolithography on a pyrex substrate. Platinum reference and counter electrodes are integrated by photolithography onto this substrate.

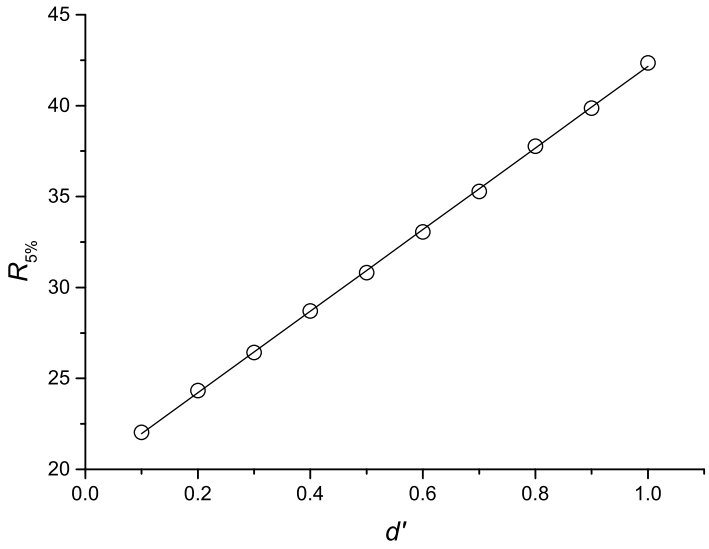


Figure 7.6: Values of $R_{5\%}$ (the value of R_0 necessary for an IDRA to produce a result within 5% of that for an IDBA) for various values of d'.

Electrode	Bands/rings	Electrode width / μm	Gap width / μm	Number of pairs
IDBA 1	Bands	10	10	15
IDBA 2	Bands	5	2	42
IDBA 3	Bands	3	2	59
IDRA 1	Rings	10	10	12
IDRA 2	Rings	5	3	30

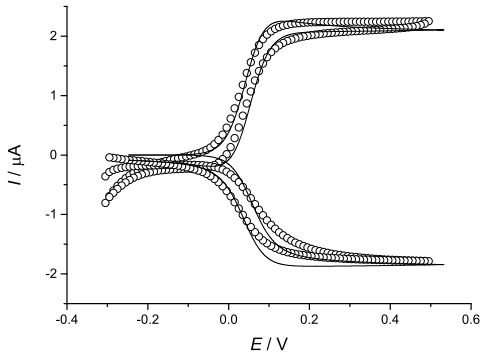
Table 7.3: Summary of geometries of electrode arrays used in this chapter. All the band electrodes are 2 mm in length.

7.5 Experimental Results

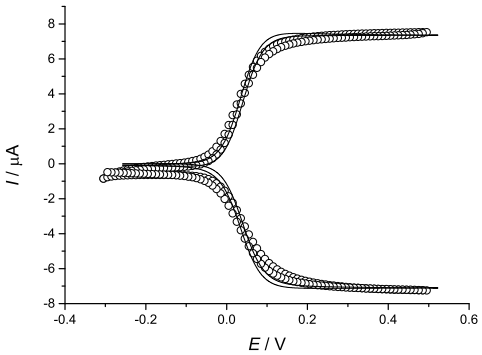
Experimental results presented in this section were obtained by Dr. Anna Fernández-la-Villa, Dr. Diego F. Pozo-Ayuso and Dr. Mario Castaño-Álvarez of Micrux Technologies®, as noted above.

7.5.1 Interdigitated band array

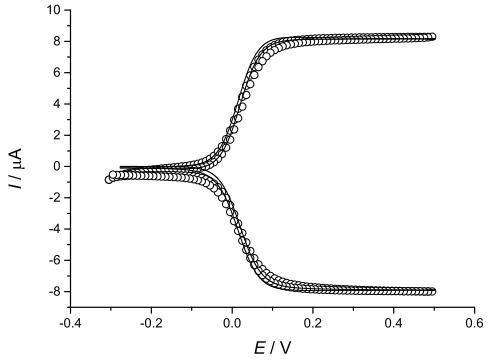
Cyclic voltammetry was carried out on aqueous 1 mM potassium ferrocyanide, $K_4Fe(CN)_6$, at a scan rate of 50 mV s^{-1} in the presence of 0.1 M KCl at three different Pt IDBA electrodes of varying geometries (summarised in Table 7.3). In all three cases the lengths of the electrodes is 2 mm. The results for IDBA1, IDBA2 and IDBA3 are shown in Figure 7.7, along with theoretical best fits. Literature values for the diffusion coefficients [34, 35] of $Fe(CN)_6^{4-}$ and $Fe(CN)_6^{3-}$ of 6.6×10^{-12} m^2 s^{-1} and 7.5×10^{-12} m^2 s^{-1} respectively were used in the simulations, with a best fit concentration determined to be 0.95 ± 0.05 mM. α and β are set at 0.5, and k^0 is arbitrarily set high at 1000 m s^{-1} to ensure complete electrochemical reversibility. Excellent fits are seen, validating the IDBA model developed above. Collection efficiencies for IDBA1, 2 and 3 at the vertex potential were measured as 79%, 96% and 96%. This is consistent with smaller inter electrode gaps (relative to the electrode widths) producing higher collection efficiencies.



(a) IDBA1



(b) IDBA2

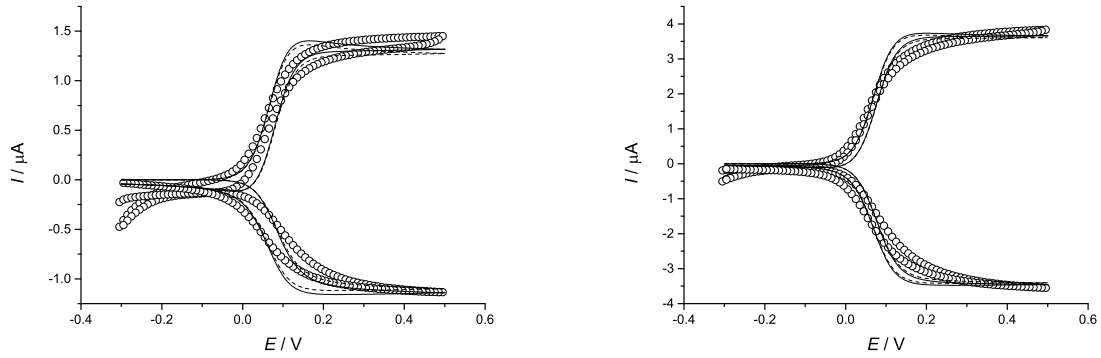


(c) IDBA3

Figure 7.7: Experimental (circles) and simulated (lines) cyclic voltammograms of 1 mM potassium ferrocyanide at IDBA 1 (a), IDBA 2 (b) and IDBA 3 (c) electrodes (see Table 7.3). In all cases the scan rate was 50 mV s^{-1}.

7.5.2 Interdigitated ring array

The cyclic voltammetry of aqueous 1 mM $K_4Fe(CN)_6$ was then repeated on two Pt IDRA electrodes (geometries summarised in Table 7.3), again at a scan rate of 50 mV s^{-1}, in the presence of 0.1 M KCl. The experiments were simulated using the full IDRA model outlined above, and using the IDBA model with each pair of generator-collector electrodes having an area equal to each of the generator electrodes in the IDRAs. The results are shown in Figure 7.8. Collection efficiencies at the potential vertex were measured as 78% and 92% for IDRA1 and 2 respectively, again reflective of the smaller gap size in IDRA2.



(a) IDRA1 (b) IDRA2

Figure 7.8: Cyclic voltammograms of 1 mM potassium ferrocyanide at IDRA 1 (a) and IDRA 2 (b) electrodes (see Table 7.3). In all cases the scan rate was 50 mV s^{-1}. Circles: Experimental data, solid lines: Simulations using the full IDRA model, dashed lines: Simulations approximating the rings as bands.

For the simulations, the same literature diffusion coefficients as above were used, and in both cases the concentration of $K_4Fe(CN)_6$ was fixed at 1 mM. It is seen that the two models produce very similar results, which both fit well with the experimental data, with differences likely being due to capacitative effects. The experimentally measured currents are dominated by the larger, more peripheral rings, which have small enough curvature for radial diffusion to be negligible on these timescales. For IDRA1, the outermost electrode pair has an R_0 value of 46. The equation for $R_{5\%}$ developed above gives an $R_{5\%}$ value of 42.16 for $d' = 1.0$, meaning this outer electrode pair can be reasonably well modelled as bands. For IDRA2, the outer electrode pair has $R_0 = 94.3$, well above the $R_{5\%}$ value of 33.18 for this geometry. This allows us to model these IDRAs using the computationally more simplistic IDBA model.

7.6 Conclusions

In this chapter, interdigitated band and ring electrodes were simulated and theoretical results compared. It was found that if a generator-collector pair of electrodes in a ring array has a large enough radius, the pair can be approximated as a pair of parallel linear bands. An equation has been developed for what radius this pair in a ring array needs to be to produce a result within 5% of that at parallel bands: $R_0 \geq 22.4d' + 19.7$ in the range $0.1 \leq d' \leq 1.0$. This was found to be independant of the scan rate used. The models for interdigitated bands and rings were used to simulate experimental data for the oxidation of $Fe(CN)_6^{4-}$, and found to give good fits. It was also shown that if the inequality given above is satisfied for the outermost pair of electrodes in a ring array, then the array can be effectively modelled using the more simplistic interdigitated band array model.

References

[1] Barnes, E. O.; Fernández-la Villa, A.; Pozo-Ayuso, D. F.; Castaño Alvarez, M.; Lewis, G. E. M.; Dale, S. E. C.; Marken, F.; Compton, R. G. *J. Electroanal. Chem.* **2013**, *709*, 57 – 64.

[2] Ordeig, O.; del Campo, J.; Xavier Muñoz, F.; Banks, C. E.; Compton, R. G. *Electroanalysis* **2007**, *19*, 1973 – 1986.

[3] Herzog, G.; Beni, V. *Anal. Chim. Acta* **2013**, *769*, 10 – 21.

[4] Fletcher, S.; Horne, M. D. *Electrochem. Commun.* **1999**, *1*, 502 – 512.

[5] Tomčík, P.; Jursa, S.; Mesároš, v.; Bustin, D. *J. Electroanal. Chem.* **1997**, *423*, 115 – 118.

[6] Sanderson, D. G.; Anderson, L. B. *Anal. Chem.* **1985**, *57*, 2388 – 2393.

[7] Jenčušová, P.; Tomčík, P.; Bustin, D.; Rievaj, M.; Dovalovská, Z. *Chem. Pap.* **2006**, *60*, 173 – 178.

[8] Aoki, K.; Morita, M.; Niwa, O.; Tabei, H. *J. Electroanal. Chem.* **1988**, *256*, 269 – 282.

[9] Aoki, K.; Tanaka, M. *J. Electroanal. Chem.* **1989**, *266*, 11 – 20.

[10] Strutwolf, J.; Williams, D. E. *Electroanalysis* **2005**, *17*, 169 – 177.

[11] Barnes, E. O.; Lewis, G. E. M.; Dale, S. E. C.; Marken, F.; Compton, R. G. *Analyst* **2012**, *137*, 1068 – 1081.

[12] Rajantie, H.; Strutwolf, J.; Williams, D. E. *J. Electroanal. Chem.* **2001**, *500*, 108 – 120.

[13] Rajantie, H.; Williams, D. E. *Analyst* **2001**, *126*, 1882 – 1887.

[14] French, R. W.; Chan, Y.; Bulman-Page, P. C.; Marken, F. *Electrophoresis* **2009**, *30*, 3361 – 3365.

[15] Nekrasov, L. N.; Khrushcheva, E. I. *Elektrokhimiya* **1967**, *3*, 166 – 172.

[16] Damjanovic, A.; Genshaw, A. M. A.; Bockris, J. O. *J. Electrochem. Soc.* **1967**, *114*, 1107 – 1112.

[17] Unwin, P. R. *J. Electroanal. Chem.* **1991**, *297*, 103 – 124.

[18] Bruckenstein, S.; Miller, B. *Acc. Chem. Res.* **1977**, *10*, 54 – 61.

[19] Albery, W. J.; Bruckenstein, S. *Trans. Faraday Soc.* **1966**, *62*, 1946 – 1954.

[20] Albery, W. J.; Bruckenstein, S. *Trans. Faraday Soc.* **1966**, *62*, 2584 – 2595.

[21] Dale, S. E. C.; Vuorema, A.; Ashmore, E. M. Y.; Kasprzyk-Horden, B.; Sillanpää, M.; Denuault, G.; Marken, F. *Chem. Rec.* **2012**, *12*, 143 – 148.

[22] Zhu, F.; Yan, J.; Lu, M.; Zhou, Y.; Yang, Y.; Mao, B. *Electrochim. Acta* **2011**, *56*, 8101 – 8107.

[23] Barnes, E. O.; Lewis, G. E. M.; Dale, S. E. C.; Marken, F.; Compton, R. G. *J. Electroanal. Chem.* **2013**, *703*, 38 – 44.

[24] Niwa, O.; Morita, M.; Tabei, H. *Anal. Chem.* **1990**, *62*, 447 – 452.

[25] Niwa, O.; Morita, M. *Anal. Chem.* **1996**, *68*, 355 – 359.

[26] Gavaghan, D. J. *J. Electroanal. Chem.* **1998**, *456*, 1 – 12.

[27] Gavaghan, D. J. *J. Electroanal. Chem.* **1998**, *456*, 13 – 23.

[28] Gavaghan, D. J. *J. Electroanal. Chem.* **1998**, *456*, 25 – 35.

[29] Crank, J.; Nicolson, E. *Proc. Camb. Phil. Soc.* **1947**, *43*, 50 – 67.

[30] Press, W. H., Teukolsky, S. A., Vetterling, W. T., Flannery, B. P., Eds. *Numerical Recipes: The Art of Scientific Computing*; Cambridge University Press, 2007.

[31] Compton, R. G.; Pilkington, M. B. G.; Stearn, G. M. *J. Chem. Soc., Faraday Trans. 1* **1988**, *84*, 2155 – 2171.

[32] Ordeig, O.; Banks, C. E.; Javier del Campo, F.; Munoz, X.; Davis, J.; Compton, R. G. *Electroanalysis* **2006**, *18*, 247 – 252.

[33] Ward, K. R.; Lawrence, N. S.; Hartshorne, R. S.; Compton, R. G. *J. Phys. Chem. C* **2011**, *115*, 11204 – 11215.

[34] Klymenko, O. V.; Evans, R. G.; Hardacre, C.; Svir, I. B.; Compton, R. G. *J. Electroanal. Chem.* **2004**, *571*, 211 – 221.

[35] Adams, R. N. *Electrochemistry at Solid Electrodes*; Marcel Dekker, New York, 1969.

Chapter 8

Voltammetry at porous electrodes

In this chapter, a model is developed to simulate both chronoamperometry and cyclic voltammetry at porous electrodes fabricated by means of electro-deposition around spherical templates. A theoretical method to extract electrochemical rate constants for quasi-reversible and irreversible systems is proposed by the approximation of decoupling of the diffusion within the porous electrode and of bulk diffusion to the electrode surface. This work, carried out in collaboration with Prof X. Chen of Nanjing Tech University, China and Mr. P. Li of Oxford University has been published in *The Journal of Electroanalytical Chemistry* [1].

8.1 Introduction

The use of porous electrodes for electroanalytical measurements is growing because of the scope for altered voltammetric responses which may, under favourable circumstances, offer a more sensitive response and at a lower over-potential than conventional macro-electrodes where mass transport occurs via semi-infinite diffusion. Such electrodes are often made by using as a template layers of spheres, for example made of polystyrene, on the surface of a pre-existing macroelectrode. Metal, very often gold, is then electroplated

around the spheres before the latter are removed, for example via dissolution in a suitable solvent. The created porous structure can then, in an idealised sense, be thought of as a three dimensional network of hollow metal spherical holes interconnected via tiny ducts which allow hole to hole transport and which are likely formed at the points of contact between the original templating spheres. Table 8.1 shows recent examples of the use of porous electrodes fabricated in this manner in electrochemical sensing, where both improved sensitivity and limits of detection are often claimed. These include the detection of species such as NADH [2–4], glucose [5–7], nitrobenzene [8] and hydrogen peroxide [9], in addition to a number of immunosensors [10–12].

The purpose of this chapter is to develop theory for porous electrodes constructed with the method described above and summarised in Figure 8.1. In particular we seek to identify the contributions to the voltammetric and chronoamperometric signals resulting from material diffusing to the top of the surface of the electrode from bulk solution and from material within the spherical holes of the porous structure. Qualitatively we anticipate that the latter will give rise, under suitable timescales, to a "thin layer" type response and that this can lead to a smaller overpotential required to drive electron transfer. If a mixture of analytes in solution have similar formal potentials under bulk diffusion conditions alone, the additional thin layer element may be used to discriminate between them if they enter the porous layer to differing extents [15–17].

In the following we employ a "decoupling" of the two modes of transport, diffusion to the electrode surface and transport within the porous layer, which has been shown experimentally to be the case for porous electrodes fabricated using drop casting of carbon nanotubes [18].

Porous material	Hollow void radius	Target species	Reference
Gold	320 nm	NADH	[2]
Gold	550 nm	NADH	[3]
Ruthenium oxide	150 nm	NADH	[4]
Gold	125 nm	Glucose	[5]
Polyaniline/Prussian Blue	250 nm	Glucose	[6]
Ionic liquid doped poly(*N*[3-(trimethyoxy-silyl)propyl]aniline)	250 nm	Glucose	[7]
Platinum nanoparticle modified carbon	55 nm	Nitrobenzene	[8]
Gold nanoparticle doped titanium dioxide with immobilised haemoglobin	250 nm	Hydrogen peroxide	[9]
Gold	250 nm	C-reactive protein[1]	[10]
Ionic liquid doped polyanailine	125 nm	Hepatitis B surface antigen	[11]
Gold	125 nm	Human Apolipoprotein B-100[2]	[12]

Table 8.1: Composition and uses of porous electrodes. [1]A human protein which is an indicator for inflammation [13]. [2]A human protein which is an indicator for coronary artery disease [14].

8.2 Theory

Electrochemistry at a porous electrode is simulated. A simple, single electron transfer is considered:

$$\mathrm{A} \pm \mathrm{e}^- \rightleftharpoons \mathrm{B} \tag{8.1}$$

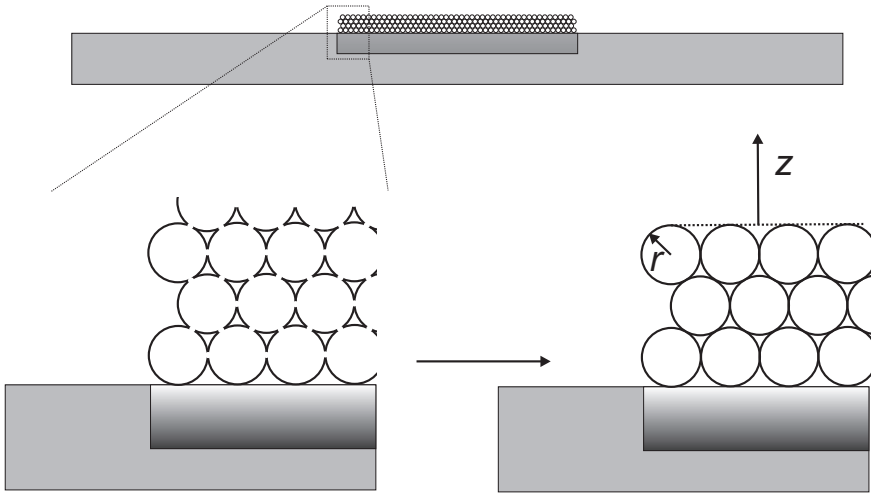


Figure 8.1: Schematic cross section of a porous electrode consisting of a series of hollow spheres supported on a disc electrode (the size of spheres relative to the disc electrode is greatly exaggerated). Also shown is a zoomed in section of the electrode, highlighting the interconnected nature of the spheres, and a depiction of the model used to simulate electrochemistry at the electrode.

The transfer is assumed to take place in solution with a large amount of inert supporting electrolyte to ensure that mass transport is diffusion only.

The porous electrode is considered to be a series of interconnected spherical voids within a conductive material. These electrodes may be fabricated by supporting a series of nanosized polystyrene spheres on a macroelectrode surface, and surrounding them with a layer of, for example, electro-deposited gold. The spheres are then dissolved away, leaving behind a network of interconnected holes, through which solution containing the analyte of interest may permeate. For simplicity, and to generate an idealised structure amenable to theoretical modelling, we assume the porous layer comprises hollow spheres formed from where the polystyrene were dissolved and tiny pores of negligible size linking adjacent spheres. This allows the entire porous layer to be flooded with electrolyte when immersed in a solution. This is shown schematically in Figure 8.1, which shows a view of the spheres supported on an electrode (a), and a zoomed in view of the porous, interconnected hollow

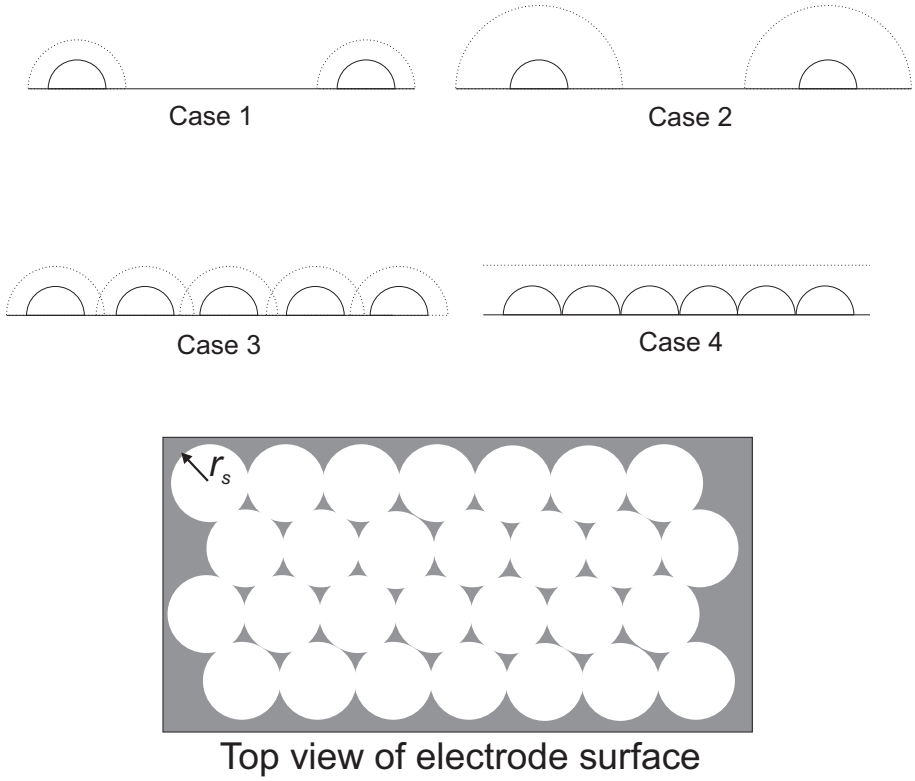


Figure 8.2: Schematic diagram of the four cases for electrochemical responses at a micro- (or nano-) electrode array, and a top view of a porous electrode surface, showing the close packing of hemispherical hollows.

sphere structures (b). In this study, the electrode is modelled as a series of identical, hollow, independent conductive spheres (Figure 8.1 (c)). After the start of an experiment, it is assumed that negligible diffusion occurs either from sphere to sphere or between the spheres and the bulk. If the spheres are small enough relative the the radius of the disc they are supported on, then the top of the layer(s) of spheres can be considered a disc electrode. The reasons for this latter simplification are discussed next.

The electrochemical behaviour of flat micro- (and nano-) electrode arrays can be divided into four distinct cases [19–25], as summarised in Figure 8.2. In case 1, the timescale is short enough so that the diffusion layers are independent and do not overlap. This leads to linear diffusion and a Cottrellian response from the array as a whole. In case 2, the timescale is longer, and while the electrodes still have independent diffusion layers, these

layers are now large compared to the electrodes, and convergent diffusion occurs. The response can be considered to be that of several independent micro electrodes. In case 3, the diffusion layers become comparable in size to the electrode separation, and begin to overlap. In case 4, the diffusion layers are very large compared to the electrodes and the distance between them. The diffusion layers merge into a single diffusion layer, and the array behaves as a single, much larger electrode, and Cottrellian (planar diffusion) behaviour is again observed. By considering the top layer of spheres to behave as a case 4 array, it may be modelled as a macroelectrode. This will be valid provided at least several layers of spheres are used in the electrode construction and that $\sqrt{Dt} > r_s$, where t is the timescale of the experiment, D is the diffusion coefficient of the species interest and r_s is the radius of the sphere.

Further to this assumption of modelling the top layer of spheres as a case 4 electrode array, we also assume that diffusion inside the hollow spheres is completely decoupled from the diffusion down to the top layer of spheres. We also assume that no diffusion occurs between individual spheres. This allows us to simulate the response inside a single sphere and and the response at a disc electrode. The single sphere result can be multiplied by the number of spheres present, and added to the disc response from the exposed top layer of spheres to give an overall response. This model is used to simulate two electrochemical experiments: potential step chronoamperometry and cyclic voltammetry, which are now discussed in turn.

8.2.1 Simulation of chronoamperometry within a single sphere

In a potential step chronoamperometric experiment, the potential applied to the electrode is stepped from a value where no electron transfer takes place, to a value where electron

transfer occurs at a rate dictated by the mass transport of the chemical species to the electrode surface. The spherically symmetric environment inside a sphere can be reduced to a one dimensional system. The dependence of concentration of any species on time is given by Fick's second law in spherically symmetric space, which is given in dimensionless parameters by:

$$\frac{\partial C_{\mathrm{i}}}{\partial \tau} = D_{\mathrm{i}}^{'} \left(\frac{\partial^2 C_{\mathrm{i}}}{\partial R^2} + \frac{2}{R} \frac{\partial C_{\mathrm{i}}}{\partial R} \right) \tag{8.2}$$

All dimensionless parameters are defined in the Glossary. Initial conditions are:

$$\tau = 0, \text{ all } R; \; C_{\mathrm{A}} = 1 \tag{8.3}$$

Note that for single step chronoamperometry, species B need not be considered.

At time $\tau = 0$, the start of the experiment, the electrode potential is stepped, and the boundary condition at the electrode surface becomes:

$$\tau \geq 0, \; R = R_{\mathrm{s}}; \; C_{\mathrm{A}} = 0 \tag{8.4}$$

At the centre of the sphere, a zero flux boundary condition is imposed as a result of symmetry:

$$\tau \geq 0, \; R = 0; \; \frac{\partial C_{\mathrm{A}}}{\partial R} = 0 \tag{8.5}$$

Table 8.2 summarises these boundary conditions.

The dimensionless flux at the sphere surface is then given by:

$$J_{\mathrm{s}} = - \left(\frac{\partial C_{\mathrm{A}}}{\partial R} \right)_{R=1} \tag{8.6}$$

Boundary		Chronoamperometry Condition	Cyclic Voltammetry Condition
$\tau < 0$	All R	$C_{\mathrm{A}} = 1$ $C_{\mathrm{B}} = 0$	
$\tau \geq 0$	$R = 1$	$C_{\mathrm{A}} = 0$ $D'_{\mathrm{B}} \frac{\partial C_{\mathrm{B}}}{\partial R} = -\frac{\partial C_{\mathrm{A}}}{\partial R}$	$-\frac{\partial C_{\mathrm{A}}}{\partial R} = K^0 \left[C^0_{\mathrm{A}} \mathrm{e}^{-\alpha\theta} - C^0_{\mathrm{B}} \mathrm{e}^{(1-\alpha)\theta} \right]$ $D'_{\mathrm{B}} \frac{\partial C_{\mathrm{B}}}{\partial R} = -\frac{\partial C_{\mathrm{A}}}{\partial R}$
	$R = 0$	$\frac{\partial C_{\mathrm{A}}}{\partial R} = 0$	

Table 8.2: Normalised boundary conditions to simulate chornoamperometry and cyclic voltammetry at a hollow sphere electrode.

8.2.2 Simulation of cyclic voltammetry within a single sphere

The only change that need be made to the above model to instead simulate cyclic voltammetry inside a sphere is the electrode surface boundary condition, where Butler-Volmer kinetics are instead employed. Using Butler-Volmer kinetics introduced in Chapter 1, the flux at the electrode surface is given in dimensionless parameters by:

$$-\left(\frac{\partial C_{\mathrm{A}}}{\partial R}\right)_{R=1} = K^0 C^0_{\mathrm{A}} \left(\exp\left[-\alpha\theta\right] - C^0_{\mathrm{B}} \exp\left[\left(1-\alpha\right)\theta\right]\right) \tag{8.7}$$

Conservation of mass results in equal fluxes of species A and B:

$$D'_{\mathrm{B}} \frac{\partial C_{\mathrm{B}}}{\partial R} = -\frac{\partial C_{\mathrm{A}}}{\partial R} \tag{8.8}$$

These boundary conditions are again summarised in Table 8.2. The dimensionless flux is calculated the same as for chronoamperometry.

8.2.3 Simulation of chronoamperometry and cyclic voltammetry at a disc electrode

Chronoamperometry at a disc electrode is well characterised and may be calculated using the Shoup and Szabo equation [26–28]. In our model of the porous electrode by hypothesis we decouple the current response from the interior of the spheres from that of the overall "disc". Thus there are two electrode radii (that of a sphere and that of the disc), which without due care will complicate the analysis of theoretical results in terms of dimensionless parameters. We therefore use the radius of the spheres as the basis for our set of dimensionless parameters. A dimensionless disc radius, R_{d}, must then be defined as:

$$R_{\mathrm{d}} = \frac{r_{\mathrm{d}}}{r_{\mathrm{s}}} \tag{8.9}$$

The Shoup-Szabo equation can then be expressed:

$$J_{\mathrm{d}} = \frac{R_{\mathrm{d}}}{\pi}\left(0.7854 + 0.4432\left(\frac{\tau}{R_{\mathrm{d}}^2}\right)^{-0.5} + 0.2145\,\exp\left[-0.3912\left(\frac{\tau}{R_{\mathrm{d}}^2}\right)^{-0.5}\right]\right) \tag{8.10}$$

Simulation methods for cyclic voltammetry at a macrodisc electrode have been well established. The relevant mass transport equation is:

$$\frac{\partial C_{\mathrm{i}}}{\partial \tau} = D_{\mathrm{i}}^{'}\left(\frac{\partial^2 C_{\mathrm{i}}}{\partial Z^2}\right) \tag{8.11}$$

Butler-Volmer kinetics are again used as the electrode surface boundary condition, now applied at $Z = 0$ rather than $R = 1$. The zero flux bulk solution boundary condition is applied at $Z_{\max} = 6\sqrt{D_{\max}^{'}\tau_{\max}}$, where $D_{\max}^{'}$ is the largest (dimensionless) diffusion coef-

ficient in the system and $\tau_{\max}$ is the total dimensionless time taken to run the experiment. This position has been shown to be well outside the diffusion layer [29–31]. Dimensionless boundary conditions, and the boundaries at which they apply, for a macrodisc are shown in Table 8.3.

The dimensionless flux at the disc, J_{d}, is given by:

$$J_{\mathrm{d}} = \frac{R_d}{4}\left(\frac{\partial C_{\mathrm{A}}}{\partial Z}\right)_{Z=0} \tag{8.12}$$

8.2.4 Total current at a porous electrode

We assume the electrochemical response at a porous electrode is the sum of the responses inside the hollow spheres (modeling the pores) and the disc like response from diffusion to the top layer of spheres. If there is negligible diffusion between individual spheres and

Boundary		Cyclic Voltammetry Condition
$\tau < 0$	All Z	$C_{\mathrm{A}} = 1$ $C_{\mathrm{B}} = 1$
$\tau \geq 0$	$Z = 0$	$\frac{\partial C_{\mathrm{A}}}{\partial Z} = K^0\left[C^0_{\mathrm{A}}\mathrm{e}^{-\alpha\theta} - C^0_{\mathrm{B}}\mathrm{e}^{(1-\alpha)\theta}\right]$ $D'_{\mathrm{B}}\frac{\partial C_{\mathrm{B}}}{\partial Z} = -\frac{\partial C_{\mathrm{A}}}{\partial Z}$
	$Z = Z_{\max}$	$\frac{\partial C_{\mathrm{i}}}{\partial Z} = 0$

Table 8.3: Normalised boundary conditions to simulate cyclic voltammetry at a macrodisc electrode

the bulk during electrolysis, then the overall current will be the sum of the two responses:

$$I = I_{\mathrm{s}} + I_{\mathrm{d}} \tag{8.13}$$

where I_{s} and I_{d} are the currents from the spheres and the "disc" respectively. Defining the total number of spheres as N_{s}, then in dimensionless terms:

$$J = N_{\mathrm{s}} J_{\mathrm{s}} + J_{\mathrm{d}} \tag{8.14}$$

8.2.5 Numerical Methods

Numerical simulation of chronoamperometry and cyclic voltammetry necessitates the discretisation of the mass transport equations and boundary conditions in space and time, using the methods outlined in Chapter 2. The equations are then solved simultaneously and implicitly over all space using the Thomas algorithm [32] to solve the large banded matrices produced, again outlined in Chapter 2.

Appropriate spatial and temporal grids must be defined to discretise and solve the equations over. For chronoamperometry, the temporal grid consists of a dense, regular mesh of points from $\tau = 0$ up to some switching value, τ_s. After this value, the temporal grid expands and becomes less dense. Mathematically:

$$\tau_0 = 0 \tag{8.15}$$

$$\tau \leq \tau_s\text{:} \quad \tau_k = \tau_{k-1} + \Delta_\tau \tag{8.16}$$

$$\tau > \tau_s\text{:} \quad \tau_k = \tau_{k-1} + \gamma_\tau \left(\tau_{k-1} - \tau_{k-2}\right) \tag{8.17}$$

For cyclic voltammetry, the temporal grid is defined in terms of the dimensionless potential. Each unit of θ is divided into N_θ evenly spaced points. The temporal grid then defined to be:

$$\tau_k = \tau_{k-1} + \frac{1}{N_\theta \sigma} \tag{8.18}$$

For the spatial grid inside a sphere (for both chronoamperometry and cyclic voltammetry), the grid expands away from the electrode surface at $R = 1$ after an initial step of Δ_R. Mathematically:

$$R_0 = 1 \tag{8.19}$$

$$R_1 = 1 - \Delta_R \tag{8.20}$$

$$R_j = R_{j-1} - \gamma_R \left(R_{j-2} - R_{j-1}\right) \tag{8.21}$$

The final R point is defined as zero, the centre of the sphere.

For a macrodisc, a similar grid is used, with an initial step size of Δ_Z from zero, and then expanding out to bulk solution:

$$Z_0 = 0 \tag{8.22}$$

$$Z_1 = \Delta_Z \tag{8.23}$$

$$Z_j = Z_{j-1} + \gamma_R \left(Z_{j-1} - Z_{j-2}\right) \tag{8.24}$$

Convergence studies found the following grid parameters sufficient to ensure simulated results were within 0.2% of fully converged outcomes: $\Delta_\tau = 1 \times 10^{-9}$, $\tau_s = 1 \times 10^{-5}$, $\gamma_\tau = 1.0001$, $N_\theta = 100$, $\Delta_R = \Delta_Z = 1 \times 10^{-5}$, $\gamma_R = \gamma_Z = 1.01$. Typical run times were of

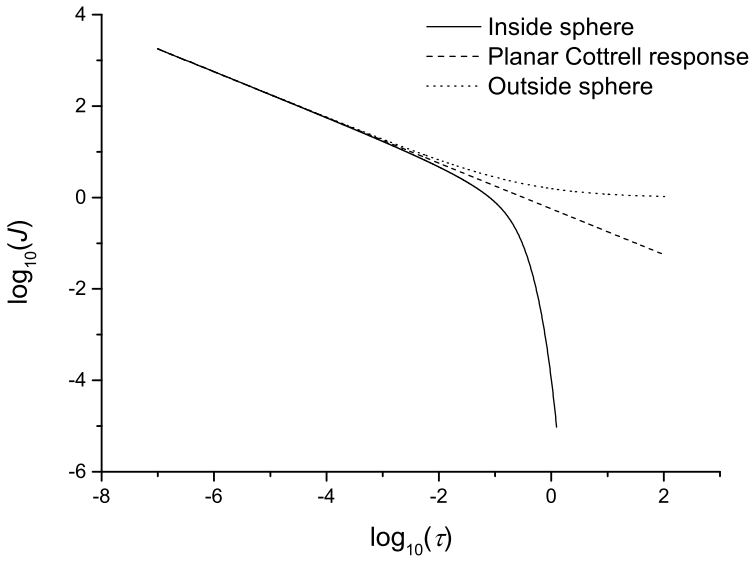


Figure 8.3: Chronoamperometric responses (in dimensionless parameters) of the inside of a sphere (solid line), a macrodisc (dashed line) and the outside of a sphere (dotted line).

the order 5 to 10 seconds per simulation. The models were programmed in C++ and all simulations carried out on an Intel(R) Xenon(R) 2.26 GHz PC with 2.25 GB RAM.

8.3 Simulated results and discussion

8.3.1 Chronoamperometry

If we consider the chronoamperometric response inside the spherical holes of a porous electrode to be completely decoupled from that outside, then the total response will be a mixture of two kinds of diffusion; that occurring inside the spherical voids and that occurring at the "disc like" surface of the top layer of spheres shown schematically in Figure 8.1. Note that the number of layers of spheres supported on the disc electrode is arbitrary, subject to fulfilling the assumption identified above. The important parameter is the number of spheres, N_{s}.

To understand these types of diffusion, chronoamperometric responses due to each kind are calculated and compared. Chronoamperometry is simulated inside a hollow sphere using the model outlined above, giving the dimensionless result shown by the solid line in Figure 8.3 (which shows dimensionless flux against dimensionless time in a log-log plot). This result is compared to known analytical results for an isolated planar macrodisc electrode, given by the Cottrell equation [33]:

$$I_{\mathrm{d}} = \frac{nFAc\sqrt{D}}{\sqrt{\pi t}} \tag{8.25}$$

which in the dimensionless form becomes:

$$J_{\mathrm{d}} = \frac{1}{\sqrt{\pi\tau}} \tag{8.26}$$

This is shown as a dashed line in Figure 8.3. For comparison, the analytical equation for the chronoamperometric response *outside* an isolated sphere is given by [34]:

$$I_{\mathrm{s}'} = nFAc\left(\sqrt{\frac{D}{\pi t}} + \frac{1}{r_e}\right) \tag{8.27}$$

(where s' denotes the response outside of a sphere), given in dimensionless parameters by:

$$J_{\mathrm{s}'} = \frac{1}{\sqrt{\pi\tau}} + 1 \tag{8.28}$$

This is shown as a dotted line in Figure 8.3. At small values of τ, all three cases show linearity in the log-log plot, corresponding to planar diffusion very close to the surface. In this limit, the diffusion is blind to the large scale shape of the electrode. As τ increases,

however, differences become apparent. The response inside the sphere starts to drop off rapidly, as all the material inside the sphere is used up. This is in stark contrast to the well known response outside a sphere, which reaches a limiting steady state current due to efficient spherical diffusion. The "infinite" Cottrellian macrodisc response continues to be linear, and decreases steadily to zero.

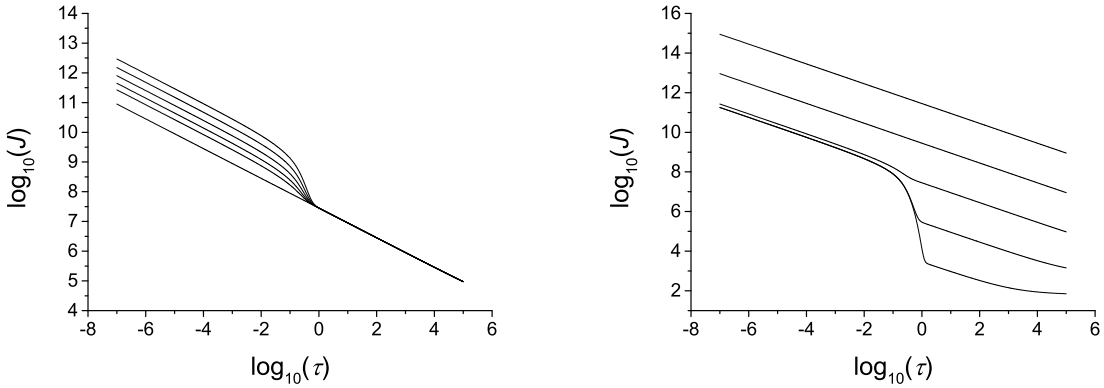
By modelling a porous electrode as being the sum of a large number of hollow spheres and the overall disc, we can approximate the chronoamperometric response of the porous electrode. The contribution of the spheres is obtained *via* simulation. The exposed surface of the top layer of spheres can be considered as a disc in which the conductive gold deposited around the upper most layer of spheres is sufficient to generate case 4 like behavior so that the porous electrode surface behaves like macrodisc. The basis for this is provided by extensive previous simulations which show that only a tiny amount of active surface is required to achieve diffusion control to the entire geometric disc surface [19–25]. Since

$$d \ll r_s \ll r_d \tag{8.29}$$

(where d is the separation between spheres) the diffusion layers around each top layer pore will overlap to a large extent and form a single, large diffusion layer. The contribution of the disc can be therefore obtained *via* the Shoup and Szabo equation, as outlined in Section 8.2.3.

$$J_{\mathrm{d}} = \frac{R_{\mathrm{d}}}{\pi}\left(0.7854 + 0.4432\left(\frac{\tau}{R_d^2}\right)^{-0.5} + 0.2146\,\exp\left[-0.3912\left(\frac{\tau}{R_d^2}\right)^{-0.5}\right]\right) \tag{8.30}$$

At any given time, the total dimensionless flux density will then by the sum of the flux from the (micro)disc given by Equation 8.30, $J_{\mathrm{d}'}$ and the simulated flux from the spheres,



(a) Vary the number of spheres (b) Vary the radius of the disc

Figure 8.4: (a) Dimensionless chronoamperometric responses of a macrodisc of radius $R_{\mathrm{d}} = 10^4$ with number of hollow spheres N_{s} from bottom to top of 0, 1, 2, 4, 8 and 16 $\times 10^8$ (b) Dimensionless chronoamperometric responses for 10^8 spheres of a macrodisc of various radius R_{d} of, from bottom to top, 10^2, 10^3, 10^4, 10^5 and 10^6.

J_{s}, multiplied by the number of spheres, N_{s}:

$$J = J_{\mathrm{d}'} + N_{\mathrm{s}} J_{\mathrm{s}} \tag{8.31}$$

Figure 8.4(a) shows the calculated chronoamperometric responses for various numbers of hollow spheres on a disc electrode of radius $R_d = 10^4$. The bottom most line represents Equation 8.30, and gives the response for the case with no spheres on the surface. The other lines, from bottom to top, have 1, 2, 4, 8 and 16 $\times 10^8$ spheres respectively. It is seen that, the more spheres there are, the greater the deviation from the Shoup and Szabo case at small τ values. In all cases however, by the time τ has reached 1, the contribution from the spheres is insignificant, since all the material inside them has been used up, and only the "disc" response remains.

The response inside the spheres can be expected to have a more significant contribution to the overall current if the experiment is carried out in an ionic liquid (rather than in

conventional solvents) due to the drastically lowered diffusion coefficients. For a typical sphere radius of 250 nm [6, 10, 35], and diffusion coefficient in an ionic liquid of 10^{-11} m^2 s^{-1}, this means the contribution from the spheres will not be seen after roughly 5 milliseconds, making it difficult to observe experimentally as it will be masked by double layer charging. Conversely, for aqueous systems, a typical diffusion coefficient would be of the order 10^{-9} m^2 s^{-1}, meaning the signal from inside the spheres is lost after roughly 10 μs, and will certainly not be observed using conventional chronoamperometry.

Figure 8.4(b) shows calculated chronoamperometric responses this time for a fixed number of spheres (10^8), but varying R_d from 10^2 (bottom most line), 10^3, 10^4, 10^5 to 10^6, (top most line). For the smallest disc, the overall response is initially dominated by the spheres. Around $\tau = 1$ the response from the spheres dies away as all the material in them is used up. This just leaves the disc response, which eventually reaches a steady state value (due to the small size of the disc). For the largest disc, it is seen that the log-log plot of the response is linear at all times. The current from inside the spheres is swamped by the large disc response and is not seen. The large size of the disc also means that steady state is not reached in this timescale, and a Cottrellian response is all that is seen.

8.3.2 Cyclic voltammetry

Cyclic voltammetry measured inside a sphere will vary greatly in character depending on the scan rate used. At low scan rates (or small spheres) all of the electroactive species inside the sphere will be consumed, leading to a "thin layer" response. At high scan rates (or large spheres) the depletion layer cannot extend very far into the interior of the sphere, leading to a "diffusional" response. This is seen qualitatively in Figure 8.5 which

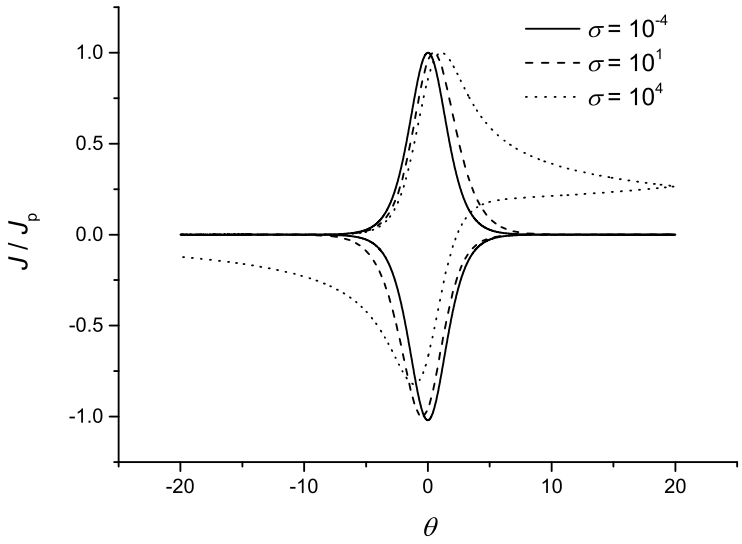
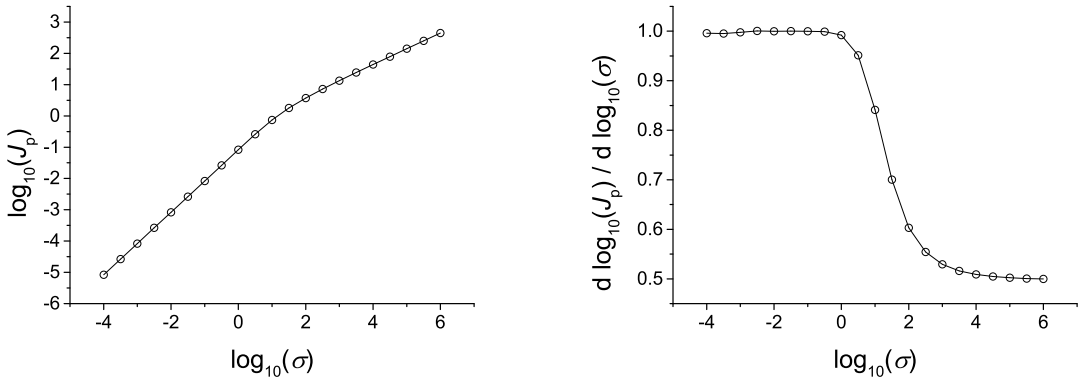


Figure 8.5: Normalised simulated cyclic voltammetric responses from inside hollow spheres at dimensionless scan rates of 10^{-4} (solid line), 10^{1} (dashed line) and 10^{4} (dotted line). K^0 is fixed at 10^5.

shows simulated cyclic voltammograms with σ values of 10^{-4}, 10^{1} and 10^{4} (normalised to a peak height of one). A clear transition is seen from a thin layer response, through an intermediate case to a diffusional response.

This behaviour is confirmed with a plot of $\log_{10}(J_\mathrm{p})$ (peak dimensionless flux) against $\log_{10}(\sigma)$. For a surface bound/thin layer response, the peak height is directly proportional to the scan rate. For a diffusional response, the peak hight is proportional to the square root of the scan rate. This is seen in Figure 8.6. Part (a) of this figure is a log-log plot of dimensionless peak height vs σ, and shows a very clear change of gradient. Part (b) shows the value of this gradient, which changes from one at low σ to a half at high σ.

Simulated cyclic voltammograms at a porous electrode are shown in Figure 8.7 for dimensionless electrochemical rate constants of (a): 1×10^{-1}, (b): 1×10^{-2}, (c): 1×10^{-3} and (d): 1×10^{-4}. Other parameters are $\sigma = 0.01$, $R_d = 4000$, $\alpha = 0.5$ and $N_\mathrm{s} = 1 \times 10^{8}$.

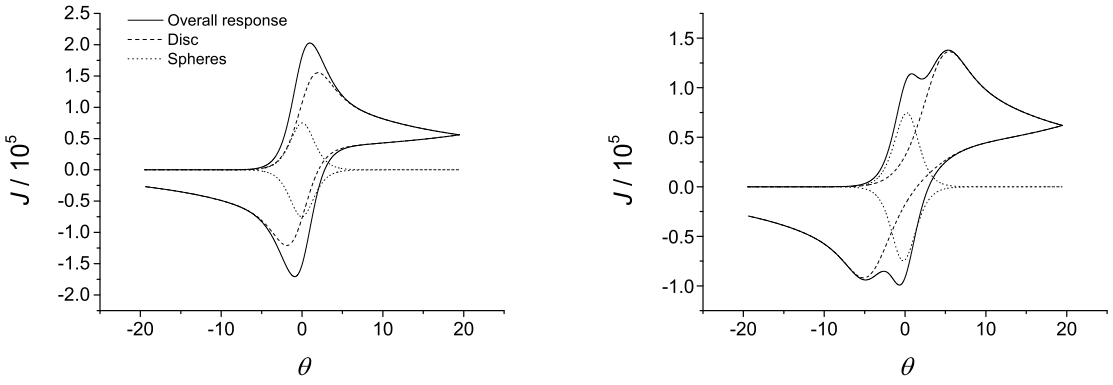


(a) (b)

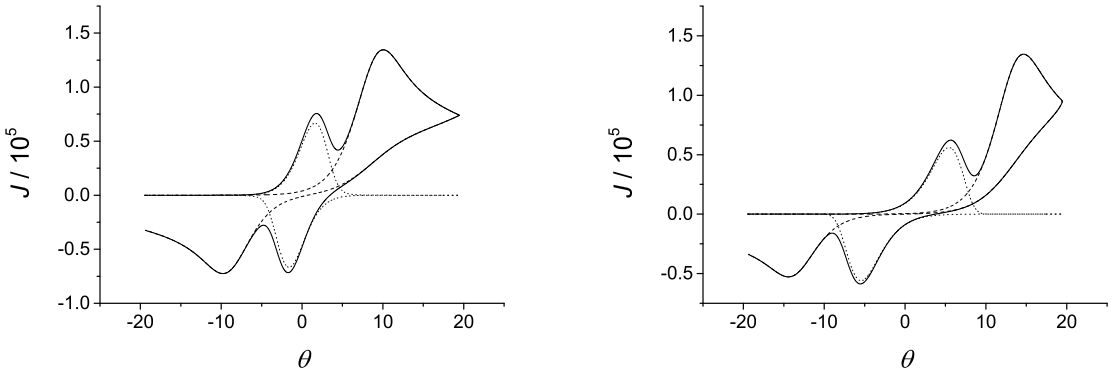
Figure 8.6: (a) Decadic log of dimensionless peak current simulated inside a sphere as a function of dedadic log of dimensionless scan rate. K^0 is set at 10^5 to ensure complete electrochemical reversibility over the whole range. (b) shows the gradient of (a).

It is seen that for the largest electrochemical rate constant, only one peak is observed in each direction of the scan. As the electrochemical rate constant is lowered however, two peaks emerge, initially close together but getting further apart at smaller K^0 values. Also shown in this figure are the relative contributions from electrolysis inside the spheres and from the overall disc (dotted and dashed lines respectively). It is seen that the cause of the peak splitting is the different responses from these two parts of the electrode (hollow voids and exposed surface) to a change in K^0. The reasons for this peak splitting are discussed in detail below.

Further to these simulated voltammograms showing the effect of changing K^0, Figure 8.8 shows the effect of changing the number of hollow spheres in the porous electrode and changing the radius of the overall disc electrode. Part (a) of this figure shows simulated voltammograms for a porous electrode for parameters in Figure 8.7 (d), but with varying numbers of hollow spheres N_s = 0, 1, 2.5, 5, 7.5 and 10 $\times 10^7$, as indicated on the figure, with R_d fixed at 4000. It is seen that the first wave in the forward scan changes size as the number of spheres is changed, and is absent if no hollow spheres are present. It is



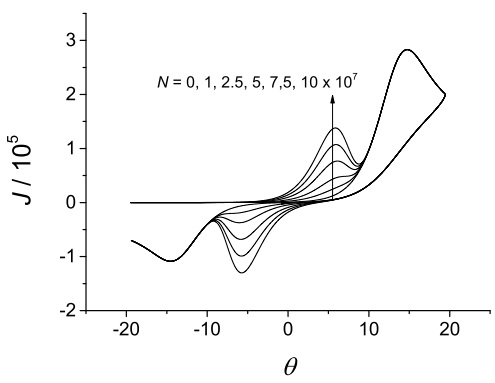
(a) $K^0 = 10^{-1}$ (b) $K^0 = 10^{-2}$



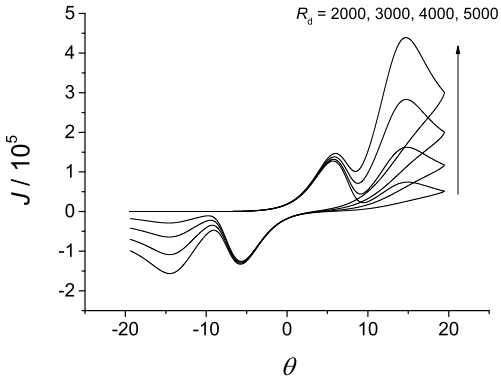
(c) $K^0 = 10^{-3}$ (d) $K^0 = 10^{-4}$

Figure 8.7: Simulated voltammograms at a porous electrode with $\sigma = 0.01$, $R_d = 4000$, $\alpha = 0.5$, $N_s = 1 \times 10^8$ and electrochemical rate constants of (a): 1×10^{-1}, (b): 1×10^{-2}, (c): 1×10^{-3} and (d): 1×10^{-4}.

also seen that for small numbers of spheres (1.0 and to a lesser extent 2.5 $\times 10^7$) then the small pre-peak is difficult to resolve and the precise position of the peak is essentially unreadable. Part (b) of this figure is as part (a), but with N_s fixed at 10^8 and R_d at 2000, 3000, 4000 and 5000. It is seen that the response due to the overall disc increases as is expected, but for these parameters does not swamp the thin layer signal from inside the spheres. It should be noted however that if R_d becomes extremely large, the thin layer signal will become unresolvable. We below consider the analytical implications of this peak splitting.



(a) Vary the number of spheres



(b) Vary the radius of the disc

Figure 8.8: Simulated dimensionless voltammograms showing (a) various numbers of hollow spheres in the porous layer, with R_{d} fixed at 4000, and (b) various values of R_{d} with N_{S} fixed at 10^8. Other parameters are $\sigma = 0.01$, $\alpha = 0.5$, $K^0 = 1 \times 10^{-4}$.

8.3.3 The possibility of two peaks arising from a single $\mathrm{A} \pm \mathrm{e}^- \rightleftharpoons \mathrm{B}$ process

Of particular interest is comparing the effect on the voltammetry of changing the electrochemical rate constant, K^0, on the response inside spheres and at a planar macrodisc electrode. Henstridge *et. al.* predicted that at porous film electrodes a single electron transfer process can result in the observation of two peaks in cyclic voltammetry, one from electrolysis within the porous film and the other from semi-infinite linear diffusion at the film surface [36, 37]. The thin layer response from inside the spheres makes the transition from being electrochemically reversible to irreversible in character at lower electrochemical rate constants than the diffusional disc response. The fact that this transition from fully reversible to fully irreversible takes place over a different range of electrochemical rate constants in the two cases means that, for electrochemical rate constants outside the fully reversible limit, two peaks are seen, one from thin layer electrolysis inside the pores, and one from linear diffusion to the exposed surface. The separation of these peaks is a

function of K^0, with the peaks becoming more separated at smaller K^0, until a limiting separation is reached. This peak splitting may provide a means of directly extracting an *approximate* value for the electrochemical rate constant and formal potential from experimental data, as described below.

8.3.4 Extraction of K^0

This voltammetric splitting of one peak into two peaks as the electrochemical rate constant is lowered provides an approximate means of estimating K^0, which is impossible for a fully irreversible system from a single peak unless the formal potential, $E_f^{\ominus}$, is known. It is therefore only possible to extract a combined parameter $k^0 \exp\left(\frac{\alpha F E_f^{\ominus}}{RT}\right)$ if only one irreversible peak is seen. If the forward wave contains two peaks however, as here predicted for a porous electrode, then the separation of these two peaks as a function of scan rate may be used to extract an approximate value of K^0, and hence $\theta_f^{\ominus}$, if α is known (or measured). Figure 8.9(a) shows the simulated peak potential on the forward scan for inside spheres ($\theta_{\mathrm{p}}^{\mathrm{sphere}}$) plotted as a function of $\log_{10}(\sigma)$ and $\log_{10}(K^0)$. Figure 8.9(b) shows the same for a macrodisc ($\theta_{\mathrm{p}}^{\mathrm{disc}}$), and Figure 8.9(c) shows the difference between the two cases ($\Delta\theta_{\mathrm{p}}$). In Figure 8.9(c), we see that the separation between the peak responses due to the interior of the spheres and the overall disc is a function of both σ and K^0.

For very large values of σ, the diffusion zone is close to the electrode surface for both inside the spheres and for the disc, thus a diffusional signal is observed for both. In this extreme, there is no peak separation, the electrochemistry is blind to the overall geometry of the electrode at which it occurs.

If σ is small but K^0 is large, then the response from inside the spheres will be thin layer

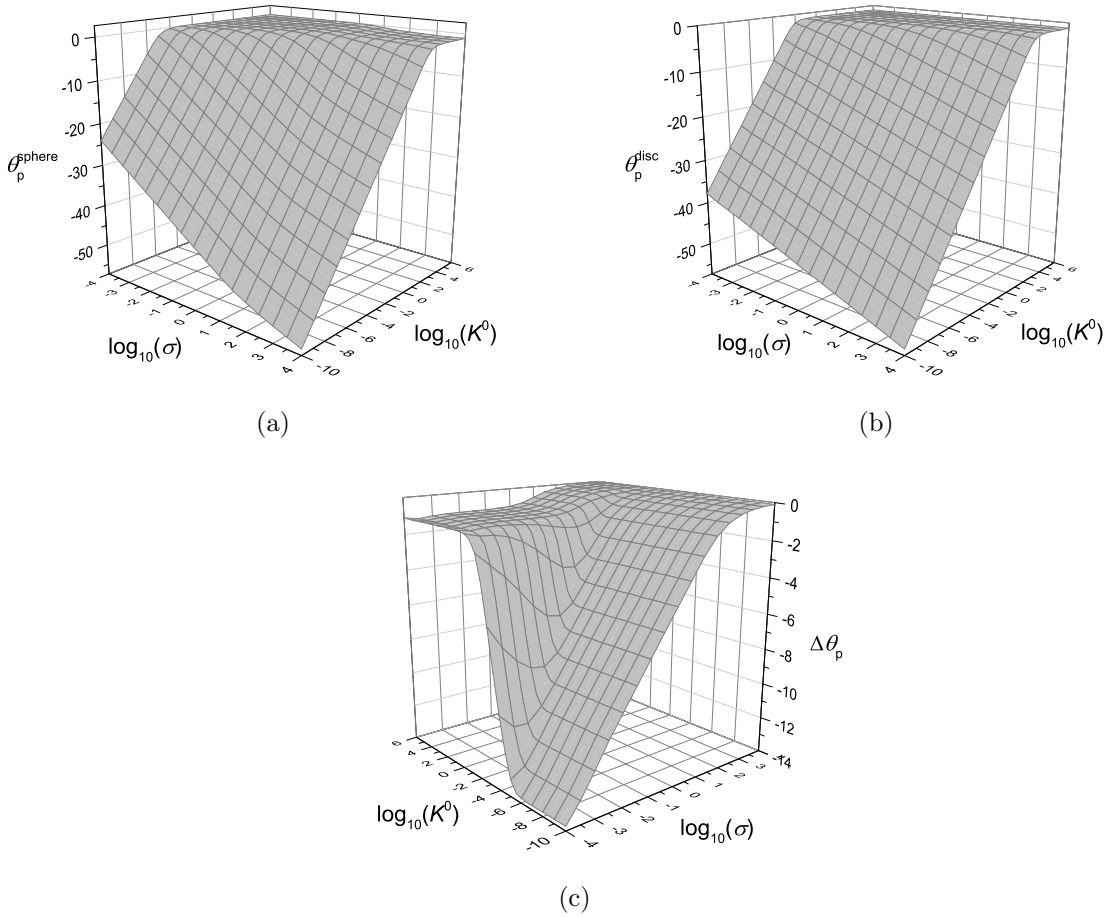


Figure 8.9: Dimensionless peak potential for a range of dimensionless scan rates and electrochemical rate constants for (a) inside spheres and (b) at macrodiscs. (c) The difference between the two.

in nature, and the disc response diffusional, but both responses are fully reversible. This leads to a constant, small peak separation. This corresponds to the simulated voltammograms shown in Figure 8.7 (a), the peaks are not separated enough to be resolved into two separate peaks.

If K^0 is small, then the peak separation becomes a function of σ. As σ is lowered from very large values, the peak separation moves away from zero (see above) and the peaks begin to shift away from each other more and more, until the separation passes through a maximum and the peaks begin to move closer together again. The point at which this maximum is reached is a function of K^0, occurring at lower values of σ as K^0 becomes

smaller.

Noting the above, K^0 can in principle be extracted from experimental data obtained over a wide range of scan rates which contain the point of maximum separation described above. The peak separations can be plotted as a function of scan rate and compared to this working surface to estimate K^0. $\theta_f^{\ominus}$ can then also be extracted from the position of the peaks. It should be noted that the data in Figure 8.9 is simulated using an α value of 0.5. For experimental data, an α value must be obtained via Tafel analysis and a working surface specific to the obtained α simulated. It should also be noted that this method assumes the ideal geometry of diffusionally independent perfectly spherical pores. This will therefore give us at least a highly approximate estimate of K^0 in any real system, where these assumptions are unlikely to be adhered to. In particular the idealised porous electrode structure here simulated is unlikely to be rigorously accurate.

As alluded to above, it should be noted that for small separations in peak potential between the response inside spheres and the response of the disc, the overall response may still contain a single unresolved peak, as in Figure 8.7 (a), where the responses overlap. The number of spheres present on the surface also has an impact, too few and the thin layer signal will be swamped by the diffusional signal and not visible. This is demonstrated in Figure 8.8. It is seen that for a small number of spheres ($N_s = 1 \times 10^7$ and to a lesser extent 2.5×10^7) then the peak position of the first, thin layer signal is not readily readable. Thus for the proposed approximate method of extracting k^0, it is desirable to have very clearly defined peaks to read off the peak positions, so an optimal number of spheres on the surface is desirable so two peaks are visible although not so large that the signal from inside the spheres begins to swamp the signal from the disc.

8.4 Conclusions

We have developed a theory which allows insight into the electrochemistry of porous electrode structures formed via electroplating around spherical templates which are then removed. It is concluded that in chronoamperometry the timescale for diffusional transport within the spherical voids of the porous layer is so fast that its contribution is usually masked by double layer charging effects. In cyclic voltammetry however, significant contributions from electrolysis of material both within the voids and from semi-infinite linear diffusion to the electrode surface is predicted to be observed. This mixed contribution of thin layer and semi infinite diffusion is shown, in principle, to be useful in extracting electrochemical rate constants for quasi-reversible and irreversible electron transfer processes.

References

[1] Barnes, E. O.; Chen, X.; Li, P.; Compton, R. G. *J. Electroanal. Chem.* **2014**, *720*, 92 – 100.

[2] Szamocki, R.; Reculusa, S.; Ravaine, S.; Bartlett, P. N.; Kuhn, A.; Hempelmann, R. *Angew. Chem. Int. Ed.* **2006**, *45*, 1317 – 1321.

[3] Szamocki, R.; Velichko, A.; Holzapfel, C.; Mücklich, F.; Ravaine, S.; Garrigue, P.; Sojic, N.; Hempelmann, R.; Kuhn, A. *Anal. Chem.* **2007**, *79*, 533 – 539.

[4] Lenz, J.; Trieu, V.; Hempelmann, R.; Kuhn, A. *Electroanalysis* **2011**, *23*, 1186 – 1192.

[5] Chen, X.; Xuan, J.; Jiang, L.; Zhu, J. *Sci. in China B* **2009**, *52*, 1999 – 2005.

[6] Chen, X.; Chen, Z.; Tian, R.; Yan, W.; Yao, C. *Anal. Chim. Acta* **2012**, *723*, 94 – 100.

[7] Chen, X.; Zhu, J.; Tian, R.; Yao, C. *Sens. Actuators B* **2012**, *163*, 272 – 280.

[8] Zhang, Y.; Zeng, L.; Bo, X.; Wang, H.; Guo, L. *Anal. Chim. Acta* **2012**, *752*, 45 – 52.

[9] Wei, N.; Xin, X.; Du, J.; Li, J. *Biosens. Biolelectron.* **2011**, *26*, 3602 – 3607.

[10] Chen, X.; Wang, Y.; Zhou, J.; Yan, W.; Li, X.; Zhu, J. *Anal. Chem.* **2008**, *80*, 2133 – 2140.

[11] Li, X.; Dai, L.; Liu, Y.; Chen, X.; Yan, W.; Chen, X.; Zhu, J. *Adv. Funct. Mater.* **2009**, *19*, 3120 – 3128.

[12] Chen, X.; Zhou, J.; Xuan, J.; Yan, W.; Jiang, L.; Zhu, J. *Analyst* **2010**, *135*, 2629–2636.

[13] Whicher, J.; Biasucci, L.; Rifai, N. *Clin. Chem. Lab. Med.* **1999**, *37*, 495 – 503.

[14] Haidari, M.; Moghadam, M.; Chinicar, M.; Ahmadieh, A.; Doosti, M. *Clin. Biochem.* **2001**, *34*, 149 – 155.

[15] Streeter, I.; Wildgoose, G. G.; Shao, L.; Compton, R. G. *Sens. Actuators, B* **2008**, *133*, 462 – 466.

[16] Sims, M. J.; Rees, N. V.; Dickinson, E. J. F.; Compton, R. G. *Sens. Actuators B* **2010**, *144*, 153 – 158.

[17] Henstridge, M. C.; Dickinson, E. J. F.; Aslanoglu, M.; Batchelor-McAuley, C.; Compton, R. G. *Sens. Actuators B* **2010**, *145*, 417 – 427.

[18] Punckt, C.; Pope, M. A.; Aksay, I. A. *J. Phys. Chem. C* **2013**, *117*, 16076 – 16086.

[19] Brookes, B. A.; Davies, T. J.; Fisher, A. C.; Evans, R. G.; Wilkins, S. J.; Yunus, K.; Wadhawan, J. D.; Compton, R. G. *J. Phys. Chem. B* **2003**, *107*, 1616 – 1627.

[20] Davies, T. J.; Moore, R. R.; Banks, C. E.; Compton, R. G. *J. Electroanal. Chem.* **2004**, *574*, 123 – 152.

[21] Davies, T. J.; Banks, C. E.; Compton, R. G. *J. Solid State Electrochem.* **2005**, *9*, 797 – 808.

[22] Chevallier, F. G.; Davies, T. J.; Klymenko, O. V.; Jiang, L.; Jones, T. G. J.; Compton, R. G. *J. Electroanal. Chem.* **2005**, *577*, 211 – 221.

[23] Davies, T. J.; Brookes, B. A.; Fisher, A. C.; Yunus, K.; Wilkins, S. J.; Greene, P. R.; Wadhawan, J. D.; Compton, R. G. *J. Phys. Chem. B* **2003**, *107*, 6431 – 6444.

[24] Davies, T. J.; Compton, R. G. *J. Electroanal. Chem.* **2005**, *585*, 63 – 82.

[25] Davies, T. J.; Ward-Jones, S.; Banks, C. E.; Del Campo, J.; Mas, R.; Munoz, F. X.; Compton, R. G. *J. Electroanal. Chem.* **2005**, *585*, 51 – 62.

[26] Shoup, D.; Szabo, A. *J. Electroanal. Chem.* **1982**, *140*, 237 – 245.

[27] Paddon, C. A.; Silvester, D. S.; Bhatti, F. L.; Donohoe, T. J.; Compton, R. G. *Electroanalysis* **2007**, *19*, 11 – 22.

[28] Klymenko, O. V.; Evans, R. G.; Hardacre, C.; Svir, I. B.; Compton, R. G. *J. Electroanal. Chem.* **2004**, *571*, 211 – 221.

[29] Gavaghan, D. J. *J. Electroanal. Chem.* **1998**, *456*, 1 – 12.

[30] Gavaghan, D. J. *J. Electroanal. Chem.* **1998**, *456*, 13 – 23.

[31] Gavaghan, D. J. *J. Electroanal. Chem.* **1998**, *456*, 25 – 35.

[32] Press, W. H., Teukolsky, S. A., Vetterling, W. T., Flannery, B. P., Eds. *Numerical Recipes: The Art of Scientific Computing*; Cambridge University Press, 2007.

[33] Cottrell, F. G. *Z. Physik. Chem.* **1903**, *42*, 385 – 431.

[34] Compton, R. G.; Banks, C. E. *Understanding Voltammetry*, 2nd ed.; World Scientific: Singapore, 2010.

[35] Zhou, J.; Huang, H.; Xuan, J.; Zhang, J.; Zhu, J. *Biosens. Bioelectron.* **2010**, *26*, 834 – 840.

[36] Henstridge, M. C.; Dickinson, E. J. F.; Compton, R. G. *Russ. J. Electrochem.* **2012**, *48*, 6329 – 2333.

[37] Xia, S.; Yu, M.; Hu, J.; Feng, J.; Chen, J.; Shi, M.; Weng, X. *Electrochem. Commun.* **2014**, *40*, 67 – 70.

Chapter 9

Equivalence of Microdisc and Sphere-On-Surface Electrodes In the Marcus-Hush Formalism

The previous six chapters have all considered electron transfer kinetics to be governed by Butler-Volmer theory, as introduced in Chapter 1. There exists, however, a competing model to describe electron transfer kinetics, Marcus-Hush theory. This chapter introduces this theory, and applies it to simulate steady state voltammetry at a microdisc electrode and a sphere-on-a-surface electrode. We investigate the possibility of kinetically, rather than diffusionally, limited currents at the two geometries, and establish the ideal conditions under which these may be observed. A previously established equivalence between steady state voltammetry at microdisc electrodes and sphere-on-a-surface electrodes is also shown to extend to kinetically limited currents predicted using Marcus-Hush theory. The work presented in this chapter has been published in *The Journal of Electroanalytical Chemistry* [1].

9.1 Introduction

Any kinetic model of electron transfer aims to quantify the values of k_{red} and k_{ox} in the heterogeneous electron transfer reaction:

$$\mathrm{A} + \mathrm{e}^- \rightleftharpoons \mathrm{B} \tag{9.1}$$

where the flux across the electrode surface is given by:

$$j_0 = k_{\mathrm{red}} c_{\mathrm{A}}^0 - k_{\mathrm{ox}} c_{\mathrm{B}}^0 \tag{9.2}$$

Butler-Volmer theory, introduced in Chapter 1, does this by introducing transfer coefficients α and β (where $\alpha + \beta = 1$) which, along with the standard electrochemical rate constant, give the following expressions [2, 3]:

$$k_{\mathrm{red}} = k^0 \exp\left[-\alpha \frac{F\left(E - E_{\mathrm{f}}^{\ominus}\right)}{RT}\right] \tag{9.3}$$

$$k_{\mathrm{ox}} = k^0 \exp\left[\beta \frac{F\left(E - E_{\mathrm{f}}^{\ominus}\right)}{RT}\right] \tag{9.4}$$

The simplicity of this model has resulted in its widespread application in electrochemical simulation, with a high level of success. However, the only physical insight gained from the model is an indication of whether the transition state for the electron transfer is reactant like ($\alpha \sim 0$), product like ($\alpha \sim 1$) or intermediate ($\alpha \sim 0.5$).

A more rigorous model is the Marcus-Hush theory of electron transfer, which considers the process of electron transfer microscopically. This model was first proposed by Marcus for outer sphere electron transfer [4–7], before being extended by Hush to include inner

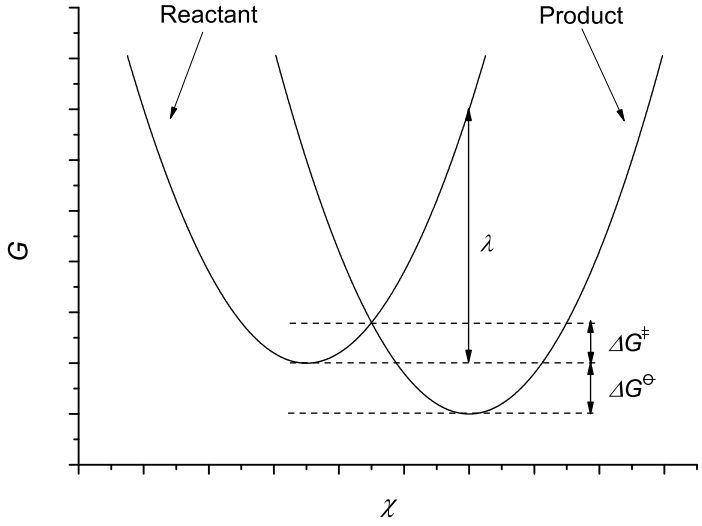


Figure 9.1: Gibbs energy curves for the reactant and product of a homogeneous electron transfer.

sphere transfer [8].

Potential energy curves for two solution phase species are shown in Figure 9.1. The Arrhenius Equation can be used to calculate the rate constant for electron transfer from the reactant to the product:

$$k = A \exp\left[-\frac{\Delta G^{\ddagger}}{RT}\right] \tag{9.5}$$

If the curves in Figure 9.1 are assumed to be parabolic with equal force constants, it can be shown that the Gibbs energy of activation, $\Delta G^{\ddagger}$, is equal to:

$$\Delta G^{\ddagger} = \frac{\lambda}{4}\left(1 + \frac{\Delta G^{\ominus}}{\lambda}\right)^2 \tag{9.6}$$

where λ is the reorganisation energy, the extent to which the molecules in question and the surrounding solvent must reorganise themselves to accommodate the electron transfer.

This homogeneous picture must be modified when considering heterogeneous transfer

from an electrode to a solution phase species [9]. An electron in a metallic electrode can exist in any one of a continuum of energy levels, each of which has energy $F\epsilon_{\mathrm{i}}$. Using the relationship:

$$\Delta G^{\ominus} = F\left(\epsilon_{\mathrm{i}} - E_{\mathrm{f}}^{\ominus}\right) \tag{9.7}$$

Equation 9.6 can be rewritten as:

$$\Delta G^{\ddagger}_{\mathrm{red/ox}}\left(\epsilon_{\mathrm{i}}\right) = \frac{\lambda}{4}\left[1 \pm \frac{F\left(\epsilon_{\mathrm{i}} - E_{\mathrm{f}}^{\ominus}\right)}{\lambda}\right]^2 \tag{9.8}$$

The rate constant for reduction or oxidation can then be written:

$$k_{\mathrm{red/ox}} = \sum_{\mathrm{i}} f_{\pm}\left(\epsilon_{\mathrm{i}}\right) A\left(\epsilon_{\mathrm{i}}\right) \rho\left(\epsilon_{\mathrm{i}}\right) \exp\left[\frac{-\Delta G^{\ddagger}_{\mathrm{red/ox}}\left(\epsilon_{\mathrm{i}}\right)}{RT}\right] \tag{9.9}$$

where $A\left(\epsilon_{\mathrm{i}}\right)$ is the electronic coupling between the electrode and solution species, $\rho\left(\epsilon_{\mathrm{i}}\right)$ is the density of states and $f_{\pm}\left(\epsilon_{\mathrm{i}}\right)$ is the probability of occupancy (f_+ for a reduction) or vacancy (f_- for an oxidation) of state i in the electrode. This is given by the Fermi-Dirac distribution:

$$f_{\pm}\left(\epsilon_{\mathrm{i}}\right) = \frac{1}{1 + \exp\left[\mp\frac{F}{RT}\left(\epsilon_{\mathrm{i}} - E\right)\right]} \tag{9.10}$$

Making the assumption that both $A\left(\epsilon_{\mathrm{i}}\right)$ and the density of states, $\rho\left(\epsilon_{\mathrm{i}}\right)$, are independent of energy [9], Equation 9.9 may be recast as an integral (since the individual energy levels exist essentially as a continuum):

$$k_{\mathrm{red/ox}} = A\rho \int_{-\infty}^{\infty} f_{\pm}\left(\epsilon\right) \exp\left[\frac{-\Delta G^{\ddagger}_{\mathrm{red/ox}}\left(\epsilon\right)}{RT}\right] \mathrm{d}\epsilon \tag{9.11}$$

which may be rewritten as:

$$k_{\mathrm{red/ox}} = A\rho \int_{-\infty}^{\infty} \frac{\exp\left[-\frac{\Lambda}{4}\left(1 \pm \frac{\theta+x}{\Lambda}\right)^2\right]}{1+\exp\left[\mp x\right]} \mathrm{d}x \tag{9.12}$$

where x is a dimensionless integration variable given by:

$$x = \frac{F}{RT}\left(\epsilon - E\right) \tag{9.13}$$

θ is a dimensionless applied potential:

$$\theta = \frac{F}{RT}\left(E - E_{\mathrm{f}}^{\ominus}\right) \tag{9.14}$$

and Λ is the dimensionless reorganisation energy:

$$\Lambda = \frac{F}{RT}\lambda \tag{9.15}$$

To eliminate the unknown quantities A and ρ, the rate constants are expressed in terms of the standard electrochemical rate constant, k^0, the rate constant for oxidation and reduction when $\theta = 0$:

$$k_{\mathrm{red}} = k^0 \frac{S_{\mathrm{red}}\left(\theta,\, \Lambda\right)}{S_{\mathrm{red}}\left(0,\, \Lambda\right)} \tag{9.16}$$

$$k_{\mathrm{ox}} = k^0 \frac{S_{\mathrm{ox}}\left(\theta,\, \Lambda\right)}{S_{\mathrm{ox}}\left(0,\, \Lambda\right)} \tag{9.17}$$

where

$$S_{\mathrm{red/ox}}\left(\theta,\, \Lambda\right) = \int_{-\infty}^{\infty} \frac{\exp\left[-\frac{\Lambda}{4}\left(1 \pm \frac{\theta+x}{\Lambda}\right)^2\right]}{1+\exp\left(\mp x\right)} \mathrm{d}x \tag{9.18}$$

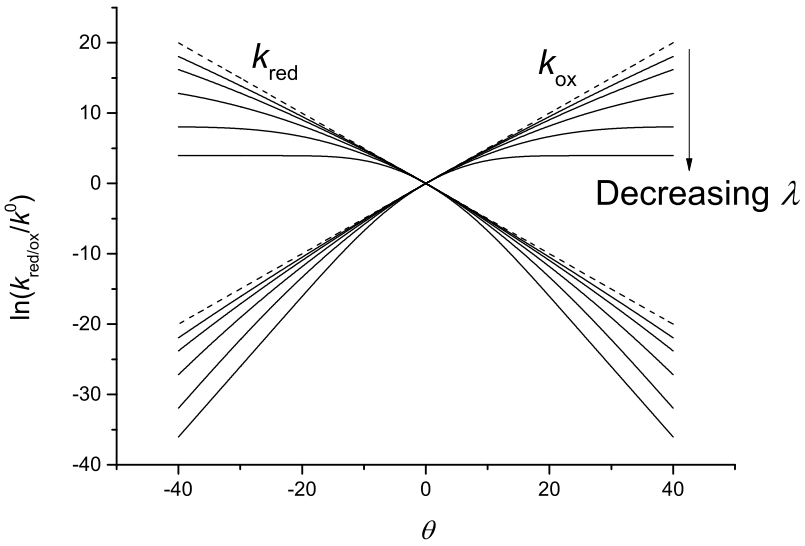


Figure 9.2: k_{red} and k_{ox} calculated using Marcus-Hush theory as a function of dimensionless overpotential for Λ values of 200, 100, 50, 25 and 10. Dotted lines show the Butler-Volmer rate constants for an α value of 0.5.

The principal difference between Marcus-Hush theory and Butler-Volmer theory is the behaviour of k_{red} and k_{ox} at large overpotentials. Butler-Volmer theory predicts that these rate constants will increase exponentially with overpotential (Equations 9.3 and 9.4). For large values of Λ, this is also the case under the Marcus-Hush formalism. For small values of Λ, however, the rate constants approach limiting values at large overpotentials. This is shown in Figure 9.2.

As mentioned above, in this derivation of Marcus theory, the force constants for the parabolic Gibbs energy curves in Figure 9.1 are assumed to be equal. This leads to what is known as symmetric Marcus-Hush theory. A natural extension of this theory is to remove this assumption, and allow the force constants of the two curves to be independent of one another. This is referred to as asymmetric Marcus-Hush theory.

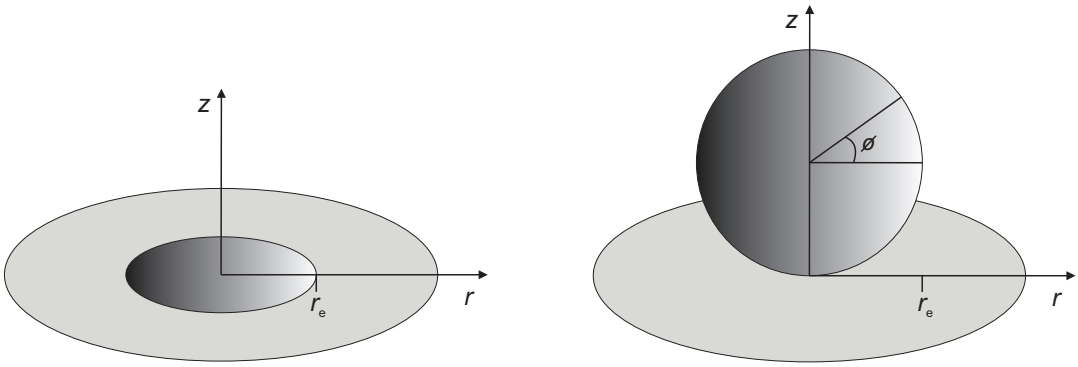
Marcus-Hush theory was first used to successfully simulate experimental electrochem-

istry by Chidsey [9], who carried out potential step chronoamperometry on surface bound ferrocene. Symmetric Marcus-Hush theory was able to accurately predict the limiting values of the rate constants at large overpotentials, a result reproduced in several studies of different systems [10–22]. Where the symmetric model failed to fully reproduce experimental data for the voltammetry of adsorbed species, the asymmetric extension was found to be successful [23].

Diffusional systems have also been investigated using symmetric [24–28] and asymmetric [29–33] Marcus-Hush theory. In general, symmetric Marcus-Hush theory was found simulate experimental data as accurately as Butler-Volmer theory for α values of approximately 0.5. If α deviated form this, asymmetric Marcus-Hush theory was required to accurately reproduce experimental data [34].

Theoretical studies carried out by Feldberg [35] and Henstridge *et. al.* [36] showed that in the Marcus-Hush model of electron transfer kinetics, steady state currents can be kinetically rather than diffusionally limited for small values of the reorganisation energy, λ. In Feldberg's study, an approximate equation of Oldham and Zoski [37] describing steady state voltammetry at a microdisc electrode was invoked and modified to use Marcus-Hush, rather than Butler-Volmer kinetics. Henstridge used numerical simulation to generate Marcus-Hush steady state responses at a conductive nanosphere resting on an electrochemically inert but conductive surface.

In this study, we simulate steady state voltammetry numerically using the symmetric Marcus-Hush formalism of electron transfer, and compare the circumstances in which a kinetically limited current is observed at a microdisc to those at a nanosphere. We also extend previous work showing the equivalence of microdiscs and spheres-on-surfaces under the Butler-Volmer formalism (subject to a mass transport correction factor) [38],



(a) Microdisc (b) Sphere-on-a-surface

Figure 9.3: Schematic diagrams of (a) a microdisc electrode and (b) a sphere-on-a-surface electrode, showing the coordinate systmes used.

and show that the approximate equivalence is retained when Marcus-Hush kinetics are used.

9.2 Theory

We aim to simulate steady state voltammetry of the one electron reduction process:

$$\mathrm{A} + \mathrm{e}^- \rightleftharpoons \mathrm{B} \tag{9.19}$$

at a microdisc electrode and a sphere-on-a-surface electrode, representing an electroactive nanoparticle impacting upon a conductive, but electrochemically inert, surface. These two geometries are shown schematically in Figure 9.3, which also defines the cylindrical coordinates used in the simulations.

The (dimensionless) mass transport equation is the same for both geometries, and is given in cylindrical space by:

$$\frac{\partial C_\mathrm{i}}{\partial \tau} = D_\mathrm{i}^{'} \left(\frac{\partial^2 C_\mathrm{i}}{\partial R^2} + \frac{1}{R}\frac{\partial C_\mathrm{i}}{\partial R} + \frac{\partial^2 C_\mathrm{i}}{\partial Z^2} \right) \tag{9.20}$$

All dimensionless parameters are defined in the Glossary.

9.2.1 Boundary conditions

Initial conditions are set such that at dimensionless time $\tau < 0$, both species are present everywhere in bulk concentration:

$$\tau < 0; \text{ all } R; \text{ all } Z; \quad C_{\mathrm{A}} = 1 \quad C_{\mathrm{B}} = 0 \tag{9.21}$$

At time $\tau = 0$, the starting potential is applied to the electrode and electrolysis occurs, The boundary condition applied at the electrode surface depends on whether Butler-Volmer or Marcus-Hush electrode kinetics are being used. In both cases, the equation takes the form:

$$\left(\frac{\partial C_{\mathrm{A}}}{\partial Z}\right)_{R \leq 1} = K_{\mathrm{red}} C_{\mathrm{A}}^{0} - K_{\mathrm{ox}} C_{\mathrm{B}}^{0} \tag{9.22}$$

for a microdisc and:

$$\left(\frac{\partial C_{\mathrm{A}}}{\partial N}\right)_{R^2+(Z-1)^2=1} = K_{\mathrm{red}} C_{\mathrm{A}}^{0} - K_{\mathrm{ox}} C_{\mathrm{B}}^{0} \tag{9.23}$$

for a sphere-on-a-surface, where N is some coordinate normal to the electrode surface. Under the Butler-Volmer formalism, the dimensionless values K_{red} and K_{ox} are given by:

$$K_{\mathrm{red}} = K^{0} \exp\left[-\alpha\theta\right] \qquad K_{\mathrm{ox}} = K^{0} \exp\left[(1-\alpha)\,\theta\right] \tag{9.24}$$

Using Marcus-Hush kinetics, the rate constants are given by:

$$K_{\mathrm{red}} = K^{0} \frac{S_{\mathrm{red}}\left(\theta,\, \Lambda\right)}{S_{\mathrm{red}}\left(0,\, \Lambda\right)} \qquad K_{\mathrm{ox}} = K^{0} \frac{S_{\mathrm{ox}}\left(\theta,\, \Lambda\right)}{S_{\mathrm{ox}}\left(0,\, \Lambda\right)} \tag{9.25}$$

Boundary			Condition
$\tau < 0$	All R	All Z	$C_{\mathrm{A}} = 1$, $C_{\mathrm{B}} = 0$
$\tau \geq 0$	$R \leq 1$	$Z = 0$	$D'_{\mathrm{A}} \left(\frac{\partial C_{\mathrm{A}}}{\partial Z}\right) = K_{\mathrm{red}} C^0_{\mathrm{A}} - K_{\mathrm{ox}} C^0_{\mathrm{B}}$ $D'_{\mathrm{B}} \left(\frac{\partial C_{\mathrm{B}}}{\partial Z}\right) = -D'_{\mathrm{A}} \left(\frac{\partial C_{\mathrm{A}}}{\partial Z}\right)$
	$R > 1$		$\frac{\partial C_{\mathrm{i}}}{\partial Z} = 0$
	$R = 0$	All Z	$\frac{\partial C_{\mathrm{i}}}{\partial R} = 0$
	$R = R_{\max}$		
	All R	$Z = Z_{\max}$	$\frac{\partial C_{\mathrm{i}}}{\partial Z} = 0$

Table 9.1: Normalised boundary conditions to simulate cyclic voltammetry at a microdisc electrode

where $S_{\mathrm{red/ox}}(\theta, \Lambda)$ is defined in Equation 9.18.

The applied potential, θ, is given by the equation:

$$\theta = \theta_{\mathrm{v}} + |\theta_{\mathrm{v}} - \theta_{\mathrm{s}} + \sigma\tau| \tag{9.26}$$

where σ is the dimensionless scan rate. To simulate steady state voltammetry, σ is fixed at 10^{-4}.

Other boundary conditions are as in previous chapters, with zero flux across the $R = 0$ symmetry boundary and at insulating surfaces, and bulk concentrations set at $R_{\max}$ and $Z_{\max}$ (which are set at $6\sqrt{D'_{\max}\tau_{\max}}$ from the electrode in both directions). The boundary conditions for a microdisc and a sphere-on-a-surface are summarised in Tables 9.1 and 9.2

Boundary			Condition
$\tau < 0$	All R	All Z	$C_{\mathrm{A}} = 1,\, C_{\mathrm{B}} = 0$
$\tau \geq 0$	$R^2 + (Z-1)^2 = 1$		$D'_{\mathrm{A}} \left(\frac{\partial C_{\mathrm{A}}}{\partial Z}\right) = K_{\mathrm{red}} C^0_{\mathrm{A}} - K_{\mathrm{ox}} C^0_{\mathrm{B}}$ $D'_{\mathrm{B}} \left(\frac{\partial C_{\mathrm{B}}}{\partial Z}\right) = -D'_{\mathrm{A}} \left(\frac{\partial C_{\mathrm{A}}}{\partial Z}\right)$
	$R > 0$	$Z = 0$	$\frac{\partial C_{\mathrm{i}}}{\partial Z} = 0$
	$R = 0$	$Z > 2$	$\frac{\partial C_{\mathrm{i}}}{\partial R} = 0$
	$R = R_{\max}$	All Z	
	All R	$Z = Z_{\max}$	$\frac{\partial C_{\mathrm{i}}}{\partial Z} = 0$

Table 9.2: Normalised boundary conditions to simulate cyclic voltammetry at a sphere-on-a-surface electrode

respectively.

The total dimensionless flux at a microdisc electrode is found by integrating the flux over the electrode surface:

$$J_{\mathrm{disc}} = \int_1^0 R \left(\frac{\partial C_{\mathrm{A}}}{\partial Z}\right)_{\mathrm{Z=0}} \mathrm{d}R \tag{9.27}$$

The total flux at a sphere-on-a-surface electrode is also found by integrating over the electrode surface, summing contributions in the R and Z directions:

$$J_{\mathrm{disc}} = \int_{-\pi/2}^{\pi/2} \left[\left(\frac{\partial C_{\mathrm{A}}}{\partial R}\right)_{\mathrm{Z=0}} \cos\phi + \left(\frac{\partial C_{\mathrm{A}}}{\partial Z}\right)_{\mathrm{Z=0}} \sin\phi \right] \cos\phi \; \mathrm{d}\phi \tag{9.28}$$

9.2.2 Numerical Methods

The above model is discretised using the methods desribed in Chapter 2 and solved numerically over discrete spatial and temporal grids. The temporal grid is defined initially in terms of the applied dimensionless potential, θ. A parameter N_θ is defined as the number of discrete time steps per unit θ, as in Chapters 7 and 8.

A non regular, exponentially expanding spatial grid is used to ensure computational efficiency. In the Z direction, the first spatial point (at the electrode/insulating surface) is defined as $Z_0 = 0$. The first step size is defined as Δ, with subsequent step sizes growing increasingly large until the simulation boundary is reached. Each Z direction spatial point is defined as:

$$Z_j = Z_{j-1} + \gamma\,(Z_{j-1} - Z_{j-2}) \tag{9.29}$$

The R direction spatial grid is defined in the same way, except that rather than expanding from a simulation boundary, the grid expands away from the edge of the electrode at $R = 1$ in both directions until $R = 0$ and $R = R_{\max}$ are reached.

In order to achieve convergence to within 0.5% of a fully converged result, the following grid parameters were used: $N_\theta = 1000$, $\Delta = 8 \times 10^{-5}$ and $\gamma = 1.25$.

The temporal grid for the simulation of voltammetry at a spherical electrode is the same as defined above for a microdisc electrode. To define the spatial grid, the geometry of the electrode is taken into account. The electrode surface is divided into N_ϕ equal spaced points, with a grid vertex at each of these points. This defines the grid points in the region $R \leq 1$ and $Z \leq 2$, as shown schematically in Figure 9.4. In the regions $R > 1$ and $Z > 2$, the grid expands exactly as outlined for the microdisc above. Convergence studies found $N_\phi = 200$ sufficient to ensure convergence.

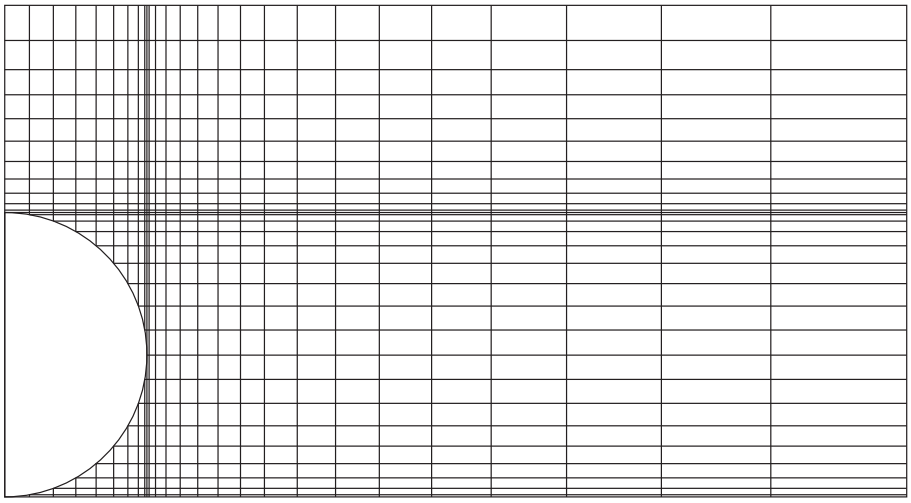


Figure 9.4: Schematic diagram of the spatial grid used in the sphere-on-a-surface simulations.

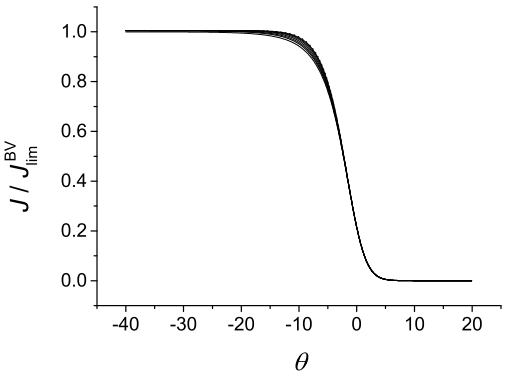
In both cases, The Alternating Direction Implicit (ADI) [39] method was employed to simulate the voltammetry, in conjunction with the Thomas Algorithm [40], as described in Chapter 2 to solve the mass transport equation and boundary conditions simultaneously in matrix form. The models were coded in C++ with multithreaded parallel programming employed to increase efficiency. Simulation running times were *c.a.* 10 mins on a 2.26 GHz Intel(R) Xenon(R) CPU with 2.25 GB of RAM.

9.3 Theoretical results

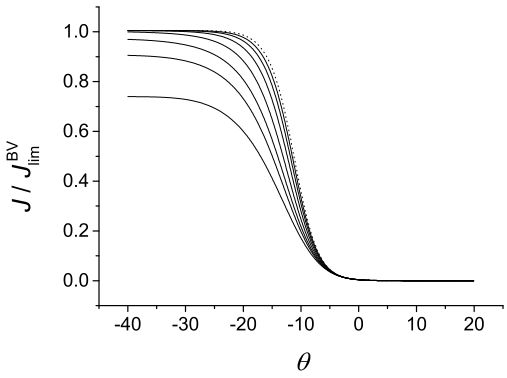
We use the models developed above to simulate steady state voltammetry at a microdisc electrode and sphere-on-a-surface electrode using symmetric Marcus-Hush theory. Kinetically limited currents at a microdisc electrode are simulated, and then compared with those at a sphere-on-a-surface electrode.

9.3.1 Kinetically limited currents at a microdisc electrode

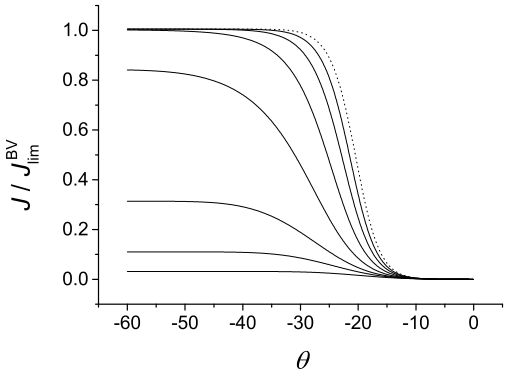
Steady state voltammetry at a microdisc electrode was simulated using the model outlined above. Various values of dimensionless reorganisation energy, Λ, and dimensionless heterogeneous rate constant, K^0, were simulated, and the results are shown in Figure 9.5. Part (a) shows results for $K^0 = 5 \times 10^{-1}$, (b) shows $K^0 = 5 \times 10^{-3}$ and (c) shows $K^0 = 5 \times 10^{-5}$. Also shown in each case is the steady state voltammetry simulated using Butler-Volmer kinetics with the same values of K^0, and $\alpha = 0.5$, and Marcus-Hush results are shown relative to this Butler-Volmer result. For all three values of K^0, it is seen



(a) $K^0 = 10^{-1}$



(b) $K^0 = 10^{-3}$



(c) $K^0 = 10^{-5}$

Figure 9.5: Simulated steady state voltammetry microdisc electrode at various Λ values and K^0. (a) $K^0 = 5 \times 10^{-1}$ (b) $K^0 = 5 \times 10^{-3}$ and (c) $K^0 = 5 \times 10^{-5}$. In each case the dotted line represents the Butler-Volmer result ($\alpha = 0.5$). Λ values are 20 (furthest from Butler-Volmer result), 25, 30, 40, 60, 100 and 200 (closest to Butler-Volmer result).

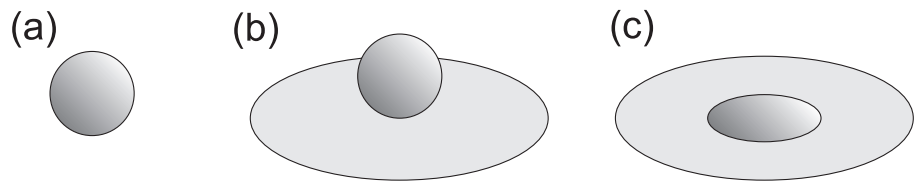


Figure 9.6: Schematic diagram of three electrode geometries which produce steady state voltammetry described by Equation 9.30. (a) Isolated spherical electrode, (b) spherical electrode resting on a conductive, inert surface and (c) a microdisc electrode.

that large Λ values produce the same limiting current as the Butler-Volmer model. As Λ becomes smaller, the limiting current becomes less than predicted by the Butler-Volmer model as kinetic control takes over. This effect is more extreme for the smallest values of K^0, where even a Λ value of 200 has not reached the Butler-Volmer limit at all points on the wave. For $K^0 = 5 \times 10^{-1}$, unfeasibly small Λ values would be required to show significant deviation from the Butler-Volmer result. This is in qualitative agreement with the previous studies of this nature [35, 36].

From the definition of K^0 given above, it is noted that lowering K^0 will mean that either k^0 or r_e is lowered, or D_A is raised. Lowering k^0 trivially means the electrochemical kinetics become more likely to be the limiting factor in the steady state current as opposed to diffusion. Either lowering r_e or increasing D_A also both lower K^0 and lead to a more kinetically limited current. This is due to the fact that either of these changes will increase mass transport efficiency to the electrode surface, thus making electrochemical kinetics the more limiting factor. Therefore, in order to see a kinetically limited current, it is desirable to have a small k^0, a small r_e and a large D_A.

9.3.2 Comparison of Marcus-Hush theory at microdisc and impacting nanoparticles

Recent work by Molina *et. al.* [38] shows that steady state voltammetry at an isolated spherical electrode alone in solution, a spherical electrode supported on a conductive but inert surface and a microdisc electrode (all shown schematically in Figure 9.6) may all be approximately described (under the Butler-Volmer formalism) by a single equation:

$$\frac{I}{I_{\text{lim}}} = \frac{\overline{K^0}\exp\left(-\alpha\theta\right)}{1+\overline{K^0}\exp\left(-\alpha\theta\right)\left[1+\exp\left(\theta\right)\right]} \tag{9.30}$$

where $\overline{K^0}$ is a dimensionless heterogeneous rate constant scaled by a geometry dependent mass transport factor. These parameters are defined for isolated spheres (is) spheres supported on surfaces (sos) and microdiscs (md) as:

$$\overline{K^0_{\text{is}}} = \frac{k^0 r_{\text{e}}}{D_{\text{A}}} = K^0_{\text{is}} \tag{9.31}$$

$$\overline{K^0_{\text{sos}}} = \frac{k^0 r_{\text{e}}}{D_{\text{A}}}\frac{1}{\ln 2} = \frac{K^0_{\text{sos}}}{\ln 2} \tag{9.32}$$

$$\overline{K^0_{\text{md}}} = \frac{k^0 r_{\text{e}}}{D_{\text{A}}}\frac{\pi}{4} = \frac{K^0_{\text{md}}\pi}{4} \tag{9.33}$$

Therefore, steady state voltammetry at a microdisc of electrochemical rate constant K^0_{md} produces approximately the same result as steady state voltammetry at a sphere-on-a-surface of heterogeneous rate constant $K^0_{\text{sos}} = \pi\ln\left(2\right)K^0_{\text{md}}/4$, as was shown.

We now investigate if this relation holds under the Marcus Hush formalism over a wide range of K^0 and Λ values. To do so, steady state voltammetry was simulated using the Marcus-Hush model described above for both a microdisc and a sphere-on-a-surface. For each microdisc heterogeneous rate constant (K^0_{md}) that was used, a corresponding sphere-

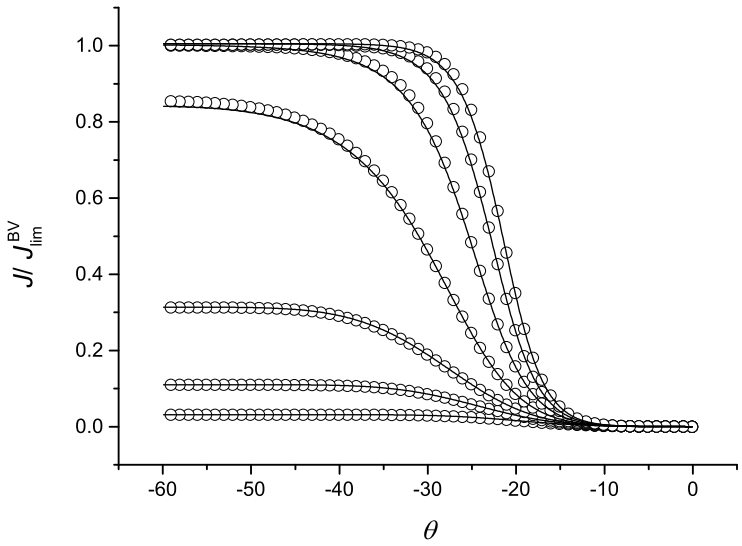
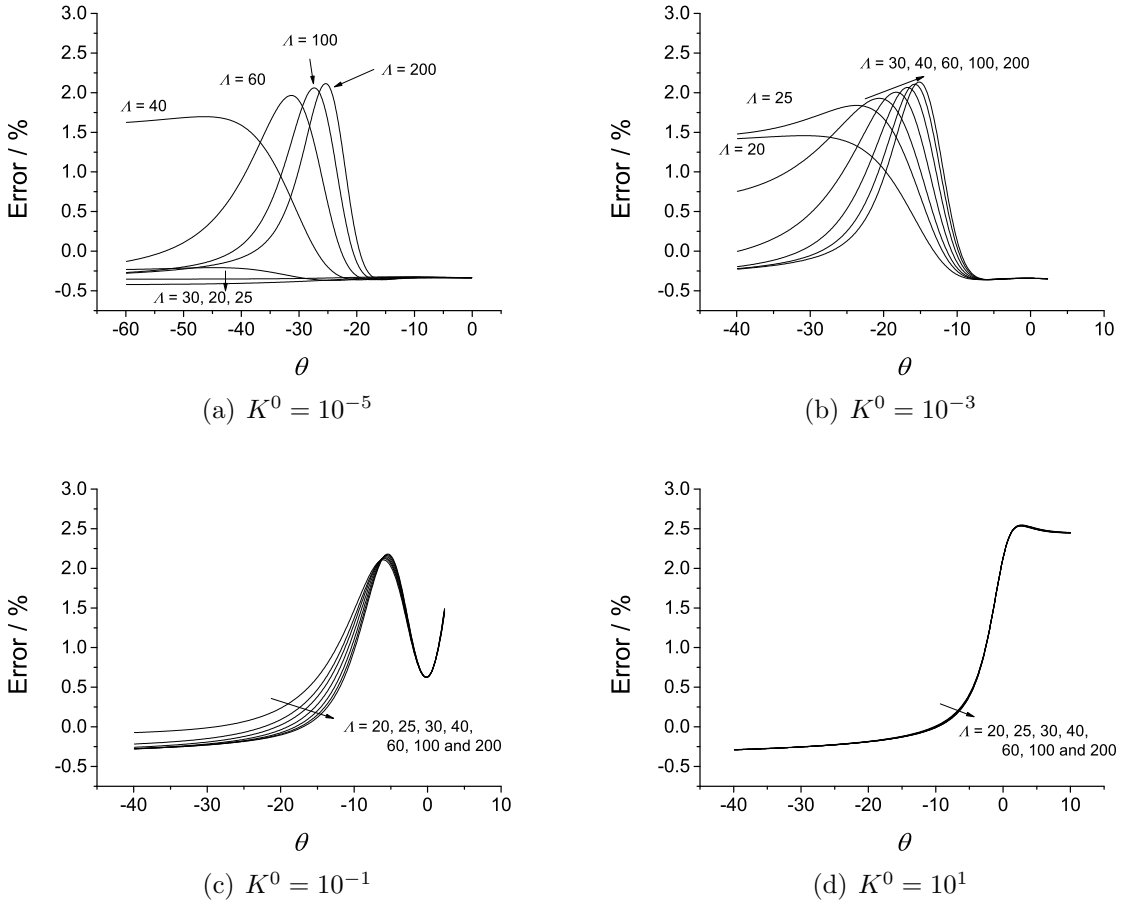


Figure 9.7: Comparison of steady state voltammetry at a microdisc electrode (solid lines) and a sphere-on-a-surface electrode (circles) using Marcus-Hush kinetics at various values of Λ. For the microdisc electrode, $K^0 = 5 \times 10^{-5}$, and for the sphere $K^0 = \frac{\pi \ln 2}{4}\,(5 \times 10^{-5})$. Λ is equal to 20 (bottom result), 25, 30, 40, 60, 100 and 200

o-a-surface simulation was run with $K^0_{\rm sos} = \pi \ln(2)\, K^0_{\rm md}/4$, with Λ the same in each case. Figure 9.7 shows simulated steady state voltammograms at a microdisc electrode (solid line) and a sphere-on-a-surface electrode (circles) at varying values of Λ (20, 24, 30, 40, 60, 100 and 200). K^0 is equal to 5×10^{-5} for the microdisc and $\frac{\pi \ln 2}{4}\,(5 \times 10^{-5})$ for the sphere. Qualitatively, the best agreement between the two geometries is seen at the smallest values of Λ where an almost exact fit is observed. Less good fits are seen at intermediate values of Λ.

Figure 9.8 (a) shows the percentage error between the fits in Figure 9.7, as well as for three other values of $K^0_{\rm md}$: 5×10^{-3} (b), 5×10^{-1} (c), and 5×10^{1} (d). To obtain the corresponding values of $K^0_{\rm sos}$, $K^0_{\rm md}$ is multiplied by $\frac{\pi \ln 2}{4}$. The percentage error is defined as:

$$\text{Error} = \frac{J_{\rm sos} - J_{\rm md}}{J_{\rm md}} \times 100\% \tag{9.34}$$



(a) $K^0 = 10^{-5}$ (b) $K^0 = 10^{-3}$

(c) $K^0 = 10^{-1}$ (d) $K^0 = 10^{1}$

Figure 9.8: Percentage error in the correspondence between steady state voltammetry at a microdisc and a sphere-on-a-surface for various values of K^0 and λ. (a) $K^0_{\mathrm{md}} = 5 \times 10^{-5}$, (b) $K^0_{\mathrm{md}} = 5 \times 10^{-3}$, (c) $K^0_{\mathrm{md}} = 5 \times 10^{-1}$, (d) $K^0_{\mathrm{md}} = 5 \times 10^{1}$. Corresponding K^0_{sos} values are obtained by multiplying K^0_{md} by $\frac{\pi \ln 2}{4}$. Λ values are indicated on the graphs.

It is seen that as K^0 increases, the error becomes less and less dependent on the values of Λ. This is because at high K^0 the Marcus-Hush model of electron transfer approaches the Butler-Volmer limit, and becomes independent of Λ. Over the whole range of K^0 and Λ values here studied, the error in the equivalence between a microdisc and a sphere-on-a-surface never exceeds 2.55% in regions of appreciable current. It is thus reasonable to say that the correspondence between the two geometries holds within the Marcus-Hush model of electron transfer, as well as within the Butler-Volmer model.

Knowing that this equivalence between microdisc electrodes and sphere-on-a-surface

electrodes holds under the Marcus-Hush formalism, we can establish which geometry is desirable for observing kinetically limited currents, for given values of k^0, r_e and D_A. The geometry with the smallest value of $\overline{K^0}$, the mass transport corrected electrochemical rate constant, is a microdisc:

$$\overline{K^0_{sos}} = \frac{k^0 r_e}{D_A}\frac{1}{\ln 2} = \frac{K^0_{sos}}{\ln 2} \approx 1.4427 K^0_{sos} \tag{9.35}$$

$$\overline{K^0_{md}} = \frac{k^0 r_e}{D_A}\frac{\pi}{4} = \frac{K^0_{md}\pi}{4} \approx 0.7854 K^0_{md} \tag{9.36}$$

This is confirmed in Figure 9.7, which established that for a sphere-on-a-surface, a smaller value of K^0 is required to achieve the same kinetically limited current as at a microdisc (or indeed nanodisc). Nanodisc electrodes of radii under 10 nm have been fabricated and characterised [41–43].

9.4 Conclusions

Models were developed to simulate cyclic voltammetry at a microdisc electrode and a sphere-on-a-surface electrode using both Butler-Volmer and symmetric Marcus-Hush kinetics. The microdisc model was used to investigate the possibility of kinetically limited steady state currents at a microdisc electrode, and it was found that for a given electrode radius, a kinetically limited will be more likely to be observed at a disc shaped electrode. It was also found that the steady state equivalence (subject to a mass transport correction) between microdisc electrodes and spherical electrodes resting on a surface also hold when Marcus-Hush kinetics are employed.

References

[1] Tanner, E. E. L.; Xiong, L.; Barnes, E. O.; Compton, R. G. *J. Electroanal. Chem.* **2014**, *727*, 59 – 68.

[2] Butler, J. A. V. *Trans. Faraday Soc.* **1924**, *19*, 729 – 733.

[3] Erdey-Grúz, T.; Volmer, M. *Z. Physik. Chem.* **1930**, *150*, 203–213.

[4] Marcus, R. A. *J. Chem. Phys.* **1956**, *24*, 966–978.

[5] Marcus, R. A. *J. Chem. Phys.* **1956**, *24*, 979 – 989.

[6] Marcus, R. A. *J. Chem. Phys.* **1957**, *26*, 867 – 871.

[7] Marcus, R. A. *J. Chem. Phys.* **1957**, *26*, 872 – 877.

[8] Hush, N. S. *J. Chem. Phys.* **1958**, *28*, 962 – 972.

[9] Chidsey, C. E. D. *Science* **1991**, *251*, 919 – 922.

[10] Finklea, H. O.; Hanshew, D. D. *J. Am. Chem. Soc.* **1992**, *114*, 3173 – 3181.

[11] Forster, R. J.; Faulkner, L. R. *J. Am. Chem. Soc.* **1994**, *116*, 5444 – 5452.

[12] Richardson, J. N.; Rowe, G. K.; Carter, M. T.; Tender, L. M.; Curtin, L. S.; Peck, S. R.; Murray, R. W. *Electrochim. Acta* **1995**, *40*, 1331 – 1338.

[13] Richardson, J. N.; Peck, S. R.; Curtin, L. S.; Tender, L. M.; Terrill, R. H.; Carter, M. T.; Murray, R. W.; Rowe, G. K.; Creager, S. E. *J. Phys. Chem.* **1995**, *99*, 766–772.

[14] Hirst, J.; Armstrong, F. *Anal. Chem.* **1998**, *70*, 5062 – 5071.

[15] Finklea, H. O.; Yoon, K.; Chamberlain, E.; Allen, J.; Haddox, R. *J. Phys. Chem. B* **2001**, *105*, 3088 – 3092.

[16] Ravenscroft, M. S.; Finklea, H. O. *J. Phys. Chem.* **1994**, *98*, 3843–3850.

[17] Finklea, H. O.; Liu, L.; Ravenscroft, M. S.; Punturi, S. *J. Phys. Chem.* **1996**, *100*, 18852 – 18858.

[18] Yan, J.; Dong, S.; Li, J.; Chen, W. *J. Electrochem. Soc.* **1997**, *144*, 3858 – 3865.

[19] Chi, Q.; Zhang, J.; Andersen, J. E. T.; Ulstrup, J. *J. Phys. Chem. B* **2001**, *105*, 4669 – 4679.

[20] Fristrup, P.; Grubb, M.; Zhang, J.; Christensen, H.; Hansen, A.; Ulstrup, J. *J. Electroanal. Chem.* **2001**, *511*, 128 – 133.

[21] Smalley, J. F.; Newton, M. D.; Feldberg, S. W. *J. Electroanal. Chem.* **2006**, *598*, 1 – 6.

[22] Henstridge, M. C.; Batchelor-McAuley, C.; Gusmo, R.; Compton, R. G. *Chemical Physics Letters* **2011**, *517*, 108 – 112.

[23] Henstridge, M. C.; Laborda, E.; Compton, R. G. *J. Electroanal. Chem.* **2012**, *674*, 90 – 96.

[24] Henstridge., M. C.; Wang, Y.; Limon-Petersen, J. G.; Laborda, E.; Compton, R. G. *Chem. Phys. Let.* **2011**, *517*, 29 – 35.

[25] Laborda, E.; Wang, Y.; Henstridge, M. C.; Martínez-Ortiz, F.; Molina, A.; Compton, R. G. *Chem. Phys. Let.* **2011**, *512*, 133 – 157.

[26] Suwatchara, D.; Henstridge, M. C.; Rees, N. V.; Compton, R. G. *J. Phys. Chem. C* **2011**, *115*, 14876 – 14882.

[27] Suwatchara, D.; Rees, N. V.; Henstridge, M. C.; Laborda, E.; Compton, R. G. *J. Electroanal. Chem.* **2012**, *665*, 38 – 44.

[28] Wang, Y.; Laborda, E.; Henstridge, M. C.; Martinez-Ortiz, F.; Molina, A.; Compton, R. G. *J. Electroanal. Chem.* **2012**, *668*, 7 – 12.

[29] Henstridge, M. C.; Laborda, E.; Y., W.; Suwatchara, D.; Rees, N. V.; Molina, A.; Martínez-Ortiz, F.; Compton, R. G. *J. Electroanal. Chem.* **2012**, *672*, 45 – 52.

[30] Laborda, E.; Henstridge, M. C.; Compton, R. G. *J. Electroanal. Chem.* **2012**, *667*, 48 – 53.

[31] Suwatchara, D.; Henstridge, M. C.; Rees, N. V.; Laborda, E.; Compton, R. G. *J. Electroanal. Chem.* **2012**, *677*, 120 – 126.

[32] Suwatchara, D.; Rees, N. V.; Henstridge, M. C.; Laborda, E.; Compton, R. G. *J. Electroanal. Chem.* **2012**, *685*, 53 – 62.

[33] Laborda, E.; Suwatchara, D.; Rees, N. V.; Henstridge, M. C.; Molina, A.; Compton, R. G. *Electrochim. Acta.* **2013**, *110*, 772 – 779.

[34] Henstridge, M. C.; Laborda, E.; Rees, N. V.; Compton, R. G. *Electrochim. Acta* **2012**, *84*, 12 – 20.

[35] Feldberg, S. W. *Anal. Chem.* **2010**, *82*, 5176 – 5183.

[36] Henstridge, M. C.; Ward, K. R.; Compton, R. G. *J. Electroanal. Chem.* **2014**, *712*, 14 – 18.

[37] Oldham, K. B.; Zoski, G. *J. Electroanal. Chem.* **1988**, *256*, 11 – 19.

[38] Molina, A.; Gonzalez, J.; Barnes, E. O.; Compton, R. G. *J. Phys. Chem. C.* **2014**, *118*, 346 – 356.

[39] Britz, D. *Digital Simulation in Electrochemistry*; Springer-Verlag: Heidelberg, 2005.

[40] Press, W. H., Teukolsky, S. A., Vetterling, W. T., Flannery, B. P., Eds. *Numerical Recipes: The Art of Scientific Computing*; Cambridge University Press, 2007.

[41] Shao, Y.; Mirkin, M. V.; Fish, G.; Kokotov, S.; Palanker, D.; Lewis, A. *Anal. Chem.* **1997**, *69*, 1627–1634.

[42] Ballesteros, B.; Schuhmann, W. *Electroanalysis* **2002**, *14*, 22 – 28.

[43] Danis, L.; Snowden, M. E.; Tefashe, U. M.; Heinemann, C. N.; Mauzeroll, J. *Electrochim. Acta* **2014**, *136*, 121 – 129.

Chapter 10

Conclusions

This thesis set out to develop models to simulate electrochemical experiments, and apply these models to extend and refine electroanalytical techniques, reaching the following conclusions.

The first area explored was the effect of hindered diffusion on the electorchemistry of nanoparticles. The results of anodic particle coulometry experiments were found to be highly sensitive to the size of the nanoparticles, with larger nanoparticles giving less frequent impacts than expected using a constant diffusion coefficient model. This has clear implications in anodic particle coulometry experiments, were impact frequencies are used to calculate nanoparticle concentration. The validity of the model was shown by the successful simulation of the anodic particle coulometry of nickel nanoparticles.

Hindered diffusion was also found to affect the adsorption properties of nanoparticles, with larger nanoparticles adsorbing more slowly onto an electrode surface due to the slower mass transport. If adsorption occurs, it was found to cause significant depletion of nanoparticles around the electrode surface, which may take hours to dissipate and will have consequences for the results of anodic particle coulometry experiments. A possible

solution to this is to mechanically stir the solution to speed up the formation of a full monolayer and quickly re-establish a uniform concentration profile.

Microband electrodes were found to be useful tools for the determination of the concentration of an electroactive species, and the diffusion coefficient of both pairs in the redox couple *via* double potential step chronoamperometry. The diffusion coefficients of decamethylferrocene and its cation were determined *via* the fitting of experimental data, and found to be in excellent agreement with values determined using a microdisc electrode.

Having successfully constructed a model for chronoamperometry at a single band electrode, a model to simulate generator-collector experiments at dual band electrodes was developed. It was found that if two species are present in solution with sufficiently different diffusion coefficients, then simultaneous measurement of two species over a wide range of mole fractions was possible. Using a theoretical case of ascorbic acid and dopamine in water, the range of detectable mole fractions of ascrobic acid was predicted to be between 0.055 and 0.96.

The dual band generator-collector model was then extended to simulate chronoamperometry and interdigitated arrays of bands and rings. It was found that if the peripheral electrodes in an interdigitated ring array had a large enough radius, the may be approximated as bands, allowing a simpler model to be used to simulate cyclic voltammetry at an interdigitated ring array. Experimental cyclic voltammetry of $Fe(CN)_6^{4-}$ at both interdigitated bands and rings was successfully simulated.

Electrochemistry using porous working electrodes was then investigated, using a model which decouples diffusion inside spherical voids in an electrode from the linear diffusion to the electrode surface from bulk solution. It was found that if chronoamperometry is

performed on electrodes of this type, then the contribution from inside the pores is lost over very short timescales and will likely be unobservable. In cyclic voltammetry however, contributions to the current from both inside the pores and to the electrode surface were found to be observable. The different modes of diffusion also result in the splitting of the voltammetric peak in cases of slow electrode kinetics, allowing for the possible direct measurement of electrochemical rate constants.

Finally, symmetric Marcus-Hush theory was used to simulate steady state voltammetry at microdisc electrodes and sphere-on-a-surface electrodes. It was found that the equivalence between these two geometries previously reported under Butler-Volmer kinetics continues to hold under Marcus-Hush kinetics. This equivalence was used to show that for a given electrode radius, a kinetically limited current is most likely to be observed at a micro- (or nano-) disc electrode.

Overall, this thesis has demonstrated the power and importance of simulation in electrochemistry not only as a tool to extract important physical parameters, but also to help develop and refine electroanalytical techniques to unlock their full potential.